

Optimal Design of Focusing Nanoantennas for Light

Novel Approaches: From Evolution to Mode-Matching

DISSERTATION

zur Erlangung des
naturwissenschaftlichen Doktorgrades
der Julius-Maximilians-Universität Würzburg

vorgelegt von
Thorsten Feichtner
aus
Bad Kötzing

Würzburg 2016



Eingereicht am: 02. Mai 2016
bei der Fakultät für Physik und Astronomie

1. Gutachter: Prof. Dr. Bert Hecht
2. Gutachter: Prof. Dr. Tobias Brixner
3. Gutachter: _____
der Dissertation

Vorsitzende(r): Prof. Dr. Peter Jakob

1. Prüfer: Prof. Dr. Bert Hecht
2. Prüfer: Prof. Dr. Tobias Brixner
3. Prüfer: Prof. Dr. Haye Hinrichsen
im Promotionkolloquiums

Tag des Promotionskolloquiums: 23. November 2016

Doktorurkunde ausgehändigt am: _____

Der Fee an meiner Seite.

Abstract

Optical antennas work similar to antennas for the radio-frequency regime and convert electromagnetic radiation into oscillating electrical currents. Charge density accumulations form at the antenna surface leading to strong and localized near-fields. Since most optical antennas have dimensions of a few hundred nanometers, their near-fields allow the focusing of electromagnetic fields to volumes much smaller than the diffraction limit, with intensities several orders of magnitude larger than achievable with classical diffractive and refractive optical elements. The task to maximize the emission of a quantum emitter, a point-like entity capable of reception and emission of single photons, is identical to the task to maximize the field intensity at the position of the quantum emitter. Therefore it is desirable to optimize the capabilities of focusing optical antennas.

Radio-frequency-antenna designs scaled to optical dimensions of several hundred nanometers show already a decent performance. However, optical frequencies lie near the plasma frequency of the metals used for optical antennas and the mass of electrons cannot be neglected anymore. This leads to new physical phenomena. Light can couple to charge density oscillations, yielding a so-called Plasmon. Effects emerge which have no equivalent in the very advanced field of radio-frequency-technology, e.g. volume currents and shortened effective wavelengths. Additionally the conductivity is not infinite anymore, leading to thermal losses. Therefore, the question for the optimal geometry of a focusing optical antenna is not easy to answer. However, up to now there was no evidence that there exist better alternatives for optical antennas than down-scaled radio-frequency designs.

In this work the optimization of focusing optical antennas is based on an approach, which often proved successful for radio-frequency-antennas in complex applications (e.g. broadband and isotropic reception): evolutionary algorithms. The first implementation introduced here allows a large freedom regarding particle shape and count, as it arranges cubic voxels on a planar, square grid. The geometries are encoded in a binary matrix, which works as a genome and enables the methods of mutation and crossing as mechanism of improvement. Antenna geometries optimized in this way surpass a comparable dipolar geometry by a factor of 2. Moreover, a new working principle can

be deduced from the optimized antennas: a magnetic split-ring resonance can be coupled conductively to dipolar antennas, to form novel and more effective split-ring-antennas, as their currents add up constructively near the focal point.

In a next step, the evolutionary algorithm is adapted so that the binary matrices describe geometries with realistic fabrication constraints. In addition a 'printer driver' is developed which converts the binary matrices into commands for focused ion-beam milling in mono-crystalline gold flakes. It is shown by means of confocal two-photon photo-luminescence microscopy that antennas with differing efficiency can be fabricated reliably directly from the evolutionary algorithm. Besides, the concept of the split-ring antenna is further improved by adding this time two split-rings to the dipole-like resonance.

The best geometry from the second evolutionary algorithm inspires a fundamentally new formalism to determine the power transfer between an antenna and a point dipole, best termed 'three-dimensional mode-matching'. Therewith, for the first time intuitive design rules for the geometry of an focusing optical antenna can be deduced. The validity of the theory is proven analytically at the case of a point dipole in front of a metallic nano sphere.

The full problem of focusing light by means of an optical antenna can, thus, be reduced to two simultaneous mode-matching conditions – on the one hand with the fields of a point dipole, on the other hand with a plane wave. Therefore, two types of ideal focusing optical antenna mode patterns are identified, being fundamentally different from the established dipolar antenna mode. This allows not only to explain the functionality of the evolutionary antennas and the split-ring antenna, but also helps to design novel plasmonic cavity antennas, which lead to an enhanced focusing of light. This is proven numerically in direct comparison to a classical dipole antenna design.

optical antennas, plasmonics, nano optics, LDOS, evolutionary optimization, mode matching

Zusammenfassung

Optische Antennen arbeiten ähnlich wie Antennen für Radiowellen und wandeln elektromagnetische Strahlung in elektrische Wechselströme um. Ladungsdichteansammlungen an der Antennen-Oberfläche führen zu starken und lokalisierten Nahfeldern. Da die meisten optischen Antennen eine Ausdehnung von wenigen hundert Nanometern besitzen, ermöglichen es ihre Nahfelder, Licht auf ein Volumen weit unterhalb des Beugungslimits zu fokussieren, mit Intensitäten, die mehrere Größenordnungen über dem liegen, was man mit klassischer beugender und reflektierender Optik erreichen kann. Die Aufgabe, die Abstrahlung eines Quantenemitters zu maximieren, eines punktförmigen Objektes, welches einzelne Photonen absorbieren und emittieren kann, ist identisch mit der Aufgabe, die Feldintensität am Ort des Quantenemitters zu maximieren. Darum ist es erstrebenswert, den Fokus optischer Antennen zu optimieren

Optimierte Radiofrequenz-Antennen, welche auf Größenordnungen von wenigen 100 Nanometern herunterskaliert werden, zeigen bereits eine gute Funktionalität. Jedoch liegen optische Frequenzen in der Nähe der Plasmafrequenz von den Metallen, die für optische Antennen genutzt werden und die Masse der Elektronen kann nicht mehr vernachlässigt werden. Dadurch treten neue physikalische Phänomene auf. Es entstehen gekoppelte Zustände aus Licht und Ladungsdichte-Schwingungen, die sogenannten Plasmonen. Daraus folgen Effekte wie Volumenströme und kürzere effektive Wellenlängen. Zusätzlich führt die endliche Leitfähigkeit zu thermischen Verluste. Das macht eine Antwort auf die Frage nach der optimalen Geometrie für fokussierende optische Antennen schwer. Jedoch stand vor dieser Arbeit der Beweis noch aus, dass es für optische Antennen bessere Alternativen gibt als herunterskalierte Radiofrequenz-Konzepte.

In dieser Arbeit werden optische Antennen auf eine bestmögliche Fokussierung optimiert. Dafür wird ein Ansatz gewählt, welcher bei Radiofrequenz-Antennen für komplexe Anwendungsfelder (z.B. isotroper Breitbandempfang) schon oft Erfolg hatte: evolutionäre Algorithmen. Die hier eingeführte erste Implementierung erlaubt eine große Freiheit in Bezug auf Partikelform und Anzahl, da sie quadratische Voxel auf einem planaren, quadratischen Gitter beliebig anordnet. Die Geometrien werden in einer binären Matrix codiert, welche

als Genom dient und somit Methoden wie Mutation und Paarung als Verbesserungsmechanismus erlaubt. So optimierte Antennen-Geometrien übertreffen vergleichbare klassische Dipol-Geometrien um einen Faktor von Zwei. Darüber hinaus lässt sich aus den optimierten Antennen ein neues Funktionsprinzip ableiten: ein magnetische Split-Ring-Resonanz kann mit Dipol-Antennen leitend zu neuartigen und effektiveren Split-Ring-Antennen verbunden werden, da sich ihre Ströme nahe des Fokus konstruktiv überlagern.

Im nächsten Schritt wird der evolutionäre Algorithmus so angepasst, so die Genome real herstellbare Geometrien beschreiben. Zusätzlich wird er um eine Art "Druckertreiber" erweitert, welcher aus den Genomen direkt Anweisungen zur fokussierten Ionenstrahl-Bearbeitung von einkristallinen Goldflocken erstellt. Mit Hilfe von konfokaler Mikroskopie der Zwei-Photonen-Photolumineszenz wird gezeigt, dass Antennen unterschiedlicher Effizienz reproduzierbar aus dem evolutionären Algorithmus heraus hergestellt werden können. Außerdem wird das Prinzip der Split-Ring-Antenne verbessert, indem zwei Ring-Resonanzen zu einer Dipol-Resonanz hinzugefügt werden.

Zu guter Letzt dient die beste Antenne des zweiten evolutionäre Algorithmus als Inspiration für einen neuen Formalismus zur Beschreibung des Leistungsübertrages zwischen einer optischen Antenne und einem Punkt-Dipol, welcher sich als „dreidimensionaler Modenüberlapp“ beschreiben lässt. Damit können erstmals intuitive Regeln für die Form einer optischen Antenne aufgestellt werden. Die Gültigkeit der Theorie wird analytisch für den Fall eines Dipols nahe einer metallischen Nano-Kugel gezeigt.

Das vollständige Problem, Licht mittels einer optischen Antenne zu fokussieren, lässt sich so auf die Erfüllung zweier Modenüberlapp-Bedingungen reduzieren – mit dem Feld eines Punktdipols, sowie mit einer ebenen Welle. Damit lassen sich zwei Arten idealer Antennenmoden identifizieren, welche sich von der bekannten Dipol-Antennen-Mode grundlegend unterscheiden. Zum einen lässt sich dadurch die Funktionalität der evolutionären und Split-Ring-Antennen erklären, zum lassen sich neuartige plasmonische Hohlraum-Antennen entwerfen, welche zu besserer Fokussierung von Licht führen. Dies wird numerisch im direkten Vergleich mit einer klassischen Dipolantennen-Geometrie gezeigt.

Optische Antennen, Plasmonik, Nano-Optik, LDOS, Evolutionäre Optimierung, Moden-Überlapp

Contents

1	Introduction and overview	v
I	Theoretical foundations	1
2	Classical electrodynamics	3
2.1	Maxwell's equations	3
2.2	Waves and the diffraction limit	5
2.3	Quantum emitters as classical dipoles	9
2.3.1	Point dipole in free space	9
2.3.2	Point dipole in arbitrary environments	13
2.4	Radiofrequency antennas	15
2.4.1	General properties	16
2.4.2	Characteristics of 1D antennas	18
2.4.3	Reciprocity theorem	21
3	Focusing antennas for visible light	25
3.1	The dielectric function of gold	26
3.2	Plasmons	30
3.2.1	Particle plasmons	32
3.2.2	Quasistatic approximation	35
3.2.3	Far-field radiation patterns	36
3.2.4	Mie scattering	38
3.2.5	Split-ring resonators and kinetic inductance	41
3.3	Optical antennas	43
3.3.1	Definition and application	43
3.3.2	The dipolar two-wire antenna	44

3.3.3	Quantum emitter emission enhancement	49
II	Methods	57
4	Numerics	59
4.1	The finite-difference time-domain algorithm	60
4.1.1	Meshing of cubes touching at edges	62
4.1.2	Materials for FDTD-simulations	64
4.1.3	Comparison to analytical solution	65
4.2	The finite element method	66
4.3	Evolutionary optimization	68
4.3.1	Definitions and working principle	68
4.3.2	Evolution for plasmonics - previous work	69
5	Fabrication	73
5.1	State of the art	73
5.2	Focused ion-beam milling with Ga	76
5.3	Monocrystalline gold flakes	77
5.4	Sample preparation	80
6	Characterization	83
6.1	Two-photon photo-luminescence	83
6.2	Scanning confocal microscopy	85
III	Results	89
7	Evolutionary optimization of 2D focusing optical antennas	91
7.1	Algorithm	91
7.2	Results	95
7.3	The split-ring antenna	102
8	Evolutionary optimization of realistic optical antennas	107
8.1	Algorithm adaption	108
8.2	Result of evolution	110
8.3	Experiment	113

9	Modematching for optical antennas	119
9.1	Theory	119
9.2	Dipole in front of sphere	121
9.3	Revisiting the split-ring-antenna	123
9.4	Intelligent design of nanoantennas	125
9.5	p-type mode PCA	129
9.6	Discussion and Conclusion	129
10	Summary & Outlook	133
IV	Appendix	139
A	Number of non redundant binary odd-sized square matrices with one symmetric and one antisymmetric axis	141
B	Local configuration space maxima in experimental EA	145
C	Fitness changes in realistic evolutionary antennas due to fab- rication inaccuracies.	147
D	List of publications	149
E	Acknowledgements	171

Chapter 1

Introduction and overview

An optical antenna is a device to convert far-field radiation into electrical energy (=currents) at frequencies in the order of 10^{14} Hz. This is comparable to the widely established radio-frequency (rf) antennas. However, optical antennas are often realized from noble metals and show for visible light a phenomenon unknown in rf-technology: particle plasmons polaritons (PPPs) or short plasmons.

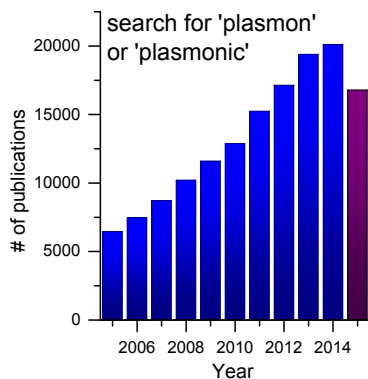


Figure 1.1: Publications per year in the Web of Knowledge for 'plasmon' OR 'plasmonic'. The 2015 value has been retrieved at Nov. 24th 2015.

experiments can be performed at ambient conditions. (ii) Nanofabrication tools have developed to commercially available products allowing a decent control of structuring materials down to feature dimensions of < 10 nm. (iii) Many

Plasmonics is the science of surface or particle charge density oscillations coupled to light, of photons and polaritons interacting at a surface at frequencies close to the materials plasma frequency ν_p . In this frequency regime the inertia of the metal electrons driven by the impinging light fields is not negligible any more [1]. Plasmons and the resultant effects are a research field constantly growing over the last few years (see Fig. 1.1) which has several reasons: (i) Optical antennas are often made from noble metals, an easy to handle material – especially gold that degrades only very slowly in air. Therefore, most ex-

findings and applications of classical optics and rf-antennas also work with plasmonic structures, e.g. magneto-optical effects [2], often even with benefits. (iv) Noble metals show strong plasmon resonances in the optical regime. Visible light based technologies in general have a large impact in sensing [3] and a promising future in information technology [4]. (v) Plasmonic resonators are often much smaller than the free space wavelength at the same frequency, making them ideal building blocks for tailoring the optical response of novel materials, opening e.g. the research field of optical meta materials [5] and meta surfaces [6].

Optical antennas are plasmonic resonators which can be used to scatter light efficiently [3, 7] or to convert light into heat [8–10]. Yet, the plasmon property applied most often is their capability to concentrate far-field electromagnetic radiation into highly localized near-field hot spots [11]. By so-called focusing optical antennas the diffraction limit of wave optics [12] can be beaten, which usually poses a strict barrier for the resolution of optical microscopes working with reflecting and refracting elements only. The small focal volume can be used to enhance imaging resolution which is used for scanning near-field optical microscopy [13]¹. In addition, the field strength can be enhanced, which connects directly to the local density of states (LDOS) [15] and, therefore, determines the lifetime of excited quantum emitters (QE) [16], point like entities with electronic energy levels absorbing and emitting single photons. It has been shown that optical antennas can be used to enhance the spontaneous emission rate of a dye by a factor of more than 1000 [17]. There are already a lot of applications realized using focusing optical antennas like single molecule mapping and spectroscopy [18], optical tweezers [19] or efficient single photon sources [20].

This work tries to find an answer to the question: What is the optimal focusing optical antenna?

Figure 1.2 shows the processes involved, when a quantum emitter is coupled to the far-field radiation continuum by means of an optical antenna. It is a two-step process (compare to a similar description in [21]): Far-field radiation is collected by the antenna, transformed into currents and, therefore, into near-fields at the antenna boundary. These near-fields then transport energy to the

¹A history of near-field microscopy technologies can be found here [14].

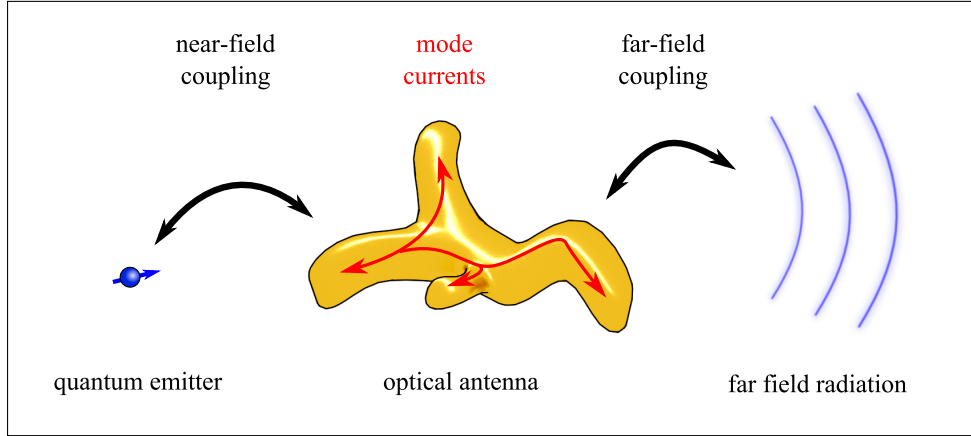


Figure 1.2: Entities and steps involved in the process of excitation/emission enhancement of a quantum emitter by means of an focusing optical antenna.

quantum emitter, if it is located in the direct vicinity of the optical antenna.

That is why everything depends on the antenna mode, the current pattern performing both tasks, the near-field and the far-field coupling. As inspiration for an optimal focusing optical antenna, designs from rf-antenna technology seem to be a good source. However, rf-antennas are usually made from thin, perfectly conducting wires that only support surface currents and are typically fed by transmission lines connected at infinitely narrow gaps [22]. For optical antennas at frequencies near the materials plasma frequency the general operation conditions deviate substantially: (i) Antenna wire diameters are comparable to the electromagnetic penetration depth into the wire material leading to volume currents [23] and therefore to a reduced effective wavelength of wire waves [14]. (ii) Feeding (excitation) of optical antennas is mostly realized by focused laser beams or point quantum emitters. (iii) high-frequency-related effects such as a finite conductivity (heat generation) and the 'kinetic inductance' [24] become significant. Therefore optical antenna designs inspired from the rf-regime, like dipole [25], bow tie [26,27] and Yagi-Uda antennas [28], not necessarily represent 'optimal' geometries at optical frequencies, despite providing a decent functionality.

This work makes use of evolutionary optimization with the objective of discovering novel geometries for focusing optical antennas. Their analysis should offer new insights into the physics of near field focusing. Therefore, chapter 2 introduces the basic physical concepts necessary to understand optical anten-

nas. It starts out with Maxwell's equations, as they are sufficient to describe all involved plasmonic effects. Also far field focusing as well as single emitter emission are reviewed, being sources and detectors for electromagnetic near- and far-fields. This chapter also gathers important concepts from rf-antenna theory, as they later help to understand optical antennas by comparing similarities and highlighting differences. Finally, the reciprocity theorem will be introduced, which is the basis of understanding the power transfer between multiple sources of radiation in arbitrary environments.

Optical antennas are described in detail in chapter 3. After discussing the behavior of metals at optical frequencies, the concept of the plasmon will be introduced. A generalized definition of optical antennas with emphasis on possible applications will be given before their basic properties will be walked through at the example of the dipolar two wire antenna. The current state of scientific knowledge about the coupling between optical antennas and QEs will be reviewed and the chapter will be concluded by detailing the fundamental differences between optical antennas and both the concepts used to describe radio-frequency technology and cavity physics.

The methods part explains in chapter 4 the numerical methods used for this work, the finite-difference time-domain algorithm as well as briefly the finite-element method. Also concepts and vocabulary associated to evolutionary optimization is introduced, a powerful heuristic tool to find good (but not necessarily the best) solution to complex problems. This method has been applied in a few works for plasmonic topics until now, which are reviewed. The fabrication of metal geometries with nanometer-sized features is the focus of chapter 5, with an emphasis on focused ion beam milling of monocrystalline gold flakes. Finally, the confocal microscope as means of optical antenna characterization together with the physics of two-photon-photo-luminescence is presented in chapter 6.

The results are separated into three chapters. The first, chapter 7, contains a numeric-only proof of principle for a novel kind of evolutionary optimization scheme applied to focusing optical antennas. It is a genetic algorithm working with a planar 21×21 matrix with binary entries as genome, to describe arbitrary shapes made from 10 nm cubic gold voxels. The resulting antenna geometry outperforms a dipolar reference design by a factor of two. As de-

sired, it also provides insights into its working principle, combining a dipolar with a split-ring mode, which is the fundamental magnetic resonance with ring-shaped mode currents. The novel antenna mode permits the realization of split-ring like modes in the optical regime for the first time, too, as kinetic inductance prohibits resonances below 900 nm for plain split-rings [24].

In chapter 8 the evolutionary algorithm is refined to describe realistic geometries. Furthermore, a 'printer driver' is developed, allowing the direct fabrication of a simulated structure by means of focused ion beam milling in monocrystalline gold flakes. Confocal two-photon photo-luminescence microscopy experiments prove the feasibility of fabrication and the validity of the numerical results. Additionally, the realistic antenna geometries show an extension of the split-ring antenna working principle, this time with two split-ring-like currents coupled to a dipolar antenna mode.

Finally, in chapter 9 a novel theoretical framework is developed to describe the energy transfer between an optical antenna and a QE. It is a formalism best described as 'three-dimensional mode-matching' which is derived on the basis of Poynting's theorem combined with reciprocity. After an analytical prove for a QE near a sphere model, the next step is to add a second mode-matching condition based on plane wave illumination to optimize also the far-field coupling of a focusing optical antenna (as depicted in Fig. 1.2). Two types of optimal antennas mode patterns are identified, which can be used as intuitive design guide lines for optimal focusing optical antennas. One of the novel modes allows to fully understand the evolutionary antenna geometry resulting in chapter 8, the second mode pattern is used to devise a novel plasmonic cavity antenna geometry, surrounding a QE with gold at the full solid angle of 4π and, thus, outperforming a comparable dipolar antenna design.

In the end it should be noted that in this work the term optical antenna is used to describe a distinct functionality, not a device nor a geometry. As one can use a stone as a hammer, though also as a paperweight, a metal nanosphere can be termed a 'scatterer' – deforming and redirecting far-field electromagnetic waves – or an 'optical antenna', transducing far-field radiation into electric currents leading to localized near-fields, scattered far-fields and heat. Optical antennas can be optimized to one of these three phenomena. Therefore, the main question answered in this work could also be: Which shape

constitutes a good *focusing* optical antenna? This has not yet been answered in a satisfactory way, in contrast to the case of the hammer. However, this work is a large step in the right direction.

Part I

Theoretical foundations

Chapter 2

Classical electrodynamics

This chapter starts with briefly introducing Maxwell's equations, while the subsequent sections will look at some of their implications needed to understand optical antennas: After the fields in a tightly focused beam of light are described, the physics of a point dipole in arbitrary environments is developed which is used to represent quantum emitters like e.g. dye molecules. The last part shortly reviews general radio frequency (RF) antenna theory, gives a more detailed analysis of one-dimensional RF-antennas and introduces the reciprocity theorem. For further reading about classical electrodynamics (at the nanoscale) one should rely on comprehensive standard literature, e.g. [16, 29], while rf-antenna theory is covered in [22, 30].

Recent efforts in theory and simulation [31–34] have explored the conditions for quantum effects to emerge in the field of plasmonics: particle distances shorter than 0.3 nm or particle sizes smaller than 10 nm lead to tunneling currents and non-local effects [35]. First experiments have been performed in this novel research field called *quantum plasmonics* [36–40]. However, the optical antennas presented in this work are more coarse metallic nanostructures and classical electrodynamics is sufficient to describe their plasmonic behavior.

2.1 Maxwell's equations

Since 1861 classical electromagnetism at the macroscopic scale has a closed theoretical form, describing the wealth of physical effects connected to electric and magnetic fields in nearly arbitrary materials as well as their dependency

on their sources, namely electrical charges and currents. James Clerk Maxwell gathered and completed the knowledge of his time, which today generally is written in the differential formulation of Oliver Heaviside [41]:

$$\nabla \cdot \mathbf{D}(\mathbf{r}, t) = \rho(\mathbf{r}, t) \quad (2.1a)$$

$$\nabla \cdot \mathbf{B}(\mathbf{r}, t) = 0 \quad (2.1b)$$

$$\nabla \times \mathbf{E}(\mathbf{r}, t) = -\frac{\partial \mathbf{B}(\mathbf{r}, t)}{\partial t} \quad (2.1c)$$

$$\nabla \times \mathbf{H}(\mathbf{r}, t) = \frac{\partial \mathbf{D}(\mathbf{r}, t)}{\partial t} + \mathbf{j}(\mathbf{r}, t) \quad . \quad (2.1d)$$

Here \mathbf{E} and \mathbf{H} denote the electric and magnetic field respectively, while \mathbf{D} and \mathbf{B} represent the electric displacement field and magnetic flux density. ρ and \mathbf{j} are the charge and current density, respectively, sources of electric and magnetic fields.

Electromagnetic fields and flux densities can be Fourier-transformed to an infinite series of harmonic components of angular frequency ω following e.g. the relation $\mathbf{E}(\mathbf{r}, t) = \int \mathbf{E}(\mathbf{r}, \omega) \cdot e^{-i\omega t} d\omega$. Here $\mathbf{E}(\mathbf{r}, \omega)$ is denoted as phasor. Maxwell's equations (2.1) in frequency dependent form using phasors are:

$$\nabla \cdot \mathbf{D}(\mathbf{r}, \omega) = \rho(\mathbf{r}, \omega) \quad (2.2a)$$

$$\nabla \cdot \mathbf{B}(\mathbf{r}, \omega) = 0 \quad (2.2b)$$

$$\nabla \times \mathbf{E}(\mathbf{r}, \omega) = i\omega \mathbf{B}(\mathbf{r}, \omega) \quad (2.2c)$$

$$\nabla \times \mathbf{H}(\mathbf{r}, \omega) = -i\omega \mathbf{D}(\mathbf{r}, \omega) + \mathbf{j}(\mathbf{r}, \omega) \quad . \quad (2.2d)$$

If not stated differently, in this work the phasor-formulation will be used and the abbreviation $\mathbf{E} = \mathbf{E}(\mathbf{r}, \omega)$.

Fields and flux densities are linked via the material equations:

$$\mathbf{D} = \varepsilon_0 \varepsilon_r(\mathbf{r}, \omega) \mathbf{E} \quad (2.3a)$$

$$\mathbf{B} = \mu_0 \mu_r(\mathbf{r}, \omega) \mathbf{H} \quad . \quad (2.3b)$$

The relative electrical permittivity ε_r and the relative magnetic permeability μ_r are in general material, position and field strength dependent second order tensors. In this work only homogeneous, local, isotropic and linear materials will be considered, described by a field strength independent scalar. In vacuum ε_r and μ_r equal unity and only the vacuum values $\varepsilon_0 = 8.8541... \cdot 10^{-12} \frac{\text{As}}{\text{Vm}}$ and

$\mu_0 = 4\pi \cdot 10^{-7} \text{ Hm}^{-1}$ remain. They are linked to the vacuum speed of light $c = (\varepsilon_0\mu_0)^{-1/2}$.

Energy conservation is given by Poyntings theorem, written in differential form for non-dispersive media as:

$$-\left\langle \frac{\partial W}{\partial t} \right\rangle = \frac{1}{2} \text{Re}(\mathbf{j}^* \cdot \mathbf{E}) + \nabla \text{Re}(\mathbf{S}) \quad (2.4)$$

, with $\langle \partial W / \partial t \rangle$ being the mean temporal change of energy at a given point in space and time, $\mathbf{j}^* \cdot \mathbf{E}$ the power flow density by means of electric currents and $\mathbf{S} = \frac{1}{2}(\mathbf{E} \times \mathbf{H}^*)$ the Poynting vector, describing the energy transport via radiation. Therefore the power flow in free space or non-conductive materials through a surface A , described by its normal vector $\mathbf{n}(\mathbf{a})$, dependent on the surface position vector \mathbf{a} can be calculated by:

$$\langle P \rangle = \iint_A \text{Re}(\mathbf{S}) \cdot \mathbf{n} \, da \quad . \quad (2.5)$$

2.2 Waves and the diffraction limit

Maxwell's equations (2.2c) and (2.2d) can be rewritten into two homogenous Helmholtz equations for \mathbf{E} - and \mathbf{B} -fields in free space ($\varepsilon_r = \mu_r = 1$ as well as vanishing σ and \mathbf{j}):

$$(\nabla^2 - \mathbf{k}^2) \mathbf{E} = 0 \quad (2.6)$$

$$(\nabla^2 - \mathbf{k}^2) \mathbf{B} = 0 \quad . \quad (2.7)$$

The simplest solutions in Cartesian coordinates are propagating plane waves:

$$\mathbf{E}(\mathbf{r}, t) = \mathbf{E}_0 e^{i\mathbf{k} \cdot \mathbf{r}} \quad (2.8)$$

$$\mathbf{B}(\mathbf{r}, t) = \mathbf{B}_0 e^{i\mathbf{k} \cdot \mathbf{r}} \quad (2.9)$$

, with the wave vector $\mathbf{k} \perp \mathbf{E} \perp \mathbf{B}$ pointing in the direction of propagation and $|\mathbf{k}| = 2\pi/\lambda$, where the vacuum wavelength λ is introduced. The wave vector is connected to the angular frequency via $\omega = c \cdot |\mathbf{k}| = 2\pi c/\lambda$, which is the linear free space dispersion relation.

Diffraction and refractive optical elements like lenses and mirrors are used in e.g. microscopes to focus collimated (i.e. parallel) plane waves into converging plane waves meeting in a focal volume (see Fig. 2.1(a)). The electromagnetic

energy is concentrated and can be used to image and probe e.g. fluorescing molecules. However, there is a fundamental limit for the minimal dimensions of the focal volume and, thus, for the resolution of any device relying on diffractive or reflective elements only.

The image generated by a microscope when looking at a perfect point light source is called point spread function (PSF). It is always blurred as the optics is not able to capture all k-vectors emitted by the point source (see also chpt. 2.3.1). The resolution Δr is the minimal distance between two nearby point sources, where their overlapping PSFs can still be distinguished. This is described by the Abbe-limit [12]:

$$\Delta r \approx 0.61 \frac{\lambda}{\text{NA}} \quad (2.10)$$

, introducing the numerical aperture $\text{NA} = n \cdot \sin \theta_{\text{max}}$, dependent on the refractive index n of the surrounding medium and the maximum light collection angle θ_{max} (Fig. 2.1(a)). In case of a microscope objective with e.g. $\text{NA} = 1.4$, two radiating point dipoles oriented perpendicular to the optical axis of the objective are indistinguishable below a distance of $\Delta r \approx 0.61/1.4 = 0.44$ times the emission wavelength λ . Clustered molecules with dimensions in the nm-range or below, thus, cannot be resolved by means of visible radiation with $\lambda \in [400, 800]$ nm. This is one of the main motivations to research nanoantennas, as they can circumvent the limited far-field resolution by accessing optical near-fields (see chpt. 3).

A full calculation of the vectorial fields of an objectives focus is beyond the scope of this work (compare e.g. chapter 3 to 4 in [16]). However, it is important to note that for large NAs the resulting fields show non-negligible polarization components in all three spatial directions (see Fig. 2.1(b)-(d)). They can be measured by scanning a point like source of linearly polarized light through the focus (chpt. 9 in [16]). This has to be kept in mind for all experiments with polarization dependent samples. Within this work it has been used to check the quality of a home-built confocal microscope.

Finally, it is worth mentioning that there is a difference between resolution, the ability to separate two nearby objects, and localization, the ability to measure the exact position of one single object. The latter can be performed with nm precision also for diffraction limited optics, since it depends on the

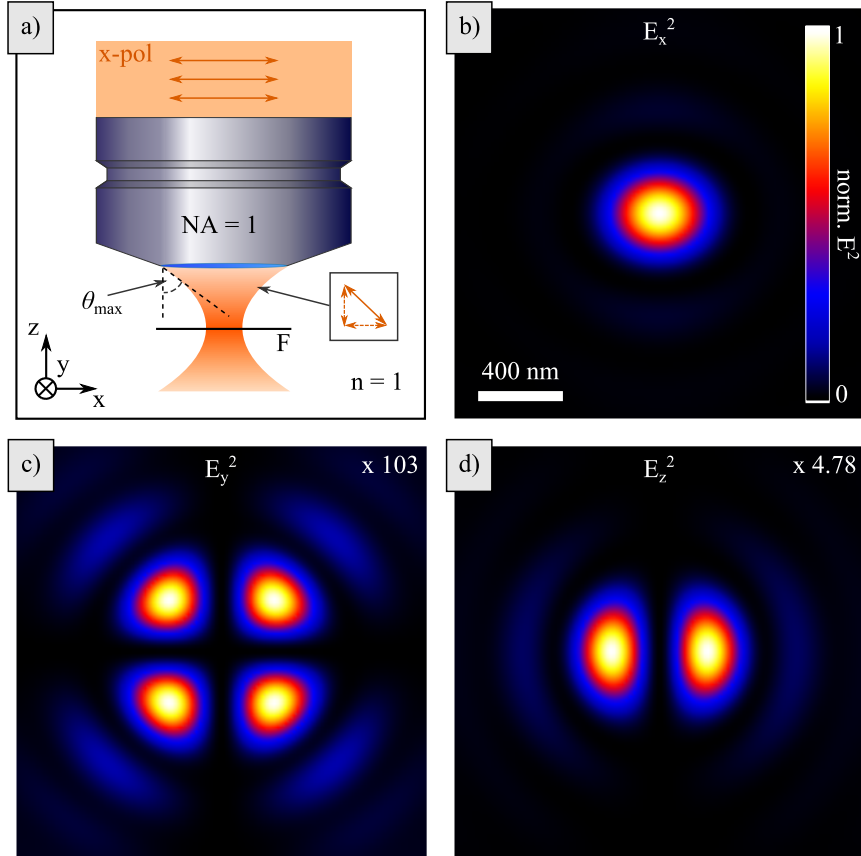


Figure 2.1: Properties of far-field focusing: a) sketch of a high NA objective situated in vacuum and illuminated with monochromatic, x -polarized plane waves. F denotes the focal plane, the inset depicts the polarization of a strongly diffracted beam gaining z -polarized field components. b)–d): Simulated normalized field intensity components E_x^2 , E_y^2 and E_z^2 in the focal plane of a $NA = 1$ objective in vacuum, when illuminated with monochromatic light of $\lambda = 650$ nm. The y - and z -components have been scaled up by a factor of 103 and 4.78 respectively.

ability to fit a model function to the measured PSF in space, hampered by the signal to noise ratio (SNR) only. Numerous methods like e.g. PALM and STORM represent the class of so-called *far-field nanoscopy* techniques, which can retrieve the PSF of single molecules even in clusters [42] (chemistry noble prize 2014).

The confocal principle In the year 1955 Minsky patented the confocal microscope [43], which allows imaging with a high SNR by spatially filtering the light in the detection path of an optical microscope by means of a pinhole.

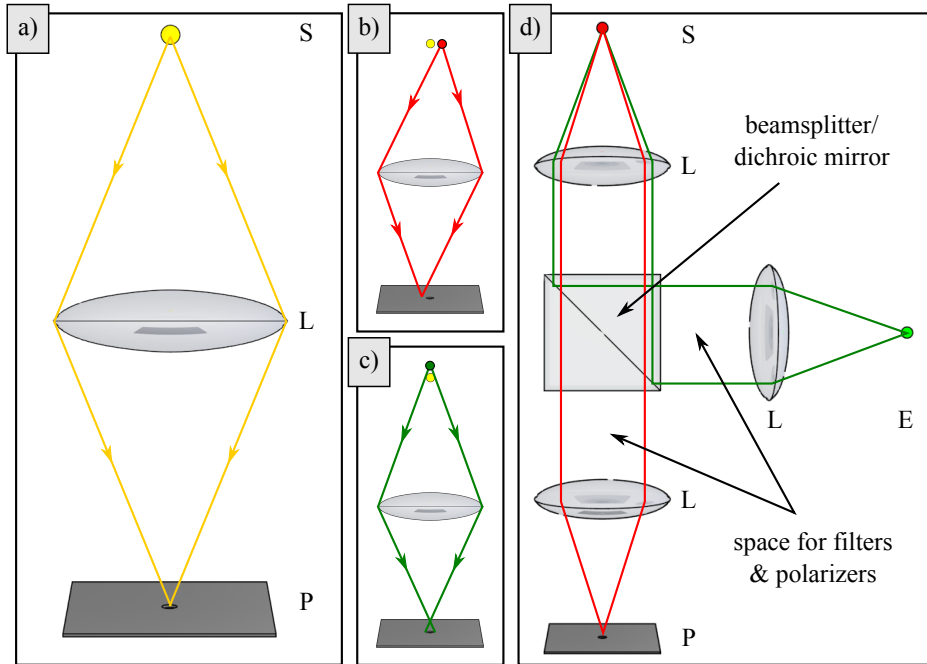


Figure 2.2: The confocal principle: a) The light emitted from a point like sample S is focused with a lens L onto a pinhole P. Light emitted from b) sources in the focal plane, but off the optical axis will be blocked mainly by the plate as well as c) light originating from sources on the optical axis but off the focal plane. d) Standard realization with a point like light source E collimated via a lens and directed to the sample S by means of a beam-splitter or a dichroic mirror.

The working principle is sketched in Fig. 2.2(a). Light emitted from a point source S situated in the first focal point of the imaging optics L is focused onto a pinhole P placed at the second focal point of L and, thus, can pass nearly unattenuated if focal spot and pinhole diameter are about equal. A detector placed behind the pinhole then registers the photons from the source. Light not originating from the first focal point will be mostly blocked instead (see Fig. 2.2(b) and (c)). An extended sample cannot be imaged in one shot, but has to be scanned through the focus. This increases image acquisition times, but also allows the optical sectioning of a 3D sample into layers perpendicular to the optical axis, enabling 3D optical microscopy [16].

In addition, illuminating the sample with a diffraction limited spot increases the resolution of a confocal microscope in x-y-direction by a factor of ≈ 1.3 [16], because the total point spread function PSF_{tot} of the optical system results

from the multiplication of the excitation and the detection PSF:

$$\text{PSF}_{\text{tot}} = \text{PSF}_{\text{exc}} \cdot \text{PSF}_{\text{det}} \quad (2.11)$$

A possible realization uses a single microscope objective for illumination and detection as sketched in Fig. 2.2(d) with a beam splitter or dichroic mirror for separating excitation and detection light path. This setup is comparably easy to optimize in experiment and allows the insertion of polarizers and filters without introducing optical errors, as the light beams between the lenses are collimated.

The confocal microscopy setup used in this work is described in chapter 6.

2.3 Quantum emitters as classical dipoles

This work focuses on the application of focusing optical antennas for the enhancement of quantum emitter (QE) excitation and emission. A QE within this context is a very small entity that – after excitation by a photon – is capable of emitting one single photon with a given wavelength via spontaneous emission. This process can be described by a quantum mechanical two-level system representing e.g. atoms, dye molecules, quantum dots and nano-diamonds with color centers (see Fig. 2.3(a) and chapter 9 in [16]) interacting with the fluctuations of a quantized electrical vacuum field in the framework of quantum electrodynamics (QED).

Fortunately, a QE much smaller than its emission wavelength can be treated classically as radiating point dipole with respect to emission pattern and emission power enhancement in inhomogeneous environments [15]. This allows to calculate the interaction between a single QE and a nanoantenna using Maxwell's equations (2.1).

2.3.1 Point dipole in free space

A point dipole oscillating with frequency ω and located at \mathbf{r}' can be described by a source current \mathbf{j}_p :

$$\mathbf{j}_p(\mathbf{r}) = -i\omega\mathbf{p}\delta(\mathbf{r} - \mathbf{r}') \quad (2.12)$$

, with \mathbf{p} being the dipole moment and $\delta(\mathbf{r})$ the Dirac delta function. To yield the electric fields originating from a given current distribution in free space, the *scalar Green's function*

$$G_0(\mathbf{r}, \mathbf{r}') = \frac{e^{ik|\mathbf{r}-\mathbf{r}'|}}{4\pi|\mathbf{r}-\mathbf{r}'|} \quad (2.13)$$

is needed (see e.g. [29]), solving the inhomogeneous Helmholtz equation for a point perturbation:

$$(\nabla^2 - k^2) G_0(\mathbf{r}, \mathbf{r}') = -\delta(\mathbf{r} - \mathbf{r}') \quad . \quad (2.14)$$

The electric fields resulting from an arbitrary current density \mathbf{j} can then be calculated via:

$$\mathbf{E}(\mathbf{r}) = i\omega\mu_0\mu \int_V \bar{\mathbf{G}}(\mathbf{r}, \mathbf{r}') \cdot \mathbf{j} \, dV \quad (2.15)$$

, where $\bar{\mathbf{G}}(\mathbf{r}, \mathbf{r}')$ is the *dyadic Greens function*, a second order tensor which can be derived from the scalar Greens function:

$$\bar{\mathbf{G}}(\mathbf{r}, \mathbf{r}') = \left(\bar{\mathbf{I}} + \frac{1}{k^2} \nabla \nabla \right) G_0(\mathbf{r}, \mathbf{r}') \quad . \quad (2.16)$$

Here $\bar{\mathbf{I}}$ is the second order unity tensor. For the current density of a point dipole eq. (2.12) the delta function and the integral in eq. (2.15) cancel each other, resulting in

$$\mathbf{E}_d = \omega^2 \mu_0 \bar{\mathbf{G}} \cdot \mathbf{p} \quad (2.17)$$

, as no magnetic materials are considered in this work and therefore $\mu = 1$. The resulting fields for a dipole localized at $\mathbf{r}' = \vec{0}$ are:

$$\mathbf{E}_d(\mathbf{r}) = \frac{1}{4\pi\epsilon_0} \frac{e^{ikr}}{r} \left\{ k^2 [(\mathbf{n} \times \mathbf{p}) \times \mathbf{n}] + \frac{1}{r} \left(\frac{1}{r} - ik \right) [3\mathbf{n}(\mathbf{n} \cdot \mathbf{p}) - \mathbf{p}] \right\} \quad (2.18a)$$

$$\mathbf{B}_d(\mathbf{r}) = \frac{1}{4\pi\epsilon_0} \frac{e^{ikr}}{r} k^2 \left(1 - \frac{1}{ikr} \right) \mathbf{n} \times \mathbf{p} \quad (2.18b)$$

, with $r = |\mathbf{r}|$ and $\mathbf{n} = \mathbf{r}/r$.

Dipole fields can be classified depending on the distance from the source:

(i) The *far-field regime* for distances with $\mathbf{k} \cdot \mathbf{r} \gg 1$ is described by the term proportional to r^{-1} , yielding spherical transverse waves traveling radially outwards with $\mathbf{E} \perp \mathbf{H} \perp \mathbf{k}$. They are transporting energy and information over long distances with the characteristic toroidal shaped far-field emission pattern showing vanishing emission power in the directions along the dipole axis

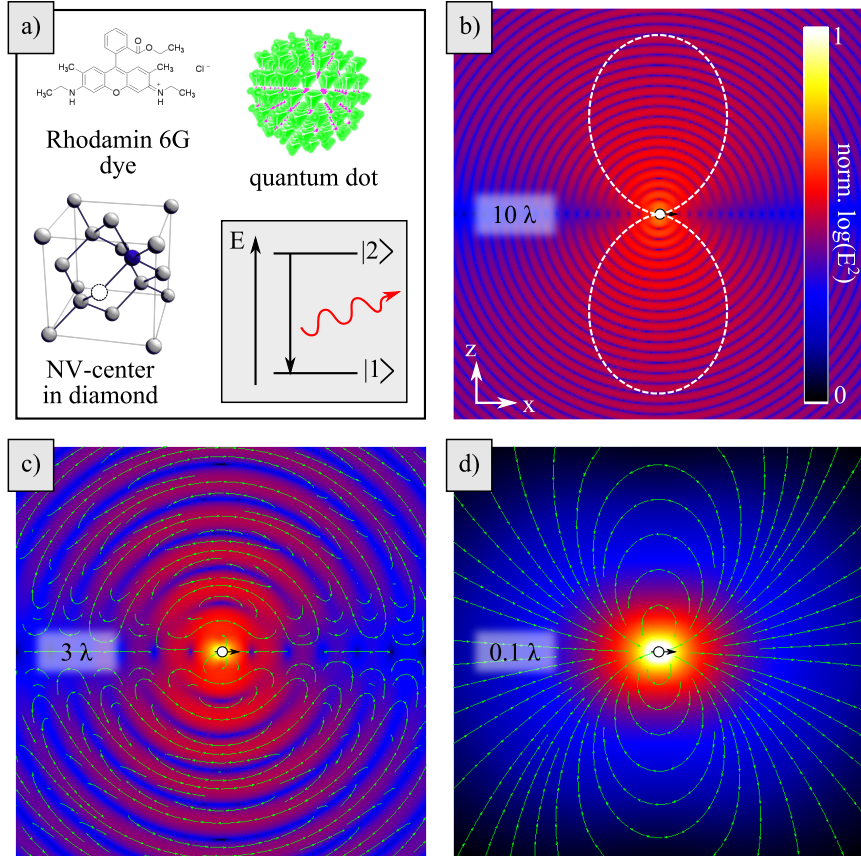


Figure 2.3: Properties of quantum emitter: a) Examples of quantum emitters, which in first approximation can be treated as two-level systems (inset: decay from the excited state $|2\rangle$ to the ground state $|1\rangle$ leads to the emission of a photon (red)): dyes, quantum dots or color centers in diamond (missing and/or replaced C-atoms). b)–d) Direction (green arrows) and normalized $\log(|\mathbf{E}^2|)$ (colored) of the fields in the x - z -plane originating from a radiating point dipole oriented along the x -axis in vacuum (white sphere with black arrow pointing in the direction of the dipole moment). The overall dimensions of the plots are denoted at their top center showing the far-field regime b) with the white dashed line being the planar cross section through the toroidal shaped emission pattern, intermediate regime c) and near-field regime d).

(Fig. 2.3(b)). These are the fields collected and analyzed by classical far-field optical microscopy.

(ii) In the *intermediate regime* with $\mathbf{k} \cdot \mathbf{r} \approx 1$ the fields are dominated by the terms proportional to r^{-2} (Fig. 2.3(c)).

(iii) The *near-field regime* with $\mathbf{k} \cdot \mathbf{r} \ll 1$ is proportional to r^{-3} . In contrast

to the far-field radiation pattern the strongest fields are concentrated along the dipole axis (Fig. 2.3(d)):

$$\mathbf{B}_d = \frac{1}{4\pi\epsilon_0} \frac{ik}{r^2} (\mathbf{n} \times \mathbf{p}) \quad (2.19)$$

$$\mathbf{E}_d = \frac{1}{4\pi\epsilon_0} \frac{3\mathbf{n}(\mathbf{n}\mathbf{p}) - \mathbf{p}}{r^3} \quad (2.20)$$

The electric fields are identical to the fields of a static dipole multiplied by the oscillation term $e^{i\omega t}$.

The mean power $\langle P \rangle$ radiated by a point dipole situated in free space with a constantly driven dipole moment is given by [29]:

$$\langle P \rangle = \frac{\omega^4}{12\pi\epsilon_0 c^3} \cdot |\mathbf{p}|^2 \quad (2.21)$$

This result originates from the surface integral eq. (2.5) of the Poynting vector over a closed spherical surface in infinite distance.

Quantum mechanically the emission process takes no time. However, the statistics of the excited states lifetime shows an exponential decay with a characteristic excited state life time τ . It defines the emission rate $\gamma = 1/\tau$, the amount of photons emitted per time, under the condition that the dipole is instantaneously re-excited after each emission event. In the classical representation the total power P_0 emitted by an excited point dipole in free space gives a measure of the time needed to emit all initial energy. Therefore, the emission rate γ can be directly identified as the damping constant in an undriven classical oscillator model, where a charge e with mass m oscillates with frequency ω [15]:

$$\frac{d^2}{dt^2}\mathbf{p}(t) + \gamma \frac{d}{dt}\mathbf{p}(t) + \omega^2\mathbf{p}(t) = 0 \quad (2.22)$$

This finally leads to:

$$P_0 = \frac{2e^2\omega^3}{3c^3m} \quad (2.23)$$

and, therefore, to an excited state life time of $\tau \approx 10$ ns for a QE in the optical wavelength regime. This is slow compared to other processes like internal losses like the generation of phonons and can be also explained by the size mismatch between QE and free space wavelength (see eq. (2.42)).

As just mentioned, realistic QEs have additional intrinsic decay channels, originating in e.g. additional energy levels. An additional parameter η_i can be

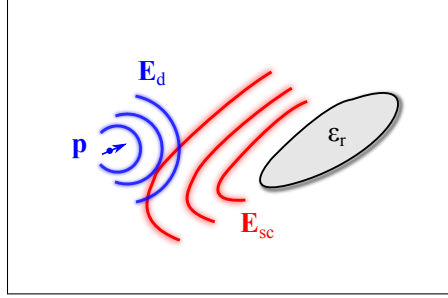


Figure 2.4: A dipole \mathbf{p} emits electric fields \mathbf{E}_d which are scattered by an object with a dielectric constant ϵ . The scattered field \mathbf{E}_{sc} will interact with the dipole and alter its emission power.

introduced, describing a QEs intrinsic quantum efficiency

$$\eta_i = \frac{P_{0,\text{rad}}}{P_{0,\text{rad}} + P_{0,\text{nr}}} \quad (2.24)$$

, yielding the amount of emitted photons per excitation event. Intrinsic losses $P_{0,\text{nr}}$ due to the existence of additional energy levels, the excited state can relax non-radiatively to, reduce the radiative power $P_{0,\text{rad}}$ reaching the far-field. η can be very small, like $\eta_i \approx 0.0001$ for carbon nanotube fluorescence [44] but can also be near unity as for semiconductor quantum dots coupled to photonic crystals [45].

2.3.2 Point dipole in arbitrary environments

If the environment of an excited dipole is inhomogeneous, its emission rate can change due to constructive or destructive self-interference with the back scattered field \mathbf{E}_{sc} as sketched in Fig. 2.4. The first theoretical description of spontaneous emission enhancement was given by Purcell in 1946 for a QE situated in a resonator cavity [46], theoretical and experimental results for simple geometries can be reviewed in the work of Drexhage [47].

To describe the influence of \mathbf{E}_{sc} it can be added to eq. (2.22) as driving force:

$$\frac{d^2}{dt^2}\mathbf{p}(t) + \Gamma_0 \frac{d}{dt}\mathbf{p}(t) + \omega_0^2\mathbf{p}(t) = \frac{e^2}{m}\mathbf{E}_{sc} \quad . \quad (2.25)$$

This leads to a relative change of the emission power compared to the free space case [16]:

$$\frac{P}{P_0} = 1 + \frac{6\pi\epsilon_0}{|\mathbf{p}|^2} \frac{1}{k^3} \text{Im}[\mathbf{p}^* \cdot \mathbf{E}_{sc}(\mathbf{r})] \quad . \quad (2.26)$$

Therefore, to realize maximum radiation enhancement the scattered field at the dipole location should be as strong as possible and pointing in the direction of the emission dipole moment. Equation (2.26) also takes into account the phase between dipolar moment and scattered field $\Delta\phi = \phi_{\text{sc}} - \phi_{\text{p}}$, which is distance dependent [47]. One can write

$$\text{Im} \{ \mathbf{E}_{\text{sc}}(\mathbf{r}_p) \cdot \mathbf{p}^* \} = |\mathbf{E}_{\text{sc}}(\mathbf{r}_p) \cdot \mathbf{p}| \text{Im} \{ e^{i\Delta\phi} \} \quad . \quad (2.27)$$

Quantum mechanically the emission rate γ_{21} of an excited QE in an arbitrary environment is given by Fermi's golden rule [15]:

$$\gamma_{21} \propto d_{21} \cdot \rho_{21}(\mathbf{r}_0, \omega) \quad (2.28)$$

, where d_{21} denotes the dipole transition matrix element and $\rho_{21}(\mathbf{r}, \omega)$ the local density of states (LDOS) defined by the environment at the position \mathbf{r}_0 of the SE for its emission frequency ω . The LDOS includes all final states of photons emitted from the excited QE and is for free space described by the Rayleigh-Jeans law [48]. The self-interaction in an environment can change the LDOS on a large scale. Cavities and photonic crystals [49] as well as plasmonic nanostructures (see chpt. 3.3.3) are the most effective means.

In the semi-classical picture it is possible to express the LDOS via the Green's tensor [16]:

$$\rho_{21}(\mathbf{r}_0, \omega) = -\frac{2\omega}{\pi} \text{Im} [\hat{\mathbf{p}} \cdot \bar{\mathbf{G}}(\mathbf{r}_0, \mathbf{r}_0, \omega) \cdot \hat{\mathbf{p}}] \quad (2.29)$$

, with $\hat{\mathbf{p}}$ the normalized vector pointing in the direction of the QE's dipolar moment.

This leads to the total QE emission rate [16]:

$$\gamma = \frac{\omega^3 |\mathbf{p}|^2}{2c^2 \varepsilon} \text{Im} [\hat{\mathbf{p}} \cdot \bar{\mathbf{G}}(\mathbf{r}_0, \mathbf{r}_0, \omega) \cdot \hat{\mathbf{p}}] \quad (2.30)$$

, which is formally identical to eq. (2.26). It turns out that the relative emission power enhancement of a classical dipole equals the relative emission rate enhancement of a quantum mechanical two level system [15]:

$$\frac{P}{P_0} = \frac{\gamma}{\gamma_0} \quad . \quad (2.31)$$

This allows to study the influence of e.g. optical antennas on the emission rate of quantum emitters by solving classical Maxwell's equation and, therefore, the use of numerical methods (see chpt. 4).

It is important to note, that eq. (2.30) captures the QEs *total* emission rate which further will be transformed into both radiative power, finally reaching the far-field, and non-radiative power, which adds to the thermal energy of the environment. Additionally, a non-unity QE quantum efficiency $\eta_i < 1$ changes with LDOS: as each decay channel has equal probability, additional emission channels will lower the relative amount of intrinsic decay events.

The Purcell effect describes the decreased excited state life time of a QE by connecting the LDOS with the quotient of a cavities mode volume V and the quality factor $Q = \Delta\nu_c/\nu_c$ of its resonance [46]. The maximum achievable spontaneous emission enhancement at the cavities resonance frequency ν_c and at the point of highest fields within the cavity is then given by the Purcell factor:

$$F_P = \frac{P}{P_0} = \frac{3}{4\pi^2} \frac{\lambda_c}{n} \cdot \frac{Q}{V} \quad (2.32)$$

, with $\lambda_c = c/\nu_c$ the free space resonance wavelength of the cavity and n the refractive index of the cavity volume. This derivation of the Purcell Factor, well-established for laser resonators and photonic crystal cavities, works only for a finite set of normal cavity modes within the resonator showing no (or in first approximation minimal) losses. Then, the mode volume is not diverging and is defined by

$$V = \frac{1}{\varepsilon_0 n^2} \int_V \varepsilon(\mathbf{r}) |\mathbf{E}(\mathbf{r})|^2 dV \quad . \quad (2.33)$$

2.4 Radiofrequency antennas

More than 120 years ago Heinrich Hertz experimentally discovered the transfer of energy through air via electromagnetic waves at radio frequencies (rf) [50]. He used two electrically powered devices – nowadays called antennas – that work as transducers between traveling far-field electromagnetic waves and localized currents/electric fields. The following review of rf-antenna principles will help to understand similarities and differences to optical antennas in later chapters.

2.4.1 General properties

Antennas are made from metal, with free electrons displaceable within their boundaries. At rf-frequencies metals behave like a perfect conductor with infinite conductivity $\sigma \rightarrow \infty$, shielding external fields instantaneously and completely. The shape of an antenna defines boundary conditions for the solution of the source-free Helmholtz equation eq. (2.14), leading to a distinct set of eigenmodes. Linear combinations of these eigenmodes can describe all possible current density patterns within the antenna geometry. The currents are sources to electric and magnetic fields outside the antenna volume, which can be classified into the three regions near-fields, intermediate fields and far-fields in dependence of the distance to wavelength ratio, exactly as for point dipoles (compare to chpt. 2.3).

Antenna modes can be driven by an external voltage or a current applied directly at the boundary making the antenna work as an emitter. Alternatively, impinging electromagnetic waves can drive internal electrical currents, which can be analyzed or used to power a device: the antenna then works as a receiver. A set of two antennas, one used as emitter and one as receiver, can thus transmit energy and/or information.

The feeding of an emitting antenna is usually realized by an electric generator connected via a thin transmission line in two fundamentally different variations: (i) current feeding: the transmission line is attached to a position, where the antenna mode has maximum current density. Charges flow between the transmission line and the antenna periodically. (ii) voltage feeding: the transmission line is attached to or ends in close distance to positions of high charge carrier density of the antenna mode. The charges within the antenna are only relocated within its volume.

The transmission of energy from an electrical generator to an antenna can be described by means of impedance (complex resistances) $Z = R + iX$ with R the real value called resistance and X the imaginary part called reactance. It can be modeled with a Thévenin equivalent circuit as depicted in Fig. 2.5 with Z_g for the generator impedance and Z_a the antenna impedance [22]. The condition for optimal power transmission from generator to antenna, leading to a minimal back reflection into the feeding transmission line, is given by [22]:

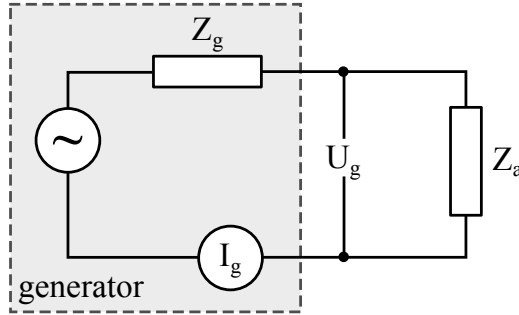


Figure 2.5: Thévenin equivalent circuit for an emitting antenna driven by a generator delivering a voltage U_g and a current I_g . Z_g and Z_a are the complex impedances of the generator and the antenna respectively.

$$X_a = -X_g \quad (2.34)$$

and called impedance matching. The real part of the antenna impedance describes all power loss channels:

$$R_a = R_\Omega + R_{\text{rad}} \quad (2.35)$$

, with R_{rad} being the loss of power due to emission of far-field radiation and R_Ω being the Ohmic losses generating heat. The later is vanishing for most rf-applications due to the material being nearly an ideal conductor, but will become an important quantity for optical antennas.

R_{rad} and thus the power emitted from a driven antenna can be calculated via the pointing vector (2.5). The fields \mathbf{E} and \mathbf{H} can be derived from the antennas current distribution \mathbf{j}_a via the vector potential $\mathbf{A}(\mathbf{r})$ [30]:

$$\mathbf{A}(\mathbf{r}) = \mu_0 \mu_r \int_V \mathbf{j}_a(\mathbf{r}') G_0(\mathbf{r}, \mathbf{r}') dV' \quad (2.36)$$

$$\mathbf{H}(\mathbf{r}) = \nabla \times \mathbf{A}(\mathbf{r}) \quad (2.37)$$

$$\mathbf{E}(\mathbf{r}) = \frac{1}{-i\omega\epsilon} \nabla \times \mathbf{H}(\mathbf{r}) \quad (2.38)$$

Here, G_0 is the Green's function eq. (2.13) of the inhomogeneous Helmholtz equation and V is the volume of the antenna. The radiation is not isotropic, but shows a radiation pattern $p(\theta, \phi)$, this is the angle dependent distribution of radiated far-field energy per solid angle at infinite distance. It holds:

$$P_{\text{rad}} = \int_0^\pi \int_0^{2\pi} p(\theta, \phi) \sin \theta d\phi d\theta \quad (2.39)$$

Antennas can also be understood as resonators, a combination of a capacitance due to charge accumulations at the antenna surface and a inductance due to oscillating electrical currents flowing along the wire. This allows to represent an antenna as a RLC-circuit defining its antennas impedance Z_a as well as its resonance frequency ω_0 . The damping of the resonance due to radiation can be described via the quality factor Q [16]:

$$Q = \frac{\omega_0}{\Delta\omega_0} = \frac{Z_0}{R_a} \quad (2.40)$$

, with $\Delta\omega_0$ being the width of the resonance and $Z_0 = \sqrt{\varepsilon_0/\mu_0}$ being the radiation resistance of vacuum. Therefore, to make an antenna a good resonator with a sharply defined resonance, R_a should be minimal. Neglecting Ohmic losses and following eq. (2.35), minimizing R will on the other side spoil the antennas function as emitter/receiver.

2.4.2 Characteristics of 1D antennas

Long, thin and straight wires of metal are easy to fabricate and show very good coupling to far-field radiation, making them the most common form of antennas. They are mathematically easy to describe since a major simplification is applicable: since the wire diameter is much smaller than the emitted wavelength (mm vs. m), the antenna can be described as 1D-system.

Oscillating currents on a straight 1D wire will be reflected at an open end with a phase shift of π . Wires with two open ends lead to standing wave patterns with vanishing currents as well as charge accumulations at the wire ends. For perfect metals current waves travel with the speed of light c and a given (rf-)frequency ν therefore leads to a wavelength of $\lambda = c/\nu$. For a wire antenna driven at its center in an infinitely narrow feed gap, maximum current amplitudes are expected at overall antenna lengths of $l = \frac{n}{2}\lambda$ with $n \in \mathbb{N}$.

The lowest modes $n = 1, 2$ are therefore the $\lambda/2$ - and the λ -antenna. For the $\lambda/2$ -antenna the current density amplitude is given as:

$$j(x) = j_0 \sin \left[k \left(\frac{l}{4} - |x| \right) \right], \quad |x| \leq \frac{\lambda}{4} \quad (2.41)$$

, with j_0 being the current amplitude at the feed point (resembling current feeding) and $k = 2\pi/\lambda$ being the wave number as depicted in Fig. 2.6(a).

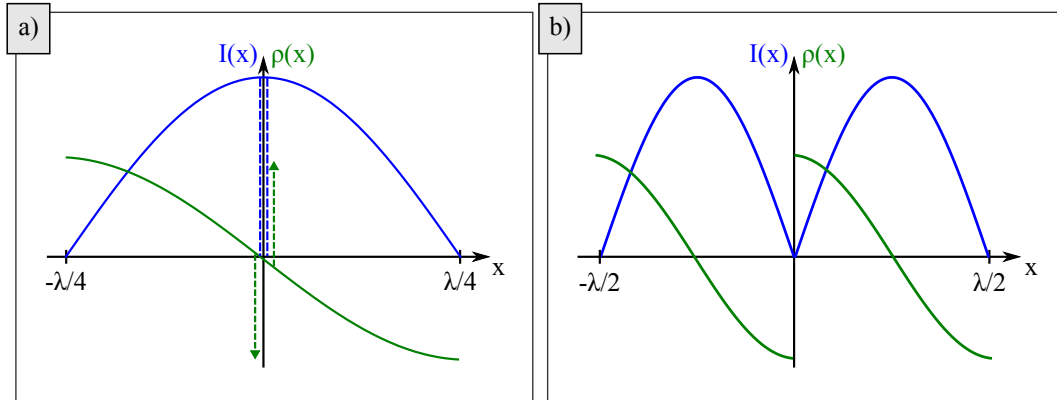


Figure 2.6: Time independent current density (blue) and charge density (green) amplitudes for a) a $\lambda/2$ -antenna and b) a λ -antenna [30]

Figure 2.6(b) shows a λ -antenna, where no current is flowing at the feed point (voltage feeding). This is the case for most optical antennas comprised of two particles, as will be described in chapter 3.3.3.

The total emission power P_r can be calculated easily only for a very short linear antenna with a length of $\Delta l \ll \lambda$. In this case it is given by $P_r = \frac{1}{2} I^2 \cdot R_r$, where I is the driving current flowing through the antenna and R_r is the radiation resistance given as [30]:

$$R_r = 80\pi^2 \left(\frac{l}{\lambda}\right)^2 . \quad (2.42)$$

This result is quite important, as the dependence of the radiation power to the antenna length relative to the emission wavelength explains classically the long excited state life time of quantum emitters (see section 2.3).

The far-field radiation patterns of linear antennas show cylindrical symmetry and are solely dependent on the angle θ between the antenna axis and the radial radiation direction [22]:

$$p(\theta, \varphi) \propto \frac{\cos(kl/2 \cos \theta) - \cos(kl/2)}{\sin \theta} . \quad (2.43)$$

The results for four antennas with different lengths are plotted in Fig. 2.7 as rotational symmetric cross section and as cylindrical projection of the full upper half space¹. Figure 2.7(a) shows the polar coordinate system used to plot

¹Introduced for better comparison with the results of complex shaped antennas without cylindrical symmetry in chpt. 7.

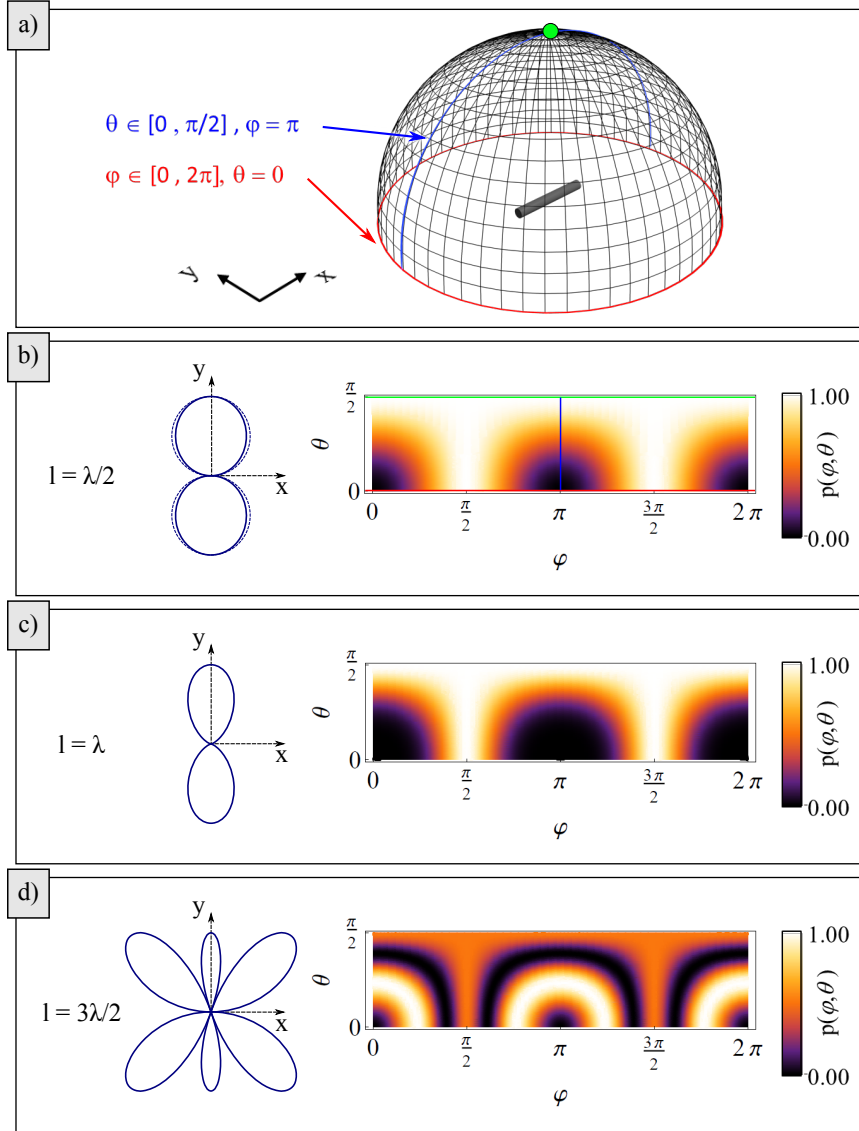


Figure 2.7: Far-field radiation patterns of linear 1D radio-frequency antennas oriented along the x -axis. a) Visualization of the used polar coordinate system with colored lines for orientation in the cylindrical projections. b)-d) radiation pattern for $l = \lambda/2$, λ and $3\lambda/2$. The left plot shows the cross section in the x - y -direction, the right a density plot of a cylindrical projection (see text for discussion). Additionally in b) the cross section for $l = 0.05\lambda$ is added as dashed line.

the 2D-projection of the 3D radiation pattern, which is identical to the Miller cylindrical projection used for cartographic maps [51]. Figures 2.7(b) and (c) show the cross sections of the typical doughnut shaped emission pattern for short dipolar antennas. As the antenna length increases, the maximum emission perpendicular to the antenna axis is more pronounced, until at $l \approx 1.2\lambda$ the emission pattern develops additional lobes [30]. This is caused by multiple dipoles on the antenna wire interfering with each other in the far-field, which is only possible if the antenna length is larger than the radiation wavelength. For the case of very short antennas – like point dipoles (see chpt. 2.3) or small metal particles (see chpt. 3.2) – the dashed line in Fig. 2.7(b) describes the dipolar emission pattern, showing the least directivity D . The directivity D of an antenna is a measure for the deviation of an antennas radiation pattern from isotropic spherical radiation into the full solid angle of 4π . It is defined as the maximum of the directive gain

$$D = \max(D(\theta, \varphi)) \quad \text{with} \quad (2.44)$$

$$D(\theta, \varphi) = \left(\frac{4\pi \cdot p(\theta, \varphi)}{P_{\text{rad}}} \right) \quad . \quad (2.45)$$

P_{rad} is the integrated radiated power, defined in eq. (2.39). Where the isotropic radiator would have $D = 1$ an ideal thin wire $\lambda/2$ -dipole antenna has a directivity of $D_{\lambda/2} = 1.64$ and a QE has $D_{\text{QE}} = 1.5$. The directivity can also be written in decibel normalized to the isotropic radiator: $D[\text{dBi}] = 10 \cdot \log_{10}(D)$.

2.4.3 Reciprocity theorem

The reciprocity theorem is a powerful tool to describe the power transfer between two radio-frequency antennas [30] as well as the data acquisition and deconvolution for scanning optical near-field microscopy (SNOM) [52]. The reciprocity theorem exists in different theoretical formulations [53]. The *Lorentz-lemma* is the most concrete, connecting two source currents \mathbf{j}_1 and \mathbf{j}_2 in different volumes made from conductive material via their generated electrical fields \mathbf{E}_1 and \mathbf{E}_2 (see Fig. 2.8):

$$\int \mathbf{E}_1 \cdot \mathbf{j}_2 dV = \int \mathbf{E}_2 \cdot \mathbf{j}_1 dV \quad . \quad (2.46)$$

Together with the definition of the electrical power (compare with eq. (2.4)):

$$P_{\text{el}} = \mathbf{j} \cdot \mathbf{E} \quad (2.47)$$

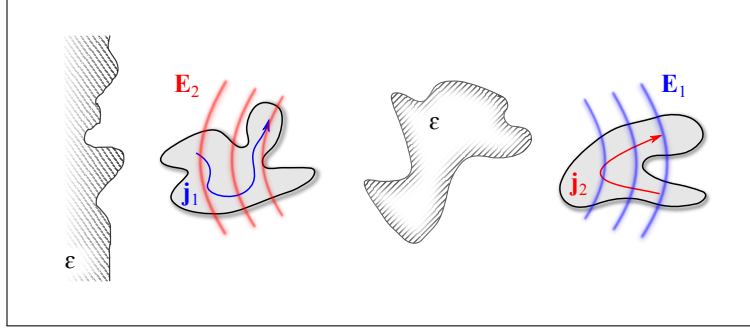


Figure 2.8: Setting for the reciprocity theorem in this work: Two volumes made from conductive materials situated in free space and with intrinsic currents \mathbf{j}_1 and \mathbf{j}_2 are sources of the respective fields \mathbf{E}_1 and \mathbf{E}_2 which penetrate the other particle. The environment can incorporate other particles or surfaces with a dielectric constant ε (figure originally composed for [54]).

, reciprocity is identical to a symmetry of energy transfer between given current patterns or modes: $P_{1 \rightarrow 2} = P_{2 \rightarrow 1}$.

For the deduction of the Lorentz-lemma we begin with two source currents $\mathbf{j}_{1,2}$ and their resulting fields $\mathbf{E}_{1,2}$ obeying Maxwell's equations :

$$\nabla \times \mathbf{E}_{1,2} = -i\omega\mu\mathbf{H}_{1,2} \quad (2.48)$$

$$\nabla \times \mathbf{H}_{1,2} = -i\omega\varepsilon\mathbf{E}_{1,2} + \mathbf{J}_{1,2} \quad . \quad (2.49)$$

These can be used to establish the following relationship:

$$\nabla \cdot (\mathbf{E}_1 \times \mathbf{H}_2 - \mathbf{E}_2 \times \mathbf{H}_1) = \mathbf{E}_2 \cdot \mathbf{J}_1 - \mathbf{E}_1 \cdot \mathbf{J}_2 \quad . \quad (2.50)$$

By integration over the whole volume containing the currents and applying the divergence theorem on the left side of the equation, one gets:

$$\oint (\mathbf{E}_1 \times \mathbf{H}_2 - \mathbf{E}_2 \times \mathbf{H}_1) d\mathbf{S} = \int (\mathbf{E}_2 \cdot \mathbf{J}_1 - \mathbf{E}_1 \cdot \mathbf{J}_2) dV \quad . \quad (2.51)$$

This is correct as long as the integration volume contains the two source currents. By setting its shape spherical and increasing its radius to infinity $r \rightarrow \infty$ one can rework the left side of eq. (2.51). Since at infinity every far-field electromagnetic wave can be decomposed into spherical waves, it fulfills the condition:

$$E_\theta = \eta H_\phi \quad \text{and} \quad E_\phi = \eta H_\theta \quad (2.52)$$

, stating that perpendicular E - and B -fields just differ by a constant factor η . The integral on the left side of eq. (2.51) therefore equals zero and one yields finally the Lorentz-lemma eq. (2.46).

The Lorentz-Lemma is used within this work to calculate the emission enhancement of quantum emitters near an optical antenna, by numerically evaluating the antennas mode under Gaussian excitation. Additionally this version of reciprocity was applied in a work about quantum emitter detection via single mode fibers, which will not be presented here [54].

Another version of reciprocity is the Green's function reciprocity:

$$\bar{\mathbf{G}}(\mathbf{r}_1, \mathbf{r}_2) = \bar{\mathbf{G}}(\mathbf{r}_2, \mathbf{r}_1) \quad (2.53)$$

, which has in this form first been introduced in the text book by Julian Schwinger [55].

Its derivation starts with the solution of the extended Poisson equation [55], which describes the electric potential at positions $\mathbf{r}_{1/2}$ of a (quasi-)static point charge located at \mathbf{r} in a medium described by a local ε :

$$-\nabla [\varepsilon(\mathbf{r}) \nabla \bar{\mathbf{G}}(\mathbf{r}, \mathbf{r}_1)] = 4\pi\delta(\mathbf{r} - \mathbf{r}_1) \quad (2.54)$$

$$-\nabla [\varepsilon(\mathbf{r}) \nabla \bar{\mathbf{G}}(\mathbf{r}, \mathbf{r}_2)] = 4\pi\delta(\mathbf{r} - \mathbf{r}_2) \quad . \quad (2.55)$$

By subtracting eq. (2.55) from eq. (2.54) after multiplication with $\bar{\mathbf{G}}(\mathbf{r}, \mathbf{r}_{1/2})$ respectively, one yields:

$$\begin{aligned} \nabla \{ \varepsilon(\mathbf{r}) [\bar{\mathbf{G}}(\mathbf{r}, \mathbf{r}_1) \nabla \bar{\mathbf{G}}(\mathbf{r}, \mathbf{r}_2) - \bar{\mathbf{G}}(\mathbf{r}, \mathbf{r}_2) \nabla \bar{\mathbf{G}}(\mathbf{r}, \mathbf{r}_1)] \} = \\ = 4\pi [\delta(\mathbf{r} - \mathbf{r}_1) \bar{\mathbf{G}}(\mathbf{r}, \mathbf{r}_2) - \delta(\mathbf{r} - \mathbf{r}_2) \bar{\mathbf{G}}(\mathbf{r}, \mathbf{r}_1)] \quad . \quad (2.56) \end{aligned}$$

The left side of this equation has been obtained using additionally the identity [55]:

$$\phi \nabla \cdot (\lambda \nabla \psi) - \psi \nabla \cdot (\lambda \nabla \phi) = \nabla \cdot [\lambda(\phi \nabla \psi - \psi \nabla \phi)] \quad . \quad (2.57)$$

In the next step both sides of eq. (2.56) are integrated over the volume of a large sphere S containing all points $\mathbf{r}, \mathbf{r}_1, \mathbf{r}_2$:

$$\begin{aligned} \frac{1}{4\pi} \oint_S [\{ \varepsilon(\mathbf{r}) [\bar{\mathbf{G}}(\mathbf{r}, \mathbf{r}_1) \nabla \bar{\mathbf{G}}(\mathbf{r}, \mathbf{r}_2) - \bar{\mathbf{G}}(\mathbf{r}, \mathbf{r}_2) \nabla \bar{\mathbf{G}}(\mathbf{r}, \mathbf{r}_1)] \}] d\mathbf{S} = \\ = \bar{\mathbf{G}}(\mathbf{r}_1, \mathbf{r}_2) - \bar{\mathbf{G}}(\mathbf{r}_2, \mathbf{r}_1) \quad (2.58) \end{aligned}$$

, where the divergence theorem was applied to the left side. For an infinitely large integration sphere with $R \rightarrow \infty$ the integral vanishes, since the Green's functions are proportional to $1/R$, hence $\bar{\mathbf{G}} \nabla \bar{\mathbf{G}} \propto 1/R^3$. Therefore, one obtains eq. (2.53).

The Green's function reciprocity will be used in chapter 9 to establish a novel mode-matching formalism for describing the coupling between an optical antenna and a quantum emitter.

Chapter 3

Focusing antennas for visible light

The very first idea that might come to ones mind who wants to realize optical antennas working in the visible light regime is to scale down geometries suggested by radio-frequency (rf) antenna theory. This leads to structures with dimensions of several hundreds of nanometers, which are nowadays established building blocks for real photonic applications. Yet, optical antennas behave different to their rf-counterparts due to metals not being ideal conductors in the optical frequency regime anymore, showing loss and dispersion instead. Consequently, this chapter starts describing the response of gold at visible frequencies, as representative for plasmonic materials which is used within this work exclusively.

Next, plasmon-polaritons – coupled oscillations of electromagnetic waves and electrons – will be introduced as the physical basis of optical antennas, which will then be described together with an overview over possible applications. Essential properties of optical antennas applied for focusing light will be explained at the example of a linear two-arm geometry. Then, the interaction between quantum emitters (QEs) and optical antennas is reviewed together with attempts to model the underlying physics based on the two established concepts 'impedance' and 'Purcell factor'. Finally the state-of-the art of design guide lines for optimizing focusing antennas is presented.

3.1 The dielectric function of gold

Despite optical antennas consisting from metallic nanoparticles, the number of electrons is in many cases sufficient to describe the material response by the macroscopic semi-classical Drude-Lorentz-bandstructure model [29]. Only for metal particles with lateral dimensions smaller than 10 nm, extended models have to be introduced (see e.g. [31, 56]), which will not be discussed within this work.

The description of metals within the framework of Maxwell's equations (2.2) is realized via the frequency dependent permittivity $\varepsilon_r(\omega)$ and permeability $\mu_r(\omega)$ (see eq. (2.3)), the latter being set to unity within this work. For metals the permittivity, also called dielectric function, is a complex quantity $\varepsilon_c(\omega) = \varepsilon'(\omega) + i\varepsilon''(\omega)$. By comparison with the forth Maxwell's equation (2.2d) the imaginary part can be related to the conductivity σ :

$$\varepsilon''(\omega) = \frac{i\sigma(\omega)}{\varepsilon_0\omega} \quad (3.1)$$

, yielding a simplified version:

$$\begin{aligned} \nabla \times \mathbf{H} &= -i\omega\varepsilon_0\varepsilon_r\mathbf{E} + \sigma\mathbf{E} = -i\omega\varepsilon_0 \left(\varepsilon - \frac{\sigma}{i\omega\varepsilon_0} \right) \mathbf{E} \\ &= -i\omega\varepsilon_0\varepsilon_c\mathbf{E} \quad . \end{aligned} \quad (3.2)$$

In the rf-regime ε_c describes a perfect conductor without any resistance. Charges always move in surface layers very thin compared to all device dimensions and can be treated as surface currents. They shield impinging oscillating electromagnetic fields from the bulk material instantaneously.

This is not the case anymore for visible light with frequencies near the metal plasma-frequency ω_p , where the bandstructure-dependent effective mass m^* of the conduction electrons is not negligible anymore. ω_p is defined as:

$$\omega_p = \sqrt{\frac{Ne^2}{\varepsilon_0 m^*}} \quad (3.3)$$

, where N is the free electron density, $e = -1.6022 \cdot 10^{-19}$ C the elementary electron charge and ε_0 the vacuum permittivity. Gold has a plasma frequency of $\nu_p = \omega_p/(2\pi) = 2.183 \cdot 10^{15}$ Hz, which resembles to a near UV wavelength of $\lambda_p = 137$ nm. In general incident waves with $\lambda > \lambda_p$ will be reflected by a metal

while wavelengths $\lambda < \lambda_p$ will be absorbed or transmitted due to the phase difference between photons and oscillating electrons. Therefore, visible light will be reflected by Au like rf-waves but the proximity to λ_p leads to a slightly delayed response to external fields and, thus, to an increased penetration depth as well as to absorption due to Ohmic losses.

A simple way to describe the dielectric function of metals is the Drude model (described in detail in e.g. [57]), which takes only the free electron gas into account:

$$\varepsilon_D(\omega) = 1 - \frac{\omega_p^2}{\omega^2 - i\gamma\omega} \quad (3.4)$$

, with γ being a damping constant taking into account the mean free electron path inside the metal. Fitting eq. (3.4) to experimental data of e.g. Johnson and Christy [58] yields a good representation of the dielectric function from infinite wavelengths (= static fields) down to about $\lambda = 700$ nm (upper panel Fig. 3.1).

Visible light of higher energies can excite interband transitions, lifting bound electrons from the valence band to unoccupied states in the conduction band. To describe the resulting additional response one can add a term $\varepsilon_L(\omega)$ to the Drude-model resembling a Lorentz-oscillator with frequency ω_0 , thus yielding the Drude-Lorentz-model:

$$\varepsilon_{DL}(\omega) = \varepsilon_D(\omega) + \varepsilon_L(\omega) \quad (3.5)$$

$$\text{with } \varepsilon_L(\omega) = 1 + \frac{\tilde{\omega}_p^2}{(\omega_0^2 - \omega^2) - i\tilde{\gamma}\omega} \quad (3.6)$$

The valence band electrons are described by a separate plasma frequency $\tilde{\omega}_p$ and damping constant $\tilde{\gamma}$. The result for adding a single Lorentz-oscillator with an energy of 2.64 eV ($\lambda = 470$ nm) is depicted in the center of Fig. 3.1. The fit is improved down to a wavelength of $\lambda \approx 500$ nm.

The Drude-Lorentz-model can fit arbitrary dielectric functions by adding an infinite number of Lorentz-oscillators. But this resembles a collection of fit parameters without underlying physical principles. Instead, Etchegoin et al. developed a method of critical points, introducing asymmetric Lorentz-peaks [59]. Their fit of ε is shown in the lower panel of Fig. 3.1. Despite the original publication presenting slightly incorrect model parameters, it still provides a quite decent fit which was used in all simulations in this work for

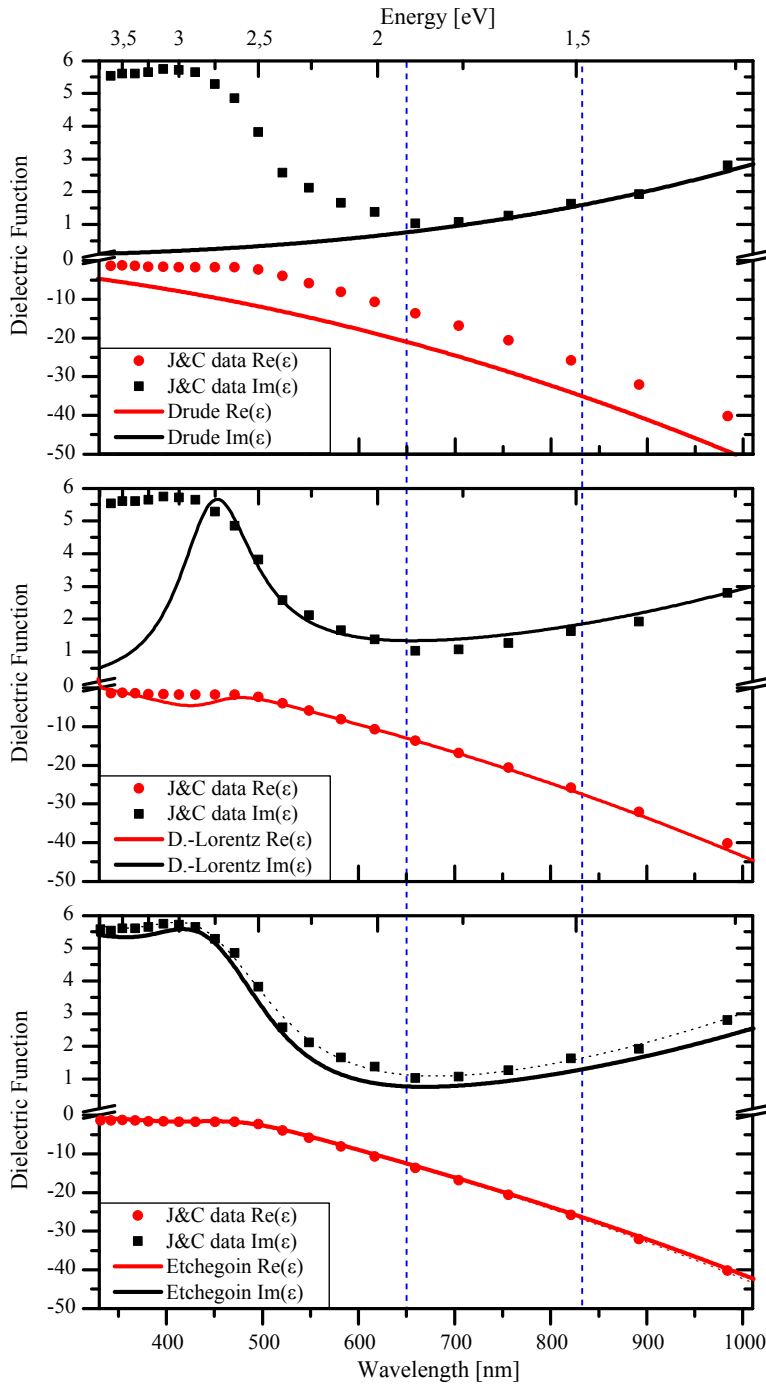


Figure 3.1: Real and imaginary part of the dielectric function $\epsilon_c(\omega)$ for gold. The data points are measured values from [58] while the lines show fits using a simple Drude-model (top), a Drude-Lorentz-model with a single interband transition at $\lambda_0 \approx 470$ nm (center) and the Etchegoin model [59] (bottom; see text for explanation). The blue lines denote $\lambda = 650$ nm and 830 nm.

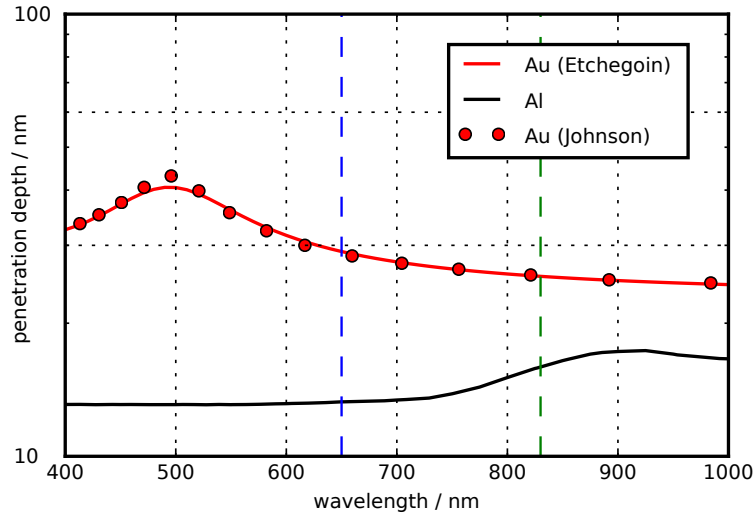


Figure 3.2: Wavelength-dependent penetration depth of gold (red; modeled after [60]) and aluminum (black; data from [63]). The red dots are the gold data from Johnson and Christy [58] for comparison. Also denoted as dashed lines are the wavelengths of 650 nm (blue) and 830 nm (green) which get important in later chapters.

full comparability (solid line). The erratum [60] gives better model parameters and the resulting ε is added as dashed line.

The dielectric function is connected to the complex refractive index $\tilde{n} = n + i\kappa$ via:

$$\varepsilon' = n^2 - \kappa^2 \quad \text{and} \quad \varepsilon'' = 2n\kappa \quad (3.7)$$

, with κ describing the damping of waves inside the material. This allows to compute the penetration depth d of electromagnetic radiation into the metal, where the field intensity is reduced by a factor of $1/e^2$:

$$d = \frac{\lambda}{4\pi\kappa(\lambda)} \quad . \quad (3.8)$$

The penetration depth of gold is plotted in Fig. 3.2 together with the values for aluminum (Al). Recent literature proposes Al as a promising future material for plasmonics in the near UV range (e.g. [61]) due to its high plasma frequency of $\nu_p = 3.57 \cdot 10^{15} \text{ s}^{-1}$ ($\lambda_p \approx 83 \text{ nm}$), when the drawback of oxidation in ambient conditions is taken into account [62].

It has to be mentioned that for the dielectric function of gold the data set of Johnson and Christy [58] has been taken as standard for the majority of

publications. Yet the morphology of thin gold films used as fabric for plasmonic structures can vary drastically, which also changes the effective optical response. Olmon et al. [64] have examined gold surfaces realized by three different methods (evaporation, template stripping and single crystalline growth). Their results deliver a low error data basis for better material fits, however, they do not vary much from Johnson and Christy values. Despite small changes in resonance positions and quantum efficiencies, the fundamental discussion of later results will not be affected.

3.2 Plasmons

Solving Maxwell's equations (2.2) for a planar interface separating a metal from a dielectric yields in addition to free-space radiation another homogeneous solution, a surface wave traveling along the boundary plane as sketched in Fig. 3.3(a). These waves involve not only fields, but also charge density oscillations of the metal electrons near the surface and are therefore called *surface-plasmon-polariton* (SPP). They can be described quantum-mechanically as coupled state between photons (polariton) and charge density waves (plasmons)¹. The term *plasmonics* refers mostly to photonic (information-)technology based on surface-plasmon-polaritons.

The metal halfspace is described by a complex dielectric function $\varepsilon_m(\omega) = \varepsilon'_m(\omega) + i\varepsilon''_m(\omega)$ and the dielectric by a real dielectric function $\varepsilon_d(\omega)$, leading to a solution for the electric fields given as [1]:

$$\mathbf{E}_{\text{SPP}} = \begin{pmatrix} E_{\text{SPP},x} \\ 0 \\ E_{\text{SPP},z} \end{pmatrix} e^{ik_x x - i\omega t} e^{ik_z z} \quad (3.9)$$

, where the boundary plane coincides with the x - y -plane and the wave travels in positive x -direction. For a given free space wavelength λ the plasmon wavelength $\lambda_{\text{SPP}} = 2\pi/k_{\text{SPP}}$ is shorter than the free space wavelength:

$$\lambda_{\text{SPP}} = \sqrt{\frac{\varepsilon'_m + \varepsilon_d}{\varepsilon'_m \cdot \varepsilon_d}} \lambda \quad . \quad (3.10)$$

¹In this work we are never considering bulk plasmons which can't couple to free space photons (read [65] for a limiting case in thin shells). We will from now on use the term plasmon as a convenient abbreviation of SPP – like in most of the recent literature.

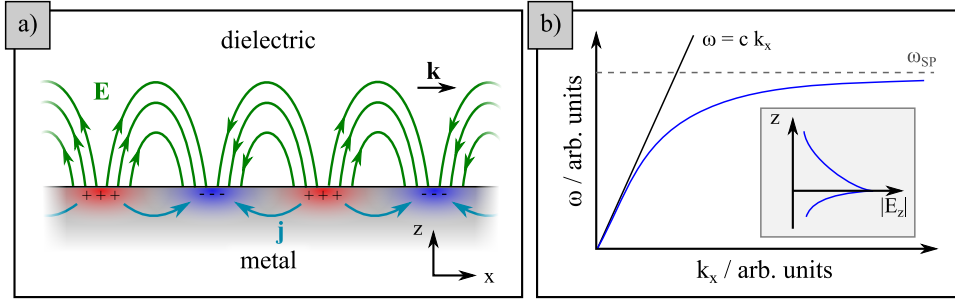


Figure 3.3: Surface plasmon properties. a) Sketch of surface plasmons wave traveling along an metal-dielectric interface in positive x -direction with a \mathbf{k} -vector \mathbf{k} . Fields \mathbf{E} are coupled to charge density oscillations built up by the current density \mathbf{j} , which give rise to a confinement of electromagnetic energy in z -direction. b) Qualitative sketch of the plasmon dispersion relation (blue) together with the light line (black). The dashed line is the surface plasma frequency ω_{SP} , being the asymptote for large \mathbf{k} -vectors. The inset shows the imaginary z -component of the fields, decaying exponentially with distance from the surface.

This is also visible in the plasmon dispersion relation, which is qualitatively given in Fig. 3.3(b)². For low frequencies the linear dispersion of light (light line – black) and the plasmon dispersion (blue) are nearly identical. For larger frequencies the plasmon \mathbf{k} -vector increases faster, leading to a shortened wavelength compared to the light line, as the mass of the metal electrons inhibits the oscillation amplitude. There is an upper limit to the plasmon frequency, which is material-dependent and is defined, where the real part of its dielectric function becomes $\varepsilon'_m = 1$.

The k_x -vector of the SPP has a non-zero imaginary part, describing a damped propagation due to Ohmic losses. The k_z -vector is purely imaginary, describing fields decaying exponentially perpendicular to the surface called evanescent waves or near-fields, which are confined to the interface as qualitatively illustrated in the inset of Fig. 3.3(b). The decay lengths are 28 nm / 328 nm for gold and vacuum respectively at a free-space wavelength of 633 nm.

The qualitative behavior does not differ, when changing the geometry from an interface to a thin metal layer or wire. Yet, the plasmon wavelength becomes

²This is simplified to loss-free metals. The implications of lossy metals on the dispersion will not be discussed here (see chapter 12 in [16]).

also dependent on the layer thickness or wire diameter a , when a is in the range of the penetration depth d of the fields into the material, which is for gold in the range of 10 – 20 nm (see Fig. 3.2). The charge density accumulations then interact with each other through the material, and the plasmon wavelength is getting even shorter compared to the interface case. For wires a linear relation of SPP-wavelength in dependence of a can be identified for a constant excitation wavelength λ [66]:

$$\lambda_{\text{SPP}} = n_1(a) + n_2(a) \left(\frac{\lambda}{\lambda_p} \right) \quad (3.11)$$

, with $\lambda_p = (2\pi c)/\omega_p$ being the plasma wavelength of the metal and n_1 and n_2 being factors with the dimension of a length, dependent on the material and linearly on a .

3.2.1 Particle plasmons

Solving the homogeneous Helmholtz equation (2.14) for a metallic particle with dimensions about or smaller than the excitation wavelength yields solutions describing plasmonic oscillations confined in all three dimensions, called particle plasmon-polaritons (PPP). They show Lorentzian resonances for simple geometries like spheres or elongated rods with the resonance frequency dependent on material and shape, allowing a broad range of possible resonance wavelengths from the near UV to the near IR as gathered in Fig. 3.4.

The first applications using chemically synthesized colloidal gold nanospheres were already realized in the roman empire to foster colored glass (Lykurgos cup) – despite lacking knowledge of the underlying fundamentals or of the existence of nanoparticles. Systematic experimental studies started around 1850 by Michael Faraday [68] and the accompanying theory was developed as early as 1908 by Gustav Mie [69]. Only in the last 20 years the research on metallic nanostructures has grown exponentially, and a wide range of new shapes as well as applications have been developed, yet, the fundamental interactions between light, metallic nanoparticles and their environment are still an active research topic, e.g. to understand surface enhanced Raman scattering (SERS).

The inset of Fig. 3.4 shows a spherical particle building up a dipolar moment due to a plasmon excited by a plane wave in vacuum. The wave will loose

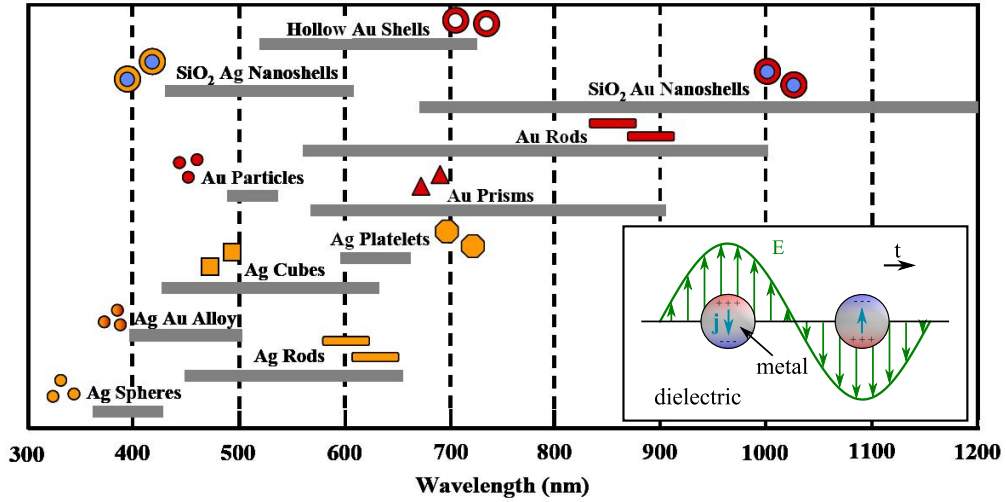


Figure 3.4: Properties of particle plasmons. Achievable resonance wavelengths of particles plasmonic resonances for metallic nanoparticles dependent on shape and material (reprinted with permission from [67]). Inset: Sketch of current densities \mathbf{j} oscillating in a nanoparticle when excited by an external harmonic field \mathbf{E} , leading to charge carrier accumulations at its boundaries. Shown are two snapshots of the dipolar mode with $\Delta t = 1/2\omega$ with neither charges nor current vanishing.

energy upon the interaction, therefore, a hypothetical geometric area called extinction cross section σ_{ext} is introduced to link incoming power P_{inc} and lost power P_{ext} :

$$P_{\text{ext}} = \frac{P_{\text{inc}}}{A} \cdot \sigma_{\text{ext}} \quad (3.12)$$

, with A denoting the area of the incoming planar wave front. σ_{ext} is made up from two components:

$$\sigma_{\text{ext}} = \sigma_{\text{sc}} + \sigma_{\text{abs}}. \quad (3.13)$$

σ_{sc} is the scattering cross section, covering the re-radiation of energy by the excited particle mode into free space with a change in k -vector direction. σ_{abs} is the absorption cross section, describing the conversion of energy into heat due to Ohmic losses. Both cross sections are a figure of merit for the coupling of energy from far-field radiation to energy localized in and near the nanoparticle, which is maximal for $\sigma_{\text{sc}} = \sigma_{\text{abs}}$ [70].

The resonance frequency of elongated particles follows a linear scaling law with respect to the particles reciprocal aspect ratio $AR^{-1} = A/l$, which is the ratio between its geometrical cross section A and its length l . This can

be understood qualitatively by a Fabry-Perot-resonator model where a traveling wave with diameter dependent effective wavelength λ_{eff} (see eq. (3.11)) is reflected on both wire ends and builds up a standing wave. We take a closer look at a second representation using a mass-spring-model as sketched in Fig. 3.5(a) [71], which will be described in the following.

The free electron gas is displaced by Δx under the influence of external fields. The positive and negative charge surplus at the rod ends are assumed to sit in a single point, leading to a Coulomb force F_C , which is set equal to a restoring force $F_r = \Delta x \cdot D$ of a fictive spring-mass system with a spring constant D . The mass m of all moving electrons is given by $m = A \cdot l \cdot n \cdot m_e$ with n being the electron number density and $m_e = 9.109 \cdot 10^{-31}$ kg the electron mass. F_C is derived from the potential energy in dependence of the electron gas displacement Δx assuming the charges located in two points:

$$W(\Delta x) = \frac{1}{4\pi\epsilon_0} \frac{(ne \cdot A\Delta x)^2}{l} \quad (3.14)$$

, with $e = 1.60 \cdot 10^{-19}$ C the elementary charge. Derivation with respect to Δx yields the force:

$$F(\Delta x) = -\frac{\partial W(\Delta x)}{\partial \Delta x} = -\frac{1}{2\pi\epsilon_0} \frac{(ne \cdot A)^2}{l} \cdot \Delta x \stackrel{!}{=} -D\Delta x \quad . \quad (3.15)$$

With $D = \sqrt{\omega_{\text{res}}/m}$ this leads to a resonance frequency of

$$\omega_{\text{res}} = \frac{\omega_p}{2\sqrt{2}} \frac{1}{AR} \quad (3.16)$$

, which is dependent on the plasma frequency ω_p of the metal (compare to eq. (3.3)) and the inverse aspect ratio of the rod. Making a rod thinner thus leads to higher aspect ratio and the resonance shifts thus to lower frequencies/longer wavelengths.

Figure 3.5(b) shows simulated resonances of five cylindrical rods with an aspect ratio of $AR = 8.25$ and increasing rod length of 40 – 60 nm in steps of 5 nm. The resonance position in both scattering and absorption cross section is nearly constant at $\lambda = 720$ nm. The small deviations of about 10 nm can originate from meshing inaccuracies (compare to section 4.1) as well as from the charge accumulation at the rod ends not being point-like as assumed in the spring-mass model.

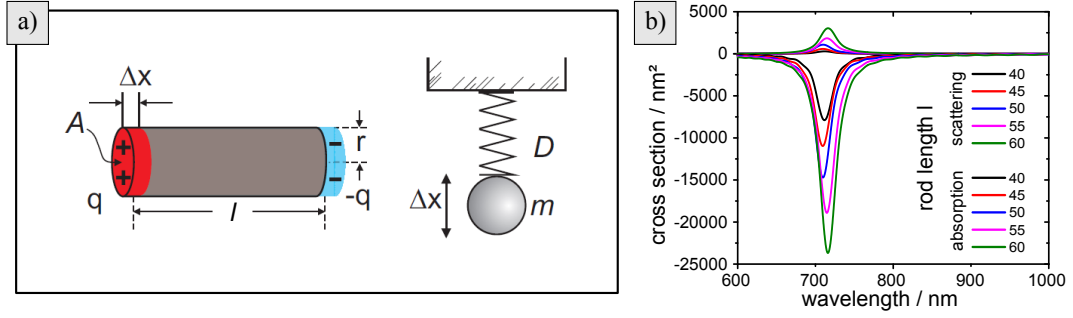


Figure 3.5: Plasmonic resonances of elongated metal particles. a) Sketch of the spring-mass model used to explain the resonance shifts dependence on the rod dimensions $A = r^2\pi$ (basis area) and length l . Δx denotes the distance the metal electron gas is displaced when an external field is applied, allowing to calculate the excess charge q at the rod end. The right part shows the mechanical analogon with a mass m fixed with a spring with a spring constant D (from [71]). b) Cross sections of a single rods with a constant aspect ratio of $AR = 8.25$ and lengths from $l = 40$ nm to 60 nm in steps of 5 nm.

3.2.2 Quasistatic approximation

For very small particles with dimensions much smaller than the excitation wavelength $d \ll \lambda_{\text{exc}}$ retardation effects won't occur since all electrons within the particle experience a constant phase. This is called the quasi-static limit and a particles cross sections are directly linked to its polarizability α . It is defined as the relation between a particles dipole moment \mathbf{p} to an impinging electromagnetic field \mathbf{E} in a dielectric environment ε :

$$\mathbf{p} = \alpha \varepsilon \mathbf{E} \quad . \quad (3.17)$$

The polarizability of a spherical nanoparticle with radius R , the external field k-vektor k and $R \cdot k \ll 1$ is given as [72]:

$$\alpha = 4\pi R^3 \varepsilon_0 \frac{\varepsilon_m - \varepsilon_d}{\varepsilon_m + 2\varepsilon_d} \quad . \quad (3.18)$$

ε_0 , ε_d and ε_m are the dielectric constant of vacuum, the surrounding dielectric medium and the metal respectively. Larger spheres will lead to an increased polarizability, since more oscillating charges will be separated by a larger distance. Additionally there is a resonance condition, if the denominator in eq. (3.18) becomes minimal (Fröhlich condition), which is not dependent on the particle size but only on the dielectric constants of the particle material

and the embedding medium. The cross sections depend on the polarizability as [72]:

$$\sigma_{\text{sc}} = \frac{k^4}{6\pi\epsilon_0^2} |\alpha(\omega)|^2 \quad (3.19)$$

$$\sigma_{\text{abs}} = \frac{k}{\epsilon_0} \text{Im}(\alpha(\omega)) \quad . \quad (3.20)$$

Scattering is therefore dependent on R^6 and dominates for large particles, while absorption goes with R^3 and dominates for smaller particles. The large polarizability of metallic nanoparticles at resonance can lead to cross sections of about one order of magnitude larger than their geometric cross section. Together with the sensitivity of their resonance to the dielectric constant of the environment, small spheres are often used as sensors in liquid environments [73].

For a ellipsoidal particle with three different half-axis a, b, c and the excitation fields polarized along the x -axis the polarizability is given as:

$$\alpha_x = 4\pi abc \frac{\epsilon_m - \epsilon_v}{3\epsilon_m + 3L_x(\epsilon_m - \epsilon_v)} \quad . \quad (3.21)$$

Since $L_x = 2a$, the length of the particle affects the denominator and the resonance wavelength of the particle can be tuned by the particle geometry (see also Fig. 3.4).

Bigger particles will show not only a dipolar mode, but also higher order modes and cannot be treated within the quasi-static approximation anymore. Then, a fully time-dependent solution is needed.

3.2.3 Far-field radiation patterns

In Fig. 3.6 the radiation patterns of the four lowest energy plasmonic particle resonances for elongated rods with a rectangular cross section of 25×25 nm illuminated with monochromatic light of $\lambda = 911$ nm are compared with their corresponding 1D rf-antenna counterpart [71]. The fundamental dipolar resonance of the rod is denoted with the amount of current maxima $n = 1$ and shows only minor deviations, only the directivity of the plasmonic antenna is reduced slightly. This originates from the rod length $l \approx \lambda_{\text{SPP}}/2$ being shorter than half the free space wavelength, leading to a radiation pattern more similar to a point dipole as shown in Fig. 2.7(b).

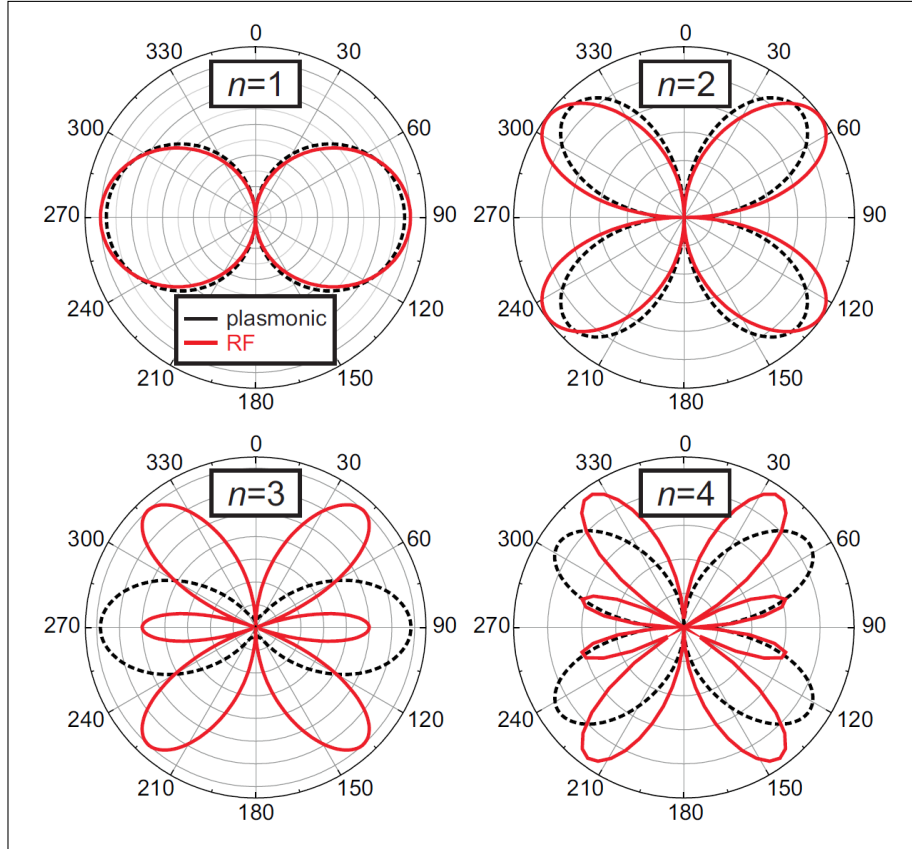


Figure 3.6: Comparison of antenna far-field radiation patterns for different resonance length $l = n \cdot \lambda_{\text{SPP}}/2$. Red lines show the rf case, black lines the case for optical antennas [71].

The second order resonance $n = 2$ is not much different from the rf-antenna case, too. This emission pattern is absent in Fig. 2.7, due to the symmetric feeding condition. In general all even numbered modes are difficult to excite from the far-field with illumination perpendicular to the wire due to reciprocity reasons, as they have vanishing emission power at angles of 90° and 270° .

The plasmonic $n = 3$ resonance still shows a dipolar emission pattern, now with large directivity, as its length has not yet surpassed the critical length of 1.2λ (see section 2.4). For the rf-antenna radiation pattern for $n = 3$ additional radiation lobes emerge. Similar arguments explain the plasmonic rod resonance with $n = 4$ still behaving qualitatively like a $n = 2$ antenna, where its rf-counterpart already emits into twice as many radiation lobes.

This difference in the far-field radiation pattern has to be taken into account for far-field excitation of plasmonic antennas, again with reciprocity as

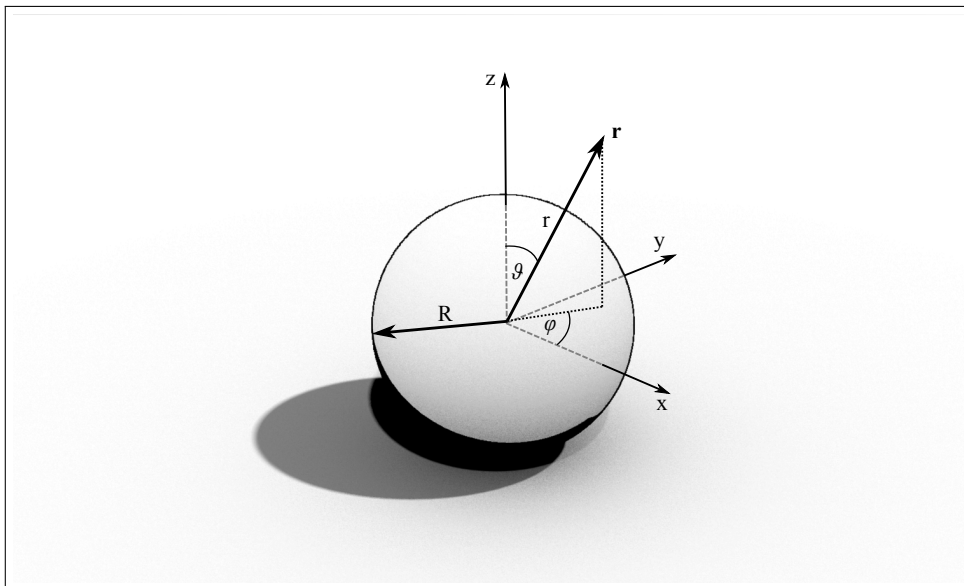


Figure 3.7: A sphere with radius R is centered at the origin of a spherical coordinate system described by coordinates r, ϑ, φ (substrate for artistic purposes only).

argument (see section 2.4.3) and a far-field radiation pattern maximum also represents a direction of optimal far-field excitation.

3.2.4 Mie scattering

For systems with spherical symmetry obeying Maxwell's equations all electromagnetic fields can be decomposed into an infinite series of orthogonal spherical vector wave functions. This is the basis of the analytical calculations published by Gustav Mie in 1908 [69], explaining the colorful scattering behavior of gold nanoparticles suspended in water, as observed by Michael Faraday nearly 60 years in advance [68]. The reduced system of a single spherical particle illuminated by a plane wave is sufficient. Here only the fundamentals are presented, which are needed to understand the later discussion of an emitting dipole positioned close to a metallic sphere. The complete mathematical derivation and deeper physical discussion of the topic can be found in [72, 74].

The geometry considered is depicted in Fig. 3.7: a sphere with radius R made from an arbitrary material is situated in the center of a spherical coordinate system with $\mathbf{r} = (r, \vartheta, \varphi)$ the plane wave impinges from positive x -direction. The indices $1/2$ denote the volume inside and outside the sphere

respectively. To solve the wave equations (2.6) and (2.7) they can be rewritten:

$$\nabla^2 \mathbf{E} + k^2 \mathbf{E} = 0 \quad (3.22)$$

$$\nabla^2 \mathbf{H} + k^2 \mathbf{H} = 0 \quad (3.23)$$

, with the wave vector $k^2 = \omega^2 \varepsilon \mu$, where $\varepsilon_{1/2} = \varepsilon_{r,1/2} \varepsilon_0$ describes the materials and $\mu = \mu_0$, as the material is non magnetic with $\mu_r = 1$. The surface of the sphere defines the following boundary conditions at $\mathbf{R} = (R, \vartheta, \varphi)$:

$$[\mathbf{E}_2(\mathbf{R}) - \mathbf{E}_1(\mathbf{R})] \cdot \hat{\mathbf{n}} = 0 \quad (3.24)$$

$$[\mathbf{H}_2(\mathbf{R}) - \mathbf{H}_1(\mathbf{R})] \cdot \hat{\mathbf{n}} = 0 \quad (3.25)$$

The solution for equs. (3.22)–(3.25) is a set of eigenfunctions called spherical vector wave functions. Their derivation is explained in detail in [72], chapter 4, here only the resulting terms will be presented, which are separable in all three coordinates:

$$\mathbf{M}_{\sigma,m,n}^{(1)}(k\mathbf{r}) = \nabla \times [\mathbf{r} y_{\sigma,m,n}(\vartheta, \varphi) j_n(kr)] \quad (3.26)$$

$$\mathbf{N}_{\sigma,m,n}^{(1)}(k\mathbf{r}) = \frac{\nabla \times \mathbf{M}_{\sigma,m,n}^{(1)}(k\mathbf{r})}{k} \quad (3.27)$$

Several further explanations are necessary:

- $\mathbf{M}^{(1)}$ and $\mathbf{N}^{(1)}$ are the eigenfunctions inside the sphere which do not diverge for $r = 0$. Outside the sphere different functions $\mathbf{M}^{(3)}$ and $\mathbf{N}^{(3)}$ facilitate further calculations. The spherical Bessel function of the first kind j_n is replaced by the spherical Hankel function (spherical Bessel function of the third kind) h_n^1 . They are given as

$$j_n(r) = \sqrt{\frac{\pi}{2r}} J_{n+1/2}(r) \quad (3.28)$$

and

$$h_n^1(r) = j_n(r) + i \sqrt{\frac{\pi}{2r}} Y_{n+1/2}(r) \quad (3.29)$$

respectively, with J and Y denoting the Bessel-functions of first and second kind.

- The index σ can take the values e (even) or o (odd). This defines the form of $y_{\sigma,m,n}$:

$$y_{e,m,n}(\vartheta, \varphi) = \cos(m) P_n^m(\cos \vartheta) \quad (3.30)$$

$$y_{o,m,n}(\vartheta, \varphi) = \sin(m) P_n^m(\cos \vartheta) \quad . \quad (3.31)$$

The P_n^m denote the associated Legendre polynomials.

- Due to the dependency on $k \cdot \mathbf{r}$ the spherical vector wave functions scale automatically with wavelength and material.

The spherical vector wave functions build the basis of a Hilbert-space. Therefore, any electric field solving (3.22) can be expressed by an infinite series of the eigenfunctions:

$$\mathbf{E} = \sum_{\nu} (\xi_{\nu} \mathbf{N}_{\nu} + \zeta_{\nu} \mathbf{M}_{\nu}) \quad (3.32)$$

, with the abbreviation $\sum_{\nu} = \sum_{\sigma} \sum_m \sum_n$. The expansion coefficients ξ_{ν}, ζ_{ν} are well-defined as the spherical vector wave functions are orthogonal:

$$\int_V M_{\nu} \cdot M_{\nu'} dV = 0, \quad \int_V M_{\nu} \cdot N_{\nu''} dV = 0, \quad \int_V N_{\nu} \cdot N_{\nu'} dV = 0 \quad (3.33)$$

for arbitrary ν, ν'' and $\nu' \neq \nu$.

Gustav Mie determined in his work analytical representation of six distinct 'Mie'-coefficients ξ_{ν}, ζ_{ν} by setting up a linear system of equations fulfilling the boundary conditions eq. (3.24) and eq. (3.25): A_{ν}, B_{ν} for decomposing the incoming plane wave, a_{ν}, b_{ν} describing the scattered fields and c_{ν}, d_{ν} for the field inside the particle.

The lowest two electric type Mie modes $\mathbf{N}_{e11}^{(1)}$ and $\mathbf{N}_{e12}^{(1)}$ are depicted in Fig. 3.8, which are (a) the dipole mode and (b) the quadrupole mode. In the quasi-static limit only \mathbf{N}_{e11} can be excited from the far-field, since only this mode shows an overall dipolar moment. The near-fields intensities are localized to very small volumes directly at the particles surface and are several orders larger than the excitation far-field. This is one reason for the large interest in plasmonic resonances, as they allow circumventing the diffraction limit and are tunable by particle geometry and environment.

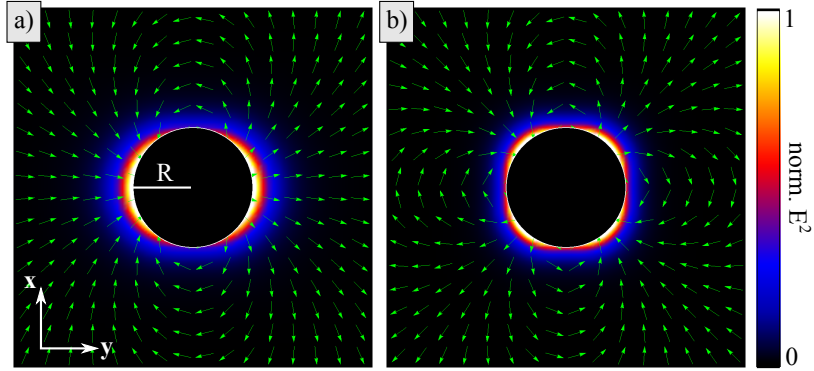


Figure 3.8: Field intensity (color) and direction (arrows) of the fundamental electrical Mie-modes in the cross section plane of a sphere with $R = 10$ nm at $\lambda = 500$ nm. (a) dipolar mode $\mathbf{N}_{e11}^{(1)}$. (b) quadrupolar mode $\mathbf{N}_{e12}^{(1)}$.

3.2.5 Split-ring resonators and kinetic inductance

A special kind of plasmonic resonator is realized by bending a metallic nanorod with a fundamental dipolar resonance such that it forms nearly a ring with the two rod ends pointing to each other, as sketched in Fig. 3.9(a). The left side shows the ideal geometry of such a *split-ring* with a spherical shape and a small slit, the right side shows a square shape [75] often used for very small split-rings in experiment, where fabrication limits realizable shapes.

Figures 3.9(b) and (c) show the electric and magnetic fields respectively, of the fundamental mode for a square split ring made from gold with a side length of 200 nm and a wire thickness and height of both 50 nm at a resonance wavelength of $\lambda \approx 1515$ nm. As for a straight rod large electrical near-fields emerge due to charges accumulating at the rod ends, which are more prominent in the gap due to capacitive coupling. The split-ring also produces pronounced magnetic field hot spots at the inner rod bends near the position of maximum current rotation $\nabla \times I$. These fields are pointing out of the ring plane and form a magnetic dipole moment.

This makes split-rings an ideal fundamental building block for metamaterials, where electric and magnetic resonators sized below half the wavelength of the impinging electromagnetic radiation make it possible to tailor the effective permittivity and the effective permeability of a material. This allows to create negative index materials [5] as well as cloaking devices [76], which both will not be described in greater detail.

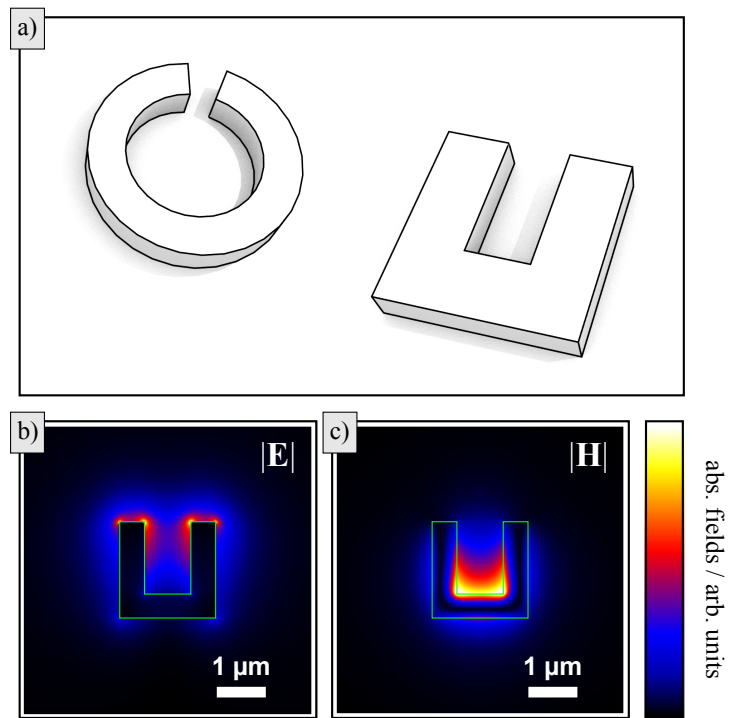


Figure 3.9: Properties of split-ring resonators. a) Typical geometries: Additional to the capacitance of the two open ends, an inductance is realized by currents with a non-zero rotation. b) Absolute values of the electric fields for a square split ring made from gold with a side length of 200 nm and a wire thickness and height of both 50 nm at a wavelength of $\lambda \approx 1515$ nm. c) Absolute values of the magnetic fields for the identical split-ring. The maximal values are at the inner side of the split-ring bends, where the rotation of the mode currents are maximal. The green strokes outline the split-ring geometry.

It has to be mentioned, that the ideal spherical split-ring designs has a very small extinction cross section, as the charges gather at a small gap leading to a very small overall dipolar moment that can couple to far-field radiation.

The resonance frequency of a split ring depends on its inductance, which is for large areas dominated by the well known geometric inductance L_g . However, it is not possible to decrease the split ring resonance wavelength infinitely, as for large frequencies the kinetic inductance L_k is not negligible any more. As the energy stored in the magnetic fields decreases with the split ring area, kinetic energy of the electrons becomes eventually comparable and the kinetic inductance becomes the lower inductance limit. For a split ring made from a wire with cross section A and length l , where the metal has an electron number density of n moving with velocity v comprising a current $I = A \cdot n \cdot e \cdot v$ the kinetic energy is given by:

$$E_{\text{kin}} = \frac{1}{2}mv^2 = \frac{1}{2}(m_e \cdot n \cdot A \cdot l) \left(\frac{I}{A \cdot n \cdot e} \right)^2 = \frac{1}{2} \overbrace{\left(\frac{m \cdot l}{A \cdot n \cdot e^2} \right)}^{L_k} \cdot I^2 \quad . \quad (3.34)$$

Therefore, the fundamental split ring resonance has a lower wavelength limit of 900 nm [24]. One way to shift magnetic resonances into the optical regime anyway, is to use rings with multiple cuts [24], a second one will be presented in chpt. 7.3.

3.3 Optical antennas

3.3.1 Definition and application

Radio-frequency antennas convert propagating electromagnetic waves into oscillating currents or vice versa. This functionality will be used to define the term *optical antenna* within this work: a device converting electromagnetic waves in the visible frequency range into free charge carrier oscillations with identical frequency. This definition excludes geometries purely made from dielectric materials which are elsewhere often termed as antennas, e.g. [77].

Any geometry made from metal can be termed optical antenna, as well as any brick of stone can be termed a hammer, too. For both applications optimized designs are available, but the word 'hammer' triggers a very distinct

picture of a device. The same might in the future be the case for the term 'optical antenna' after an optimal form has been developed and a certain social adaption process filled the term with meaning.

All optical antennas show three effects: scattering, localization and heat generation. Only the their fraction is variable and so optical antennas can be differentiated dependent on their application³. *Scattering optical antennas* re-emit received energy into the far-field and are used e.g. for bio-sensing [3] and solar cell enhancement [7]. *Heating optical antennas* are applied in e.g. cancer treatment [8], (waste) water treatment [9], or for assistance in magnetic recording [10]. Additionally the decay of plasmons into hot electrons can be used for generating photo-currents [78] or establishing chemical reactions [79].

Finally there are *focusing optical antennas*, applying plasmonic near-fields. Many of their possible applications are depicted in Fig. 3.11: optical trapping [80], electron emission [81], multi-photon physics [82, 83], lithography [84], solar cell enhancement [7], surface/tip enhanced Raman spectroscopy (SERS/TERS) [85, 86], magnetic reading and switching [87, 88], waveguide coupling [89, 90], scanning near-field microscopy (SNOM) [91], single photon sources [92], surface plasmon amplification by stimulated emission of radiation (SPASER) [93, 94].

Focusing optical antennas are experimentally exploited for over thirty years (for a historical review, read [14]). Research has reached a stadium, where the fundamental experiments with sharp tips and particles of simple geometries have been performed numerous times and many reviews are available [21, 71, 95–97]. Furthermore, a first book dedicated solely to optical antennas has been published [98].

3.3.2 The dipolar two-wire antenna

To understand some of the key concepts of focusing optical antennas we take a closer look at the linear dipolar two-wire nanoantenna. It consists of two identical metallic nanorods, the antenna arms, aligned along their long axis and separated by a small gap, forming a structure comparable to a classical linear antenna.

³The same is true for hammers.

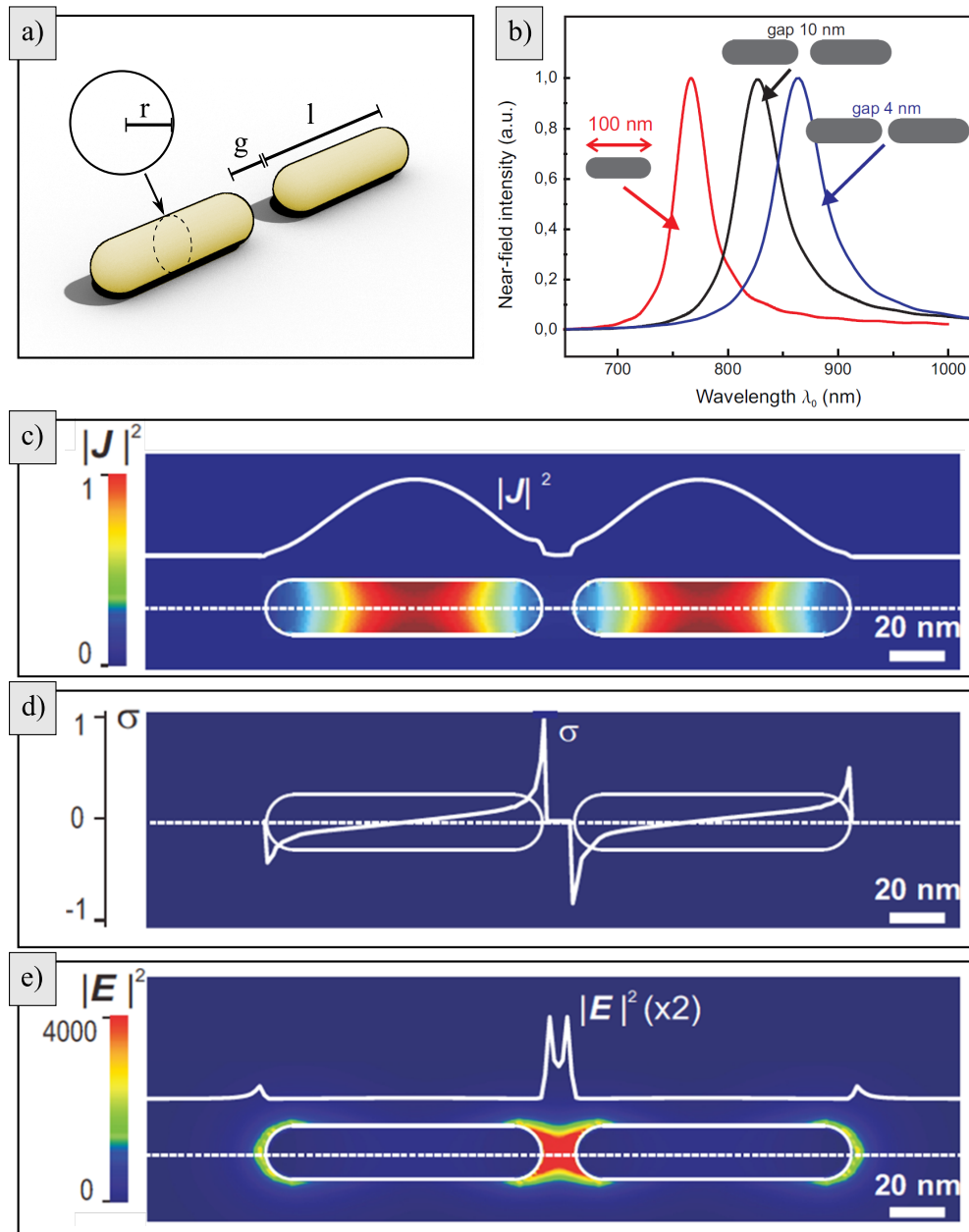


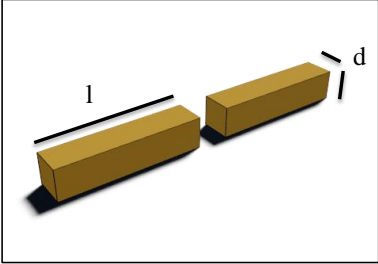
Figure 3.10: Properties of two wire dipolar optical antennas excited at resonance. a) Basic geometry consisting of two identical rods of length l with a circular cross-section of radius r and spherical end caps, separated by a narrow gap with width g . b) Normalized NFIE of a single rod with $l = 100$ nm and $r = 10$ nm, as well as of two-wire dipolar antennas made from identical rods separated by gaps of 10 and 4 nm. c) induced currents, d) charge density per length and e) NFIE at the resonance frequency of $\lambda = 830$ nm for the antenna with $g = 10$ nm [99].

Here, the rods are cylindrical with an overall length $l = 100$ nm, a cross section radius $r = 10$ nm and spherical end caps as sketched in Fig. 3.10(a). Figure 3.10(b) shows the wavelength dependent near-field intensity enhancement (NFIE) spectra close to the end caps of a single rod as well as of two dipolar antennas with gaps of $g = 10$ nm and $g = 4$ nm when illuminated from the far-field with a broadband Gaussian focus of $\text{NA} = 1$. All spectra show a Lorentzian-shaped resonance peak, the resonance wavelength being shortest for the single rod and getting longer for the coupled rods, as their gap width decreases.

Figures 3.10 (c) – (e) show current density, linear charge density⁴ and NFIE respectively for the antenna with $g = 10$ nm at its resonance frequency of $\lambda = 830$ nm. The current density of the dipolar optical antenna resembles to a voltage-fed λ -antenna leaving each arm overall uncharged (see Fig. 2.6). However, more charges accumulate at the gap due to capacitive coupling, shifting also the current maximum to the gap. This effect generally occurs at rod distances of $g \approx 50$ nm and smaller, giving rise to a very pronounced NFIE in the gap volume. Figure 3.10(e) reveals an NFIE of more than 4000-fold compared to the maximum field intensity in the focal spot of the illuminating Gaussian focus without antenna. As the gap volume is about $10 \times 20 \times 20$ nm³, the optical antenna realizes a much higher field confinement than achievable with far-field optics restricted by diffraction (see section 2.2). The observed resonance shift to lower energies for coupled rods with decreasing gap size originates in the reduction of the restoring force, as the complementary charges gathering at the gap are shielding each other (compare to the spring-mass-model in section 3.2.1).

Plasmon resonances of interacting particles follow a hybridization law [100], resulting in two coupled resonances for two dipolar particle resonances, one termed 'symmetric' and one one termed 'anti-symmetric', depending on the fields of the coupled system. Here, we focus on the anti-symmetric resonance for the dipolar antenna, which is shifted to lower energies compared to the single rod resonance. The symmetric resonance (i) is difficult to excite efficiently from the far-field due to a vanishing macroscopic dipolar moment and (ii) shows no near-field enhancement in the center gap, which could later be

⁴Simulations and data analysis performed by the author.



d / nm	30	25	20	15	10
l / nm	90	84	74	61	46
λ_r / nm	725	729	729	726	729
$\Delta\lambda / \text{nm}$	58	46	36	29	26
Q-factor	12.5	15.8	20.3	25.0	28
E_{max}	~2200	~3100	~4100	~4600	~3600

Table 3.1: Q-factor, resonance width $\Delta\lambda$, and maximum near-field intensity enhancement E_{max} of optical antennas consisting of gold wires with length l separated by a 10 nm gap with constant resonance wavelength λ_r but decreasing square cross section d^2 (originating from supplementary material to [102]).

used to couple efficiently to single emitters [101].

For optical antennas, their thickness d often is only 1 – 2 orders of magnitude smaller than the antenna length l , contrary to the rf-antenna case with quasi 1D-wires. This has two reasons: (i) fabrication of wires thinner than 10 nm is extremely demanding, and (ii) scaling of effective plasmon wavelength. Wires with smaller d lead to shorter rod lengths l resonant at the given frequency (compare with single rods in section 3.2.1). Therefore, the antennas overall polarizability decreases as does the extinction cross section, impairing the coupling to far-field radiation. This results in an increased quality factor Q of the antenna resonance (See section 2.3), as Table 3.1 shows for a series of antennas made from cuboids with decreasing square cross section of edge length d , tuned in overall length for constant resonance wavelength λ_r . In the beginning thinner antennas show, however, higher maximum NFIE, due to better field confinement in the gap originating in the smaller geometrical cross section of the rods. For even thinner rods eventually the NFIE decreases again, due to the aforementioned reduction of polarizability as direct result of the shortening of the effective wave length λ_{SPP} (compare with eq. (2.42)). This shows once again, that an optical antenna has to fulfill two tasks, coupling to far-fields and focusing the received energy, which cannot be optimized independently within structures showing a single mode.

Applications of resonant focusing optical antennas




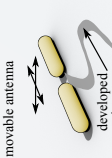
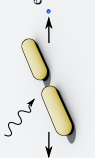
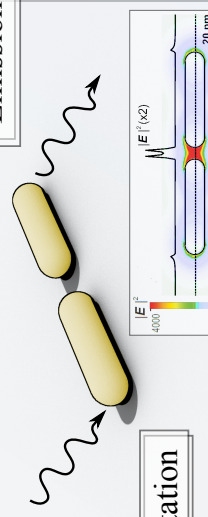
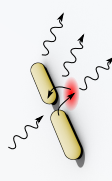
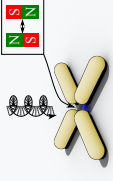
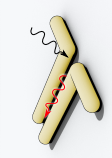
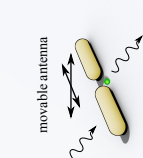
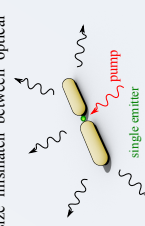
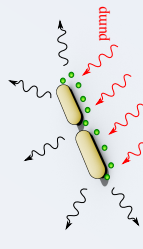
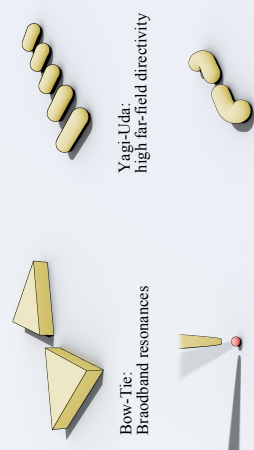
<p>An antenna converts electromagnetic far-field radiation into currents or vice versa. In the optical regime metals show a different behavior compared to radio frequencies and plasmons can be excited, coupled states between fields and currents. Here applications of resonant focusing optical antennas, which can generate a highly localized and enhanced volume of near-fields below the diffraction limit, are presented.</p>	<p>Optical Trapping: The forces exerted by strong electro-magnetic fields are used to trap particles. Can be coupled with sensing.</p> 	<p>Electron emission: Strong localised fields give rise to an enhanced photo effect or even to tunnel electrons. Can be used e.g. as pulsed electron source.</p> 	<p>Multi-photon physics: The high photon density in the near field hot spot enhances second harmonic generation (SHG) and two-photon luminescence (TPL)</p> 	<p>Lithography: A moving antenna can be used to write structures into a resist below the refraction limit.</p> 	<p>Solar cell enhancement: The resonance of the antenna increases the interaction time between light and material. The strong focusing allows to work with reduced material, e.g. quantum dots. The antennas can serve as metallic contacts.</p> 
<p>This is the classical geometry of an optical antenna: two metallic rods are separated by a small gap, the near-fields are enhanced in due to capacitive coupling.</p>	<p>Excitation</p> 	<p>SERS: Surface Enhanced Raman Spectroscopy is enhanced twice in excitation and emission by optical antennas. This can lead to enhancement factors up to 10^{14}.</p> 	<p>Magnetic reading and switching: Circular polarised excitation can switch magnetical materials in the hot spot volume. Can be used for optical data storage and retrieval.</p> 	<p>Waveguide coupling: The field in the center resembles that of a guided mode of a plasmonic transmission line. Optimizes energy transfer from far-field to plasmonic circuitry.</p> 	<p>SNOM: Scanning Near-field Optical Microscopy uses optical antennas for imaging. The strong localization of near-fields can circumvent the diffraction limit and thus increase resolution. The antenna has to be scanned across the sample. Can be combined with SERS.</p> 
<p>Single Photon Source: The emission rate of point like photon emitters like dye molecules or quantum dots is low due to the size mismatch between optical wavelength and emitter. Optical antennas can circumvent these limitations as their size is comparable to the wavelength, but the hot spot allows strong coupling to the emitter.</p> 	<p>SPASER: Surface Plasmon Amplification by Stimulated Emission of Radiation. A gain medium is pumped by an external light source. The power is transferred coherently by stimulated emission into the plasmon mode of the antenna which further radiates into the far-field. Allows laser smaller than $\lambda/2$ as the resonant antennas are, too.</p> 	<p>Geometrical Variations</p>  <p>Bow-Tie: Broadband resonances</p> <p>Yagi-Uda: high far-field directivity</p> <p>chiral geometries: sensitive to circular polarizations</p> <p>Single Tip: Easy to fabricate & scan sensitive to z-components</p>			

Figure 3.11: Overview of the possible applications of optical antennas using near-fields of excited plasmonic resonances.

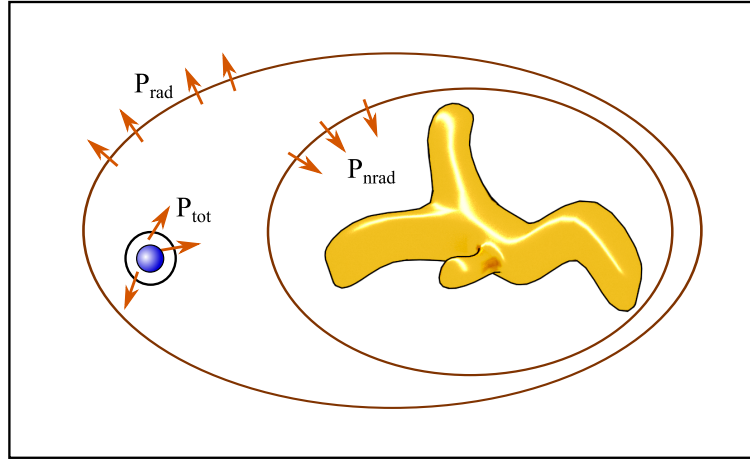


Figure 3.12: The total power output P_{tot} of an excited quantum emitter (blue) near a metal nanoparticle is split into two parts: the radiative emission rate P_{rad} , measurable in the far-field, and the non-radiative emission rate P_{nrad} which is transformed into heat. The sketched volumes can be used to calculate the powers by integrating the Poynting vector flux through their surfaces.

3.3.3 Quantum emitter emission enhancement

An excited quantum emitter (QE) placed in close distance to a metallic nanoparticle can have a strongly enhanced decay rate according to eq. (2.26), if it excites a (resonant) plasmon mode with high intensity near-fields at its position. This effect has been a research topic in theory and experiment for more than forty years since it has been identified as the main working principle of surface-enhanced Raman scattering (SERS), which has been discovered 1974 [103]. In most of the cases the Raman shift, which is the wavelength change between excitation and emission, is much smaller than the width of the plasmonic resonance. Since reciprocity applies to optical antennas (see section 2.4.3), both excitation and emission are enhanced in the presence of plasmonic resonances. The resulting SERS signal enhancements of up to $\text{NFIE}^2 \approx 10^{10}$ [104] increasing the signal to noise ratio by a large margin, enabling measurements of small analyte amounts. It has been shown on rough metal films that surface enhanced Raman scattering (SERS) can reach single molecule sensitivity [105], and tip enhanced Raman spectroscopy (TERS) has already been used to map molecular sub-structures [18].

Not all the power transferred from the QE to the nanoparticle will reach the

far-field, since plasmonic excitations show Ohmic losses at optical frequencies. Therefore, the total emission power P_{tot} of the QE is split into a radiative part P_{rad} detectable in the far-field and a non radiative part P_{nrad} , heating the nanoparticle (comparable to cross sections, see section 3.2.1). Figure 3.12 sketches exemplary surfaces for calculating the different powers analytically and numerically via the Poynting vector in eq. (2.5). The quantum efficiency η of a SE-antenna system is then defined as

$$\eta = \frac{P_{\text{rad}}}{P_{\text{tot}}} = \frac{P_{\text{rad}}}{P_{\text{rad}} + P_{\text{nrad}}} \quad (3.35)$$

, where the internal efficiency of the QE is always $\eta_{\text{int}} = 1$.

An analytical solution exists for the case of a SE near a spherical metal particle [106], which will therefore be used as benchmark system to evaluate the quality of numerical results (see chpt. 4) and of novel theoretical approaches (see chpt. 9). In Fig. 3.13 the left column shows the behavior of an excited dipole with a dipolar moment perpendicular to the surface of a sphere made from gold with radius $R = 10$ nm. The top graph row shows always enhanced radiative power with a maximum at the resonance wavelength of the sphere at $\lambda_r \approx 535$ nm. This effect gets more pronounced for decreasing distance, in agreement with eq. (2.26) because the mode fields of the dipolar sphere mode (see Fig. 3.8) get stronger close to the surface. However, the center graph shows the non-radiative power increasing even faster, as the coupling into more and more higher order non-radiative sphere modes sets in. This is also visible in the lower left panel, where the quantum efficiency (green dashed line) drops significantly for distances lower than 25 nm.

For the dipolar moment parallel to the sphere surface, shown in the right column of Fig. 3.13, no radiative power enhancement can be realized. The radiative dipolar mode of the sphere is excited with the wrong phase (compare with eq. (2.27)). Additionally the quadrupolar and higher order non-radiative modes are still well excitable, leading to quenching. The total power P_{tot} of the QE is increasing at distances of about 20 nm and smaller, however, the quantum efficiency is dropping fast.

The emission powers for QEs near arbitrary shaped optical antennas can only be retrieved by numerical methods, making it difficult to design antenna geometries for e.g. optimal P_{rad} . However, there are two closely related fields

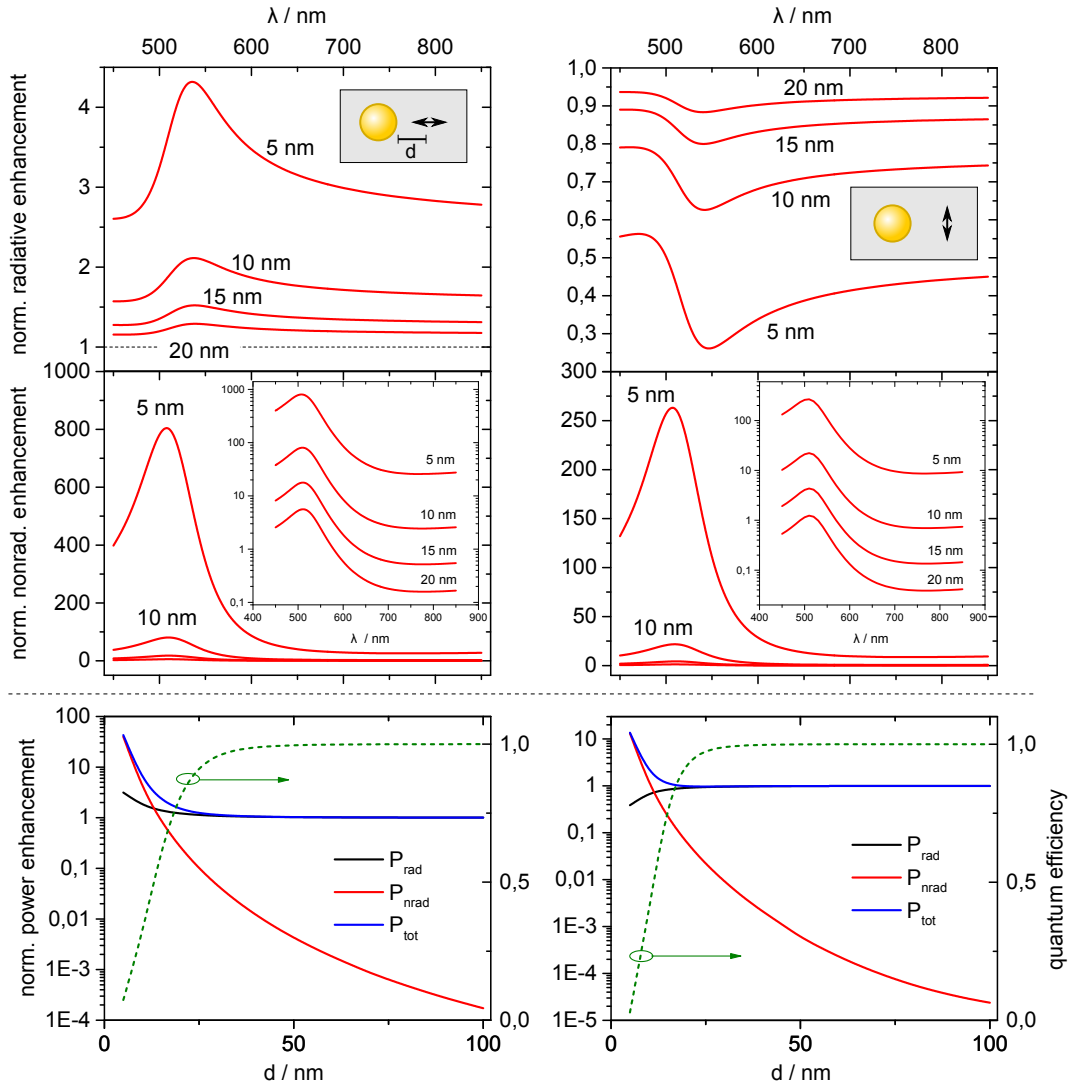


Figure 3.13: Analytically calculated emission rates of an excited dipole in front of a gold sphere with radius 10 nm. Left column: dipole moment perpendicular to sphere surface; right column: dipole moment parallel to sphere surface. Upper row: radiative emission enhancement spectra for different distances between sphere and dipole; center row: non-radiative emission enhancement spectra; bottom row: distance dependent power enhancements P_{rad} , $P_{\text{nrاد}}$ and P_{tot} as well as the quantum efficiency (green dashed line; axis right) for a wavelength of $\lambda = 650$ nm (calculations performed using Mathematica 9).

of physics – rf-antenna technology (see section 2.4) and cavity physics (see section 2.3.2) – which are often referred to as source for intuitive physical understanding and antenna design guidelines. Both approaches establish new figures of merit and have led to working plasmonic devices, yet, they delivered only a few rules-of-thumb for their functionality assessment. They will be highlighted in the next paragraphs together with the fundamental differences and resulting drawbacks.

Comparison to rf-antenna concepts There are many similarities between antennas for different wavelength regimes as all are converting electromagnetic radiation into alternating currents of the same frequency. However, major differences can be identified comparing rf-antennas (recall chpt. 2.4) with antennas for optical wavelengths:

The *driving mechanism* of optical antennas is different. Rf-antennas are mostly connected to a waveguide, which allows to add and remove charges from single antenna arms which is called current-feeding. Focusing optical antennas are driven by quantum emitters via their field, which is identical to voltage feeding. This leads to the fact, that two wire optical antennas cannot show a $\lambda/2$ -resonance, when driven by a quantum emitter. Even the recently published electrically connected antennas [107–109] are designed such that the leads are not hampering the antenna mode, but to apply constant voltages.

The *material* of rf-antennas can be described as an ideal metal without losses. Optical antennas on the other hand always have Ohmic loss channels, generating heat. This can limit their efficiency drastically, prohibiting high- Q plasmonic structures.

Finally the non-negligible *electron mass* leads to shorter effective wavelengths λ_{eff} for plasmonic waves on metallic structures (see section 3.2). This allows on the one hand to build resonators much smaller than half the resonance wavelength, but also e.g. decreases the coupling efficiency to the far-field for metallic nanorods due to a smaller polarizability. Emission patterns of linear antennas also differ [23] (recall Fig. 3.6). In addition the *penetration depth* of electromagnetic waves in the visible range is in the same order of magnitude as the thickness of an optical antenna. This leads to volume currents contrary to the surface currents in rf-antennas.

It has been tried to adapt the impedance matching concept to optical antennas (compare to section 2.4). For antennas with a clean and defined gap, the change of the antenna resonance by loading the gap with different materials can indeed be described by an equivalent circuit and, thus, also by impedance [110, 111]. This approach delivers a set of lumped circuit rules comparable to rf-technology, yet, the equivalent circuit for general plasmonic geometries has to be made up anew for each small change in the shape or setup of the components [112, 113]. The impedance of an antenna coupling into a plasmonic waveguide can also be determined, when their connection geometry is kept constant [114].

A second approach using impedance has been developed by Greffet [115]. He was able to identify terms comparable to the circuit power transfer function when rewriting eq. (2.30). Yet, the prior knowledge of the Green's function, which is only rarely possible analytically, cannot be circumvented.

Comparison to cavity physics The concept of the Purcell factor $F_P \propto Q/V$ (see section 2.3.2) seems promising for the description of spontaneous emission enhancement via plasmonic resonators, too. Focusing optical antennas obviously achieve high Purcell factors due to the small dimensions of their near-field hot-spots. Therefore, their mode volume V is smaller than their free space resonance wavelength, which cannot be achieved with resonators based on dielectric materials [116]. However, as already discussed the Q-factor is comparably small, with maximal values in the order of 10^1 due to high radiation losses for larger optical antennas and increasing Ohmic losses for smaller ones.

Additionally, it is not straight forward to calculate F_P from scratch for resonators with losses. First the complex resonance frequency $\tilde{\omega}_\nu = \omega_\nu - i\gamma_\nu$ has to be introduced, with $\gamma_\nu = 1/\tau_\nu$ being the damping factor of the mode which is inversely proportional to the mode lifetime τ_ν . Then, the quality factor can be redefined as $\tilde{Q} = -\text{Re}(\tilde{\omega}_\nu)/[2 \cdot \text{Im}(\tilde{\omega}_\nu)]$. The resulting, so-called quasi-normal modes (QNM) have fields $\tilde{\mathbf{E}}_\nu, \tilde{\mathbf{H}}_\nu$ leading to the mode volume integral (2.33) not to converge, as the free space radiation part of QNMs is diverging for $|\mathbf{r}| \rightarrow \infty$. Also the introduction of a cutoff criteria to subtract the far-field part of the QNM does not help [117].

Recently, this problem has been solved by two groups [118, 119], using the concept of perfectly matched layers (PML; see also section 4.1.2) to truncate the diverging fields of QNMs without changing the underlying physics, identifying this procedure as a coordinate transformation. Thus, it allows to calculate the mode volume as usual via integration of mode fields omitting divergence.

The resulting complex valued mode volume unfortunately is less intuitive and needs knowledge about the mode field distribution by rigorous Green's function calculation or numerical simulations:

$$\tilde{V} = \frac{\int \left[\tilde{\mathbf{E}}_\nu \cdot \frac{\partial(\omega\varepsilon)}{\partial\omega} \tilde{\mathbf{E}}_\nu - \tilde{\mathbf{H}}_\nu \cdot \frac{\partial(\omega\mu)}{\partial\omega} \tilde{\mathbf{H}}_\nu \right] d^3\mathbf{r}}{2\varepsilon_0 n^2 \left[\tilde{\mathbf{E}}_\nu(\mathbf{r}_0) \cdot \hat{\mathbf{p}} \right]^2} . \quad (3.36)$$

The denominator already includes the dependency on the field intensity parallel to the dipole moment, while the numerator takes into account dispersion effects. As a direct consequence, the known Purcell formalism is applicable with only minor changes:

$$F_P = \frac{3}{4\pi^2} \left(\frac{\lambda_0}{n} \right)^3 \operatorname{Re} \left(\frac{\tilde{Q}}{\tilde{V}} \right) . \quad (3.37)$$

Finally, it has been shown recently, that both formalisms – antenna impedance and cavity Purcell factor – are identical, when they are derived from the Green's function of the system [120]. However, the expected simplifications, like lumped circuit rules or intuitive mode volume design guidelines, are not realized yet, and the tedious task of solving the Green's function is still not circumvented.

Collection of design rules for optimized QE-antenna coupling Despite the difficulties in the theoretical description of optical antennas, some intuitive optimization rules have been framed in the literature, based on fundamental principles of electromagnetism⁵:

Lightning rod effect. As currents flow into a tip, the charge density is increased, leading to more pronounced near-field hot spots in their vicinity.

Capacitive coupling. Opposite charges separated by a small, insurmountable distance e.g. a gap attract each other increasing their density. This kind of

⁵Where not specified, all reviews mentioned on page 44 incorporate the rule.

coupling together with the aforementioned lightning rod effect is today the most used way to achieve the smallest volume highest field plasmonic hot spots. Prominent examples using the first two effects are bow-tie antennas and TERS, with an additional metallic substrate.

Resonance tuning. This might sound trivial in the first place, but e.g. the bow-tie antenna has a broad-band resonance, which is for focusing at a given wavelength not as effective as an optimized single resonance dipolar antenna. Furthermore, the shape of the particle(s) has a strong effect on the resonance, especially the existence of tips and narrow gaps can lead to large resonance shifts.

Yet, there is an additional way to tune the resonance, not in frequency, but in wavelength by changing the dielectric function of the direct antenna environment. Filling material in the gap of an antenna – sometimes referred to as loading – has been mentioned above, but also putting the antenna on a substrate (sometimes with an intermediate adhesion layer) shifts its effective plasmon wavelength [121] and thus its resonance to longer wavelengths. Often this is undesired, as it decreases the particles polarizability.

The inverse case, putting the QE inside a high index material half space near the surface and the plasmonic antenna near the surface in the vacuum, is a effective measure to enhance the QE to antenna coupling [122], as it decreases the size mismatch between emission wavelength and QE.

Optimize far-field coupling. This is not a real optimization for the coupling between an antenna and a QE. Yet, this second step of the optical antenna functionality has also a major impact on the amount of photons reaching the far-field in the end. Else, an QE placed on the surface of a metal sphere can heat it very efficiently.

There are two main different strategies: (i) Maximize the overall polarizability of the antenna structure. This increases the overall coupling to the far-field [122]. (ii) Work with/in a high index medium. This reduces the mismatch between far-field radiation and structure dimensions (adapted from [122]).

A third strategy is tailoring the directivity of the antenna by its environment, which shall be mentioned only briefly. As in most applications the far-field is accessed via a microscope objective, a large fraction of an optical antennas dipolar emission is lost. In [77] an environment is introduced, which

redirects radiation from an QE into the collection angle of a high-NA objective. This should also work for optical antennas.

There are even more ways to optimize plasmonic focusing, which will be left aside in this work, as they leave the picture of optically small single particles, looking on wave-guides or particle ensembles (e.g. Yagi-Uda designs).

Part II

Methods

Chapter 4

Numerics

Analytical solutions for Maxwell's equations can be derived only for a few simple geometries. To plan and understand experiments with more complex geometries, numerical methods are the only viable tool and, thus, many different algorithms are available today to solve electrodynamic problems. In this work the finite-difference time-domain (FDTD) method has been used most of the time, as it allows the analysis of transient signals with broadband spectra in a single simulation and in an intuitive way. In addition quasistatic simulations with rotational symmetry were performed with the finite element method (FEM) for fast assessment of novel geometries.

This chapter explains the FDTD algorithm to an extent necessary for the understanding of later results. For a primal read the extensive groundwork book from Taflove [123] is recommended. All FDTD simulations within this work were performed with the commercial software *FDTD-Solutions* from the company *Lumerical Solutions Inc., Canada* in versions 5 to 8.7.1.

The FEM method will be introduced only very briefly, as the relevant geometries were all re-evaluated with FDTD simulations. The software used was COMSOL Multiphysics in versions 4.4. and 5.0.

Finally, this chapter introduces evolutionary algorithms, as this method to find solutions to complex non-analytical problems was applied in this work to optimize focusing optical antennas.

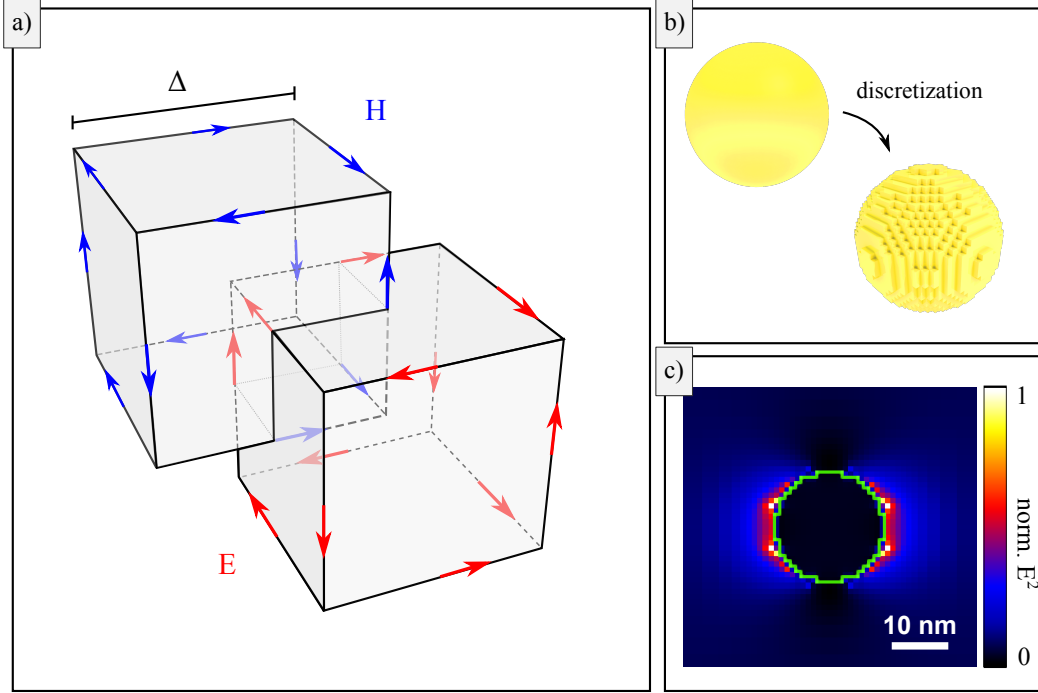


Figure 4.1: a) The Yee-cell as space discretization used in the FDTD algorithm for solving Maxwell's equations. The electrical fields E (red) sit on the edge-centers of a cubic lattice (only one cube is shown). A second lattice is shifted by half the cube size Δ in all three dimensions and carries the magnetic fields H (blue). b) Geometric consequence of the staircasing effect for cubic space discretization of a sphere. c) Resulting near-field intensities for a sphere with radius of 10 nm discretized by 1nm Yee-cells. The green line sketches the sphere surface.

4.1 The finite-difference time-domain algorithm

The FDTD algorithm discretizes space and time by means of the Yee-cell [124] in order to approximate the derivatives in Maxwell's equations (2.1c) and (2.1d) as differential quotients and, thus, describes the evolution of electric and magnetic fields in space and time. The special geometry of the Yee-cell (see Fig. 4.1(a)) allows to compute the curl of fields along all three dimensions.

Two cubic lattices with lattice constant Δ are used to segment space with the second lattice shifted by $\Delta/2$ in all three dimensions. One lattice is used to represent the components of the electrical field E , which are located at the center of the cube edges parallel to the respective component. The second lattice is used in the same way, but represents the magnetic fields H .

Maxwell's equations (2.1c) and (2.1d) can then be rewritten component-wise

with i, j, k cyclic $\in \{x, y, z\}$:

$$\frac{\partial H_i}{\partial t} = \frac{1}{\mu} \left(\frac{\partial E_j}{\partial k} - \frac{\partial E_k}{\partial j} \right) \quad (4.1a)$$

$$\frac{\partial E_i}{\partial t} = \frac{1}{\varepsilon} \left(\frac{\partial H_k}{\partial j} - \frac{\partial H_j}{\partial k} - \sigma E_i \right) \quad . \quad (4.1b)$$

The partial derivatives are approximated by first order differential quotients with $l \in \{x, y, z\}$:

$$\frac{\partial F^n(i, j, k)}{\partial l} = \frac{F^n(i + \frac{1}{2}, j, k) - F^n(i - \frac{1}{2}, j, k)}{\Delta l} + \mathcal{O}(\Delta l^2) \quad (4.2)$$

$$\frac{\partial F^n(i, j, k)}{\partial t} = \frac{F^{n+1/2}(i, j, k) - F^{n-1/2}(i, j, k)}{\delta t} + \mathcal{O}(\delta t^2) \quad . \quad (4.3)$$

The indices identify the position in space and time subdivided in steps of $\Delta/2$ and $\delta t = \Delta t/2$, respectively. FDTD is a leap-frog type algorithm, where electric and magnetic field are calculated alternately in successive half time steps.

To ensure the stability of the algorithm the following inequality has to be satisfied [123]:

$$v_{\max} \Delta t \leq \left(\frac{1}{\Delta x^2} + \frac{1}{\Delta y^2} + \frac{1}{\Delta z^2} \right)^{-1/2} \quad (4.4)$$

, with v_{\max} being the maximum phase velocity within the simulation volume.

The convergence of the FDTD-algorithm for $\{\Delta t, \Delta x, \Delta y, \Delta z\} \rightarrow 0$ can be demonstrated via the definition of dispersion [123] :

$$\left[\frac{1}{c \Delta t} \sin \left(\frac{\omega \Delta t}{2} \right) \right]^2 = \sum_i^{x,y,z} \left[\frac{1}{\Delta i} \sin \left(\frac{\tilde{k}_i \Delta i}{2} \right) \right]^2 \quad (4.5)$$

$$\xrightarrow{\Delta \rightarrow 0} \left(\frac{\omega}{c} \right)^2 = \sum_i^{x,y,z} k_i^2 \quad . \quad (4.6)$$

If the simulated geometries have curved surfaces, the discretization of space leads to *staircasing*. Figure 4.1(b) shows a sphere, which is discretized by cubic Yee-cells leading to edges and corners emerging in the representation of the originally smooth surface. This has a strong influence on the near-fields of metallic nanostructures close to the surface as depicted for the fundamental dipolar mode of a 10 nm radius gold sphere in Fig. 4.1(c). Four pixels with extreme high field strength emerge in the cross section view due to the lightning rod effect concentrating charges in edges and corners. Comparing with the

analytical solution in Fig. 3.8, the fields behave physically down to very small distances of a few nm, before staircasing leads to unphysical results. Further implications for nano-optical simulations will be discussed in section 4.1.3.

The software used in this work delivers frequency dependent results after a Fourier-transformation of the transient field data. This yields physical results, when the overall simulation time is long enough, so that all power from radiation sources like plane waves, Gaussian focuses or point dipoles has left the simulation volume. This is realized by defining a shut-off criterion, which stops the simulation after the maximum field inside the simulation volume has dropped below a given field strength value of typically 10^{-5} of the maximum field compared to the simulation start. For the broadband simulations within this work the shut-off criterion was set to 10^{-7} or 10^{-8} , instead, to remove artifacts from Fourier-transformation. Alternatively there is an apodisation option that introduces an artificial smooth fade out for the fields in the simulation volume.

FDTD Solutions works with a more sophisticated implementation of the Yee-cell, allowing not only cubic, but generalized cuboid cell geometries. Therefore, it is possible to define areas with differing cell sizes, which is highly beneficial for the simulation of plasmonic structures. For propagating far-field radiation the mesh size should be $\Delta \leq 0.1\lambda_{\min}$ with λ_{\min} being the shortest wavelength within the simulation volume. When metals are involved this rule breaks down, as the near-fields of plasmon resonances show a strong fall-off in a range of tens of nanometers. The optimal Yee-cell size can be determined by a convergence test with subsequent smaller meshing or by a comparison with a representative analytical solution (see section 4.1.3). The possibility to define regions with different mesh sizes for plasmonic problems reduces for many single particle problems simulation time and used disc space by a large margin to a level manageable by commercially available work stations.

4.1.1 Meshing of cubes touching at edges

The convergence of FDTD-simulations of antennas consisting of perfect 10 nm sized gold cubes (see chpt. 7) was tested, with the center of a cube in the coordinate origin. The meshing was forced to be symmetric and the Yee-cell size reduced from 1 nm to 0.5 nm, obtaining the results shown in Fig. 4.2.

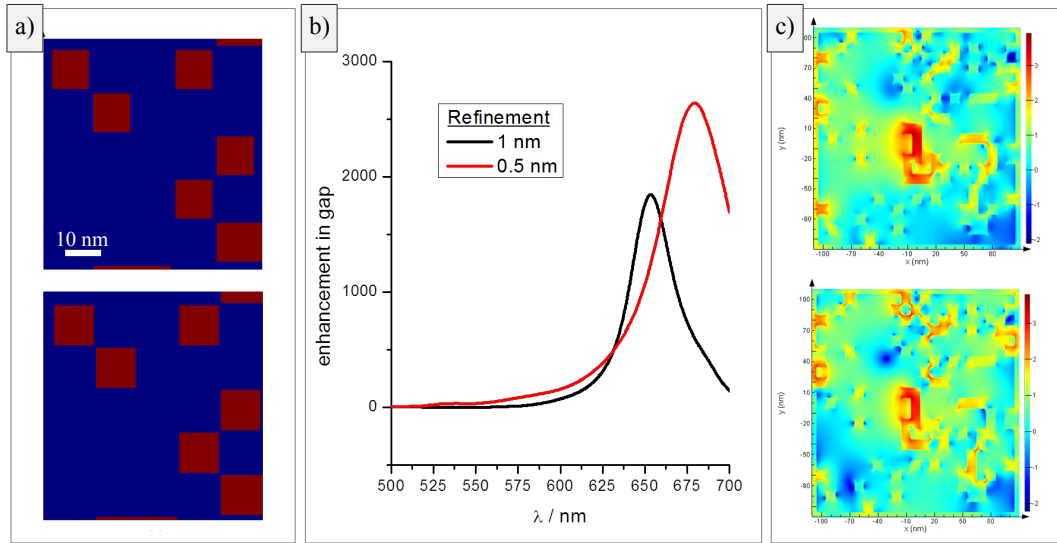


Figure 4.2: Influence of bad meshing on complex antenna simulations [125]. a) Index monitor data showing 10 nm Au cubes arranged edge-to-edge with meshing of 1 nm (top) and 0.5 nm (bottom). b) shift of optimized EA-antenna resonance when changing the meshing from 1 nm to 0.5 nm. c) comparison of near-fields at $\lambda = 650$ nm of the structure with meshing of 1 nm (top) and 0.5 nm (bottom).

In panel (a) data from the material index monitor shows small gaps occurring between cubes which were originally meant to touch at their edges, decreasing with smaller mesh size. Due to the strong capacitive coupling between highly concentrated charge carrier accumulations at gaps (compare with section 3.3.2) small gap deviations lead to big changes in resonance and near-field strength.

This leads to a change in the antenna resonance wavelength of > 25 nm as shown in Fig. 4.2(b). Also the antennas near-field patterns at the optimization wavelength of 650 nm changed (Fig. 4.2(c)). There is a clear reduction of field intensity in the very center as well as a strong enhancement in the holes at the upper-right antenna area and a large field strength drop in the very lower left corner of the geometry, impeding the original functionality of the 1 nm meshed antenna. To avoid this problem, the mesh has to be shifted by half a mesh cell in all three dimensions. This has been done in all numerical results presented in this work, introducing a way to keep distances constant while changing the Yee-cell size.

4.1.2 Materials for FDTD-simulations

Optical parameters of simulated materials can be defined in multiple ways. For dielectric materials with low dispersion, e.g. glass and indium tin oxide (ITO), fixed values from literature were retrieved from an online database [126].

For gold a critical point fit of the values from Johnson and Christy [58] as published in [59] (see section 3.1) has been used to generate 801 data points in the frequency range between 200 and 1000 nm. These data points were imported in 'FDTD Solutions' as basis of a polynomial fit.

Perfectly matched layer

FDTD simulations are performed in a closed cuboid volume terminated by six intersecting planes, which should emulate an infinite continuation of the truncated space. This includes outgoing radiation not to be reflected as well as not to be just removed, as both actions will alter the fields inside the simulation volume. Therefore, an anisotropic material has to be introduced, which dampens an impinging electromagnetic wave while turning its k -vector parallel to its surface and thus avoids reflection. This perfectly matched layer (PML) [127] has permittivity and permeability tensors given as

$$\bar{\epsilon} = \begin{pmatrix} a & 0 & 0 \\ 0 & a & 0 \\ 0 & 0 & b \end{pmatrix} \quad \bar{\mu} = \begin{pmatrix} c & 0 & 0 \\ 0 & c & 0 \\ 0 & 0 & d \end{pmatrix} . \quad (4.7)$$

Ten layers of PML (= 10 Yee cells) are sufficient to dampen a perpendicular impinging plane wave by a factor of 100 dB before it re-enters the simulation volume. Stronger back reflections occur in edges and corners of the simulation volume, where electromagnetic waves have larger impinging angles, but due to scattering from one PML to the next PML, a thickness of 12 layers is sufficient for all simulation tasks with no material penetrating the PML. This is the standard setting within FDTD Solutions and has not been changed in any simulation (a test can be found in [128]). The PML does not dampen near-fields, so it is important to place it at least in a distance of $\lambda_{\text{sim}}/2$ from any metallic material, with λ_{sim} being the largest wavelength occurring within the simulation [123].

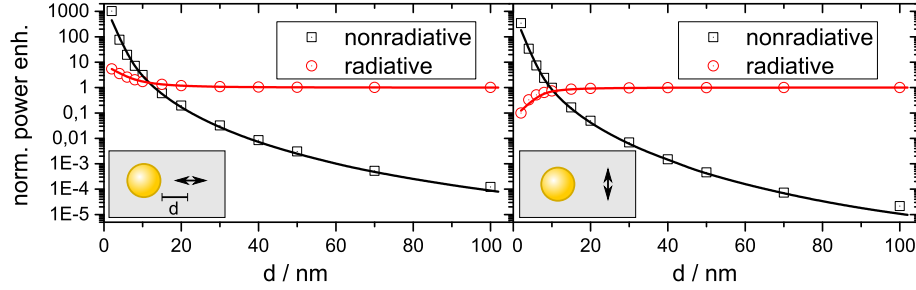


Figure 4.3: Comparison between the analytical solution (solid lines) and numerical results (symbols) for the case of a dipole emitting at $\lambda = 830$ nm near the surface of a sphere (radius = 10 nm) with orientation perpendicular (left) or parallel (right) to the surface.

4.1.3 Comparison to analytical solution

Since the central topic of this work is the coupling between a quantum emitter (QE) and an optical antenna, an analytically solvable system is used as benchmark for numerically investigating the emission power enhancement of a QE (see section 2.3). Figure 4.3 shows analytical results (based on [106]) and numerical data for the radiative and non-radiative power enhancements for the cases of a QE dipolar moment perpendicular and parallel to the surface of a gold sphere with radius $r = 10$ nm emitting at $\lambda = 830$ nm dependent on the distance. A full discussion of the involved physics can be found in section 3.3.3.

The meshing was set to 1 nm in the volume containing the sphere and the dipole plus additional 5 nm in all directions. The overall simulation volume was set to $(1000 \text{ nm})^3$ to ensure the recommended distance between structure and PML of $\lambda/2$.

The simulated data reproduce the analytical solution very well down to dipole-sphere distances of about 4 nm for both radiative and non-radiative power. For 2 nm the simulated non-radiative power gets too large, since stair-casing deforms the near-fields. In addition, the non-radiative part deviates strongly for large distances, as the absolute values approach zero. This originates in FDTD Solutions performing the numerical calculations only with single precision, leading to large relative numerical inaccuracies for such small numbers, which are further exaggerated by the logarithmic plot. However, this is no problem as its absolute value is negligible.

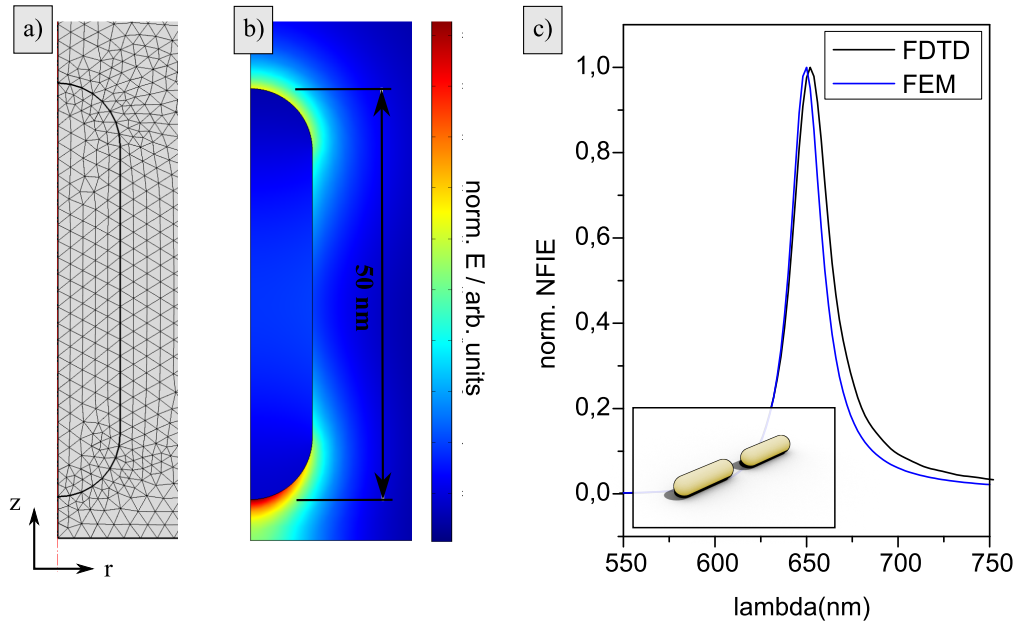


Figure 4.4: Properties of quasistatic COMSOL simulations of a dipolar two rod antenna with a gap of 10 nm, arm length of 50 nm and a cross section radius of 7.5 nm. a) Central part of the meshing of the quarter simulation cross section, when the maximum finite element edge length is set to 2 nm. b) Absolute value of the electric fields obtained from the quasistatic FEM solution. c) Near-field intensity enhancement (NFIE) spectra of both FEM (blue) and FDTD (black) simulations (Inset: Full dipolar antenna geometry).

4.2 The finite element method

The finite element method (FEM) is used in nearly every field of physics and engineering which deals with complex volumes and surfaces. COMSOL is using FEM for the solution of differential equations connected to mechanics, acoustics, heat transport, electrical properties, etc. and, of course, optics.

The method has some advantages compared to FDTD, the most prominent being the discretization of surfaces and volumes as triangles and tetrahedrons. Figure 4.4(a) shows an antenna arm meshed with minimal element dimensions of 2 nm without a visible staircasing effect.

The second big advantage is the possibility to compute rotational symmetric geometries, by calculating a two-dimensional plane only. This can be combined with an additional symmetry plane at $z = 0$ and in the end only one quarter of the 2D cross section has to be computed. However, this does not allow

anymore the implementation of a plane wave or Gaussian focus source, which would be necessary for realistic experimental conditions. Antenna modes and the NFIE can still be retrieved and compared relatively with each other by solving the geometry quasi-statically if the dimensions are small compared to the excitation wavelength. A constant field of 1 V/m is applied on the outer borders of the simulation. Figure 4.4(b) shows the near-fields resulting from the rotation-symmetric quasi-static FEM simulations, looking similar to the mode fields from a FDTD simulation as plotted in Fig. 3.10(b).

To prove the viability of this approach, a two rod antenna with a 10 nm gap, an arm length of 50 nm and a radius of 7.5 nm was chosen as reference with a resonance at $\lambda = 650$ nm. As the thickness of the antenna rod is much smaller than the excitation wavelength, the quasistatic approach is viable. The resulting NFIE spectra for both quasistatic rotational symmetric FEM simulations and FDTD simulations in the very antenna center is shown in Fig. 4.4(c).

There are slight differences, as the resonance of the quasistatic simulation is shifted by 3 nm to shorter wavelength and has a smaller FWHM. The latter can be explained by the absence of staircasing, which increases Ohmic losses of an antenna and thus reduces its Q-factor. The resonance peak shift can have mainly two reasons, on the one hand less coupling across the gap due to missing staircasing near-field hot spots will shift the resonance to shorter wavelength, on the other hand the effective thickness of the rod can be larger, also leading to a resonance shift to higher energies. Both effects can be explained with the omission of staircasing.

The main advantage is simulation time: while a single FDTD simulation takes about 20 – 40 min, the complete quasistatic wavelength sweep takes only about 50 s. This makes it a viable tool for testing more complex geometries for general functionality, before the final data are retrieved with full wave FDTD simulations.

4.3 Evolutionary optimization

Nowadays, it is consensus that life on earth has developed to the actual state with algae and trees, frogs and birds and humans by means of evolution, beginning with the humble starting condition of self-replicating amino acid complexes [129]. The concept of encoding properties of single individuals in a genome which then can be mutated and recombined with other individuals genomes is obviously a powerful method for adapting life to a enormous variation of environmental boundary conditions.

Therefore, it is not especially surprising that in computer science biological evolution inspired a variety of approximation algorithms. These generate 'good' solutions to very complex problems, which can either only been solved exactly with extreme computation time, might have no analytical solution (yet) or are even not fully understood, thus making it impossible to define the properties of an optimal solution. But whenever it is possible to define an *environment* represented by a *fitness function*, evolutionary algorithms (EA's) are a good choice to find a good, but most likely not the best solution to the posed problem in an acceptable time.

The seminal work for the application of genetic algorithms (GA's) - a special case of EA - was published in 1975 by John H. Holland [130]. Today GA's are used to solve problems in many aspects of our lives e.g. automobile design [131], robotics [132] or financial trading [133].

4.3.1 Definitions and working principle

The terminology for evolutionary algorithms is derived from biology, despite some changes due to introducing countable quantities for the work within a computer program:

individual: Single entity S representing a possible solution to the given problem.

environment: Originally, the setting where an individual has to be able to survive and outperform other individuals. Generalized, this is the definition of the problem to be solved.

fitness function and fitness: The fitness function is a mathematical relation $F(S) \rightarrow f_S$ which assigns to an individual S a real-value fitness f_S . The fitness is a measure for the performance in the given environment and therefore for the quality of the solution S to the posed problem. For a given problem an infinite number of fitness functions exist and its choice is crucial as it has not only to represent the posed problem correctly but also ensure the efficient selection of more sophisticated structures as parents of the next generation.

genome: Complete representation of an individual. In computer applications a genome is mostly a linear (binary) string g consisting of '1' and '0'. The use of a genome within an evolutionary algorithm defines it as a more specialized genetic algorithm.

generation: Set of individuals \mathbf{G}_n , which exist at the same time and compete for the right to pass on their genomes to the next generation. The individuals of generation \mathbf{G}_n are children of \mathbf{G}_{n-1} and parents to \mathbf{G}_{n+1} .

population: In this work every individual of any generation belongs to the (ever growing) population, contrary to the case of only the actual/last generation being the population. The solution of a GA is the best individual of the population after a given number of generations or after fulfilling an abort condition.

inheritance: This is the core mechanism of any GA. By *mutation* and *crossing* of parent genomes the individuals of consecutive generations are built from the individuals of the preceding generations, but with random alterations or mixed from two parents to find new and even better individuals. In general only the fittest individuals of one generation are allowed to pass on their properties, thus, realizing a continuous improvement of fitness.

4.3.2 Evolution for plasmonics - previous work

While in radio-frequency (rf) antenna research many different optimization algorithms have been applied with success [89, 134], until now¹ only a few pub-

¹August 2015

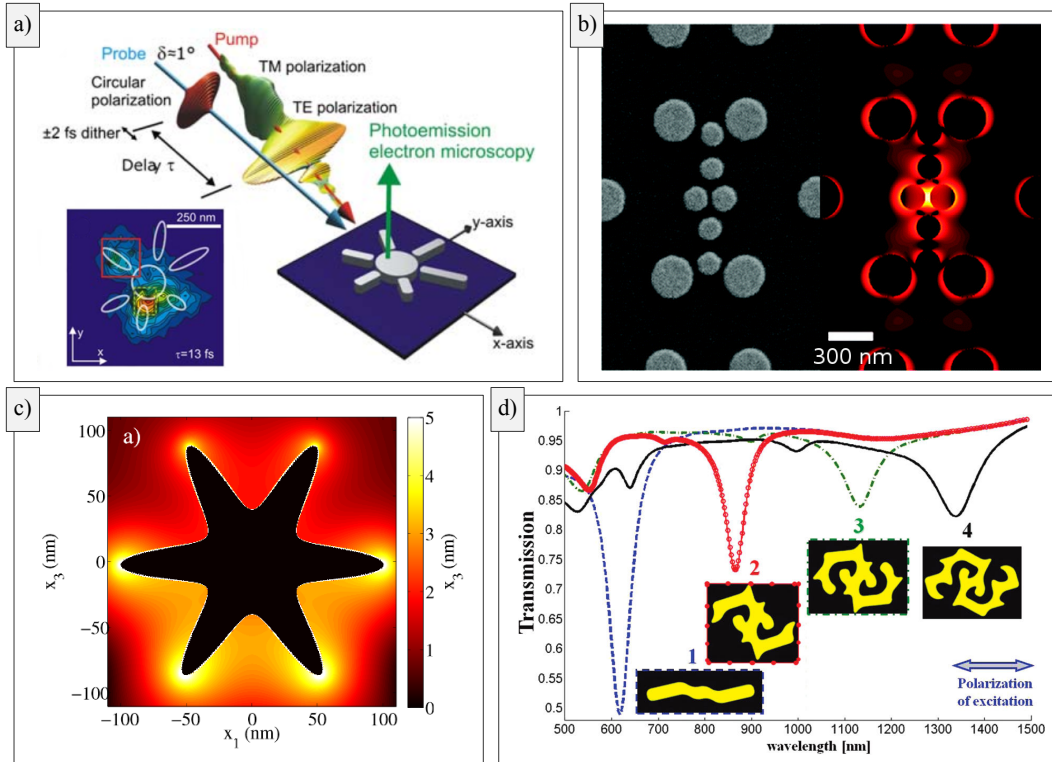


Figure 4.5: Examples of evolutionary algorithm approaches for optimization of plasmonic nanoparticles. a) An evolutionary optimized ultra-short laser pulse is used to excite a complex structure with several resonances. The control of the near-field hot-spot position is shown in the inset, where the red square marks the illumination area and the green square the desired place of the hot spot (reprinted with permission from [135]). b) Multiple cylindrical gold patches are positioned and scaled to achieve a high near-field enhancement for a given frequency (left: SEM; right: simulation; reprinted with permission from [136]). Copyright 2012 American Chemical Society). c) Parameters of an analytically describable complex shaped wire cross-section are optimized to guide plasmonic modes of a desired frequency [137]. d) The shape of a single nanoparticle is changed within geometric constraints feasible for nanofabrication to maximize a plasmon resonance at a given wavelength (reprinted with permission from [138]). Copyright 2011 American Chemical Society). c) and d) are numeric only studies.

lications exist combining evolutionary optimization with plasmonic structures for optical frequencies. Basically three different concepts have been employed, all limited in the geometrical configuration space. Fig. 4.5 shows an overview over the different EA approaches.

Panel (a) shows the excitation optimization by means of coherent control [135, 139]. The amplitude and phase of the spectral components building up a very short laser pulse are altered to get maximum control of near-field spatial and temporal behavior in complex plasmonic geometries. Originally applied to influence chemical reactions, the pulse forming itself via liquid-crystal cells is optimized by means of evolutionary algorithms for a given plasmonic structure. This allows to steer light through a forking waveguide made from cylindrical constituent particles, localize near-fields in space and time for e.g. a "sun-shaped" heptamere (depicted) and to enhance near-field localization in rough and random metal thin films [140]. This approach does not deliver antenna geometries for specified applications, but can be used to foster the fundamental understanding of e.g. SERS.

Another type of EA either works with a given regular grid of particles, which can be switched 'on' and 'off' [141, 142] or with a given amount of particles with free choice of position and size [136] (Fig. 4.5(b)). The goal of the optimization is a high near-field enhancement for broad-band and single frequency applications, respectively. Both works do not change the geometry of the single particles but stay with spheres and cylinders, examining the response to plane wave excitation. The result is, that scattering structures gather energy from the far-field, re-routing incoming light with the correct phase for constructive interference to the central parts of the structures responsible for near-field localization. The center shows gaps as small as the restrictions of the algorithm allow.

The last type of algorithms takes the shape of individual structures as variable: The propagation properties of a metallic nanowire with a complex shaped cross section has been optimized in [137] (Fig. 4.5(c)). The geometry can be described analytically, but only within narrow constraints. A comparable approach for 3D particles based on the geometries described by Gielis superformula has been used in [143] to optimize the incoupling of solar light to solar cells. More flexible is an approach, which allows the shape of a single, point symmetric particle to change freely, under the restriction of curvatures feasible for fabrication [138] (Fig. 4.5(d)). It has been shown, that the scattering cross section can be optimized for a given wavelength.

All these approaches have major restrictions in geometry and applicability.

This work will introduce a more general approach to an EA for optimization of plasmonic geometries in chpt. 7, which is then adapted to geometries feasible for FIB structuring in chpt. 8. Finally, a new theoretical approach to explain the coupling between single emitter and optical antennas will be presented in chpt. 9, able to explain the functionality of the geometries yielded by the EA.

Chapter 5

Fabrication

The fabrication of nanometer sized metal structures is laborious and often involves expensive devices like the recently developed helium ion microscope [144, 145] together with some amount of craftsmanship or highly sophisticated chemical recipes, using even DNA-origami [146]. There are two main approaches to achieve controlled nanopatterning: *top-down* and *bottom-up*. The first section will present examples of these approaches representing the state of the art of plasmonic structure production. The second and third section will introduce a relatively new approach combining both bottom-up and top-down strategies: monocrystalline gold-flakes created by means of wet chemical synthesis are treated by focused-ion-beam (FIB) milling to carve the desired geometries.

5.1 State of the art

Top-down fabrication is starting with a volume or a thin film of a basic raw material to be shaped by means of eroding tools. This allows the fabrication of highly sophisticated structures on large areas with nearly arbitrary shapes [147]. Bottom-up fabrication, on the other hand, uses basic building blocks with a simple geometry. These mainly chemically grown components are then assembled to larger and more complex structures by means of nanomanipulation or self organization. Both approaches had large impact on the big success story of recent plasmonics research, but have both pros and cons, which will be discussed at the example of realizing sub-nanometer gaps in gold.

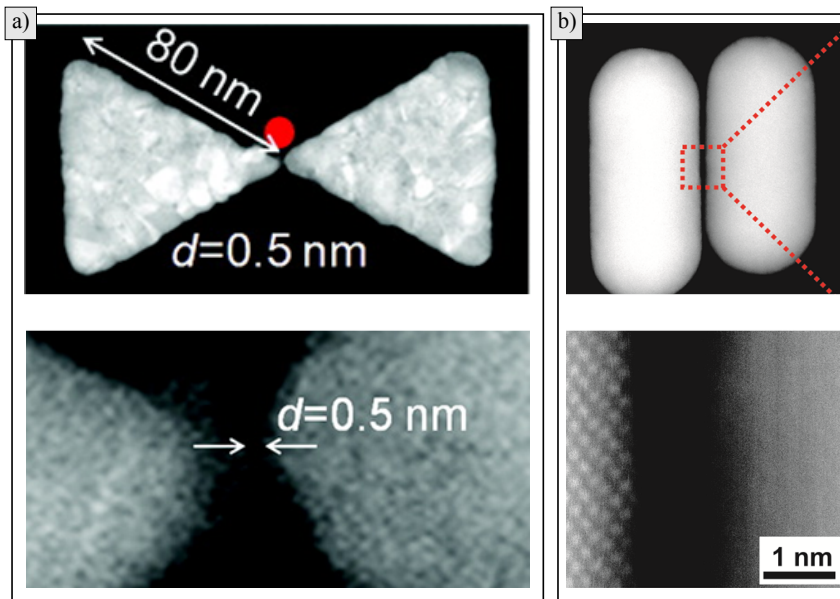


Figure 5.1: Examples of sub-nanometer gaps in plasmonic structures. a) STEM images of a bow-tie antenna with a gap of ≈ 0.5 nm realized via electron-beam-lithography of evaporated gold (reprinted with permission from [36]. Copyright 2012 American Chemical Society). b) Cavity with gap ≈ 0.5 nm obtained via self-organization of chemically grown gold nanorods (reprinted with permission from [148]. Copyright 2012 American Chemical Society). In both panels the upper part shows SEM-pictures, the lower parts TEM-measurements for gap size determination.

Figure 5.1(a) shows a bow-tie antenna made from gold realized by means of electron-beam-lithography. A thin layer of resist is deposited on top of a thin layer of evaporated gold, which is exposed to controlled electron beam radiation. Depending on the resist, the (un-)exposed areas are removed chemically and the remaining material serves as mask in the final etching process. The limits of this method are dependent on the resist material, as the electron beam always develops more material than expected by its nominal beam diameter due to scattering and secondary electron generation. The direct writing of lines with a width of 10 nm seems to be the resolution limit for HSQ as resist [149]. However, using the proximity effect allows to fabricate smaller gaps, if they are quasi-zero-dimensional. For example, two very close, yet not touching triangles can be created in the pattern generator. Due to the e-beam having a finite diameter, the resist is also developed in the 'non touching area', which allows to surpass the nominal resolution. This recipe also works for FIB milling.

The gold material for the bow-tie antenna is a thin film evaporated via electron-beam-deposition, resulting in polycrystalline raw material. Each crystallite has a different orientation and, therefore, a slightly different etching rate. This makes the fabrication not fully controllable in the length scale of the polycrystallinity and defined small gaps are a matter of luck. One has to produce many similar structures to realize a few with the desired geometry. The single crystallites are distinguishable in Fig. 5.1(a), however, gaps sizes below 1 nm could be realized. This approach breaks down, when the desired overall geometry gets more complex (compare to Fig. 5.4(e)).

Figure 5.1(b) shows a cavity realized by self assembly of two chemically grown gold nanorods. The gold of these single rods is monocrystalline, yet the 'structuring' is quite uncontrolled: the length and thickness of the single rods is not monodisperse, but follows a statistical distribution and the positioning of the structure is performed by dropcasting a solution with an optimized rod concentration. This approach delivers in addition to dimers many singular rods as well as trimers and higher order clusters. In general structures resulting from bottom-up approaches have a supreme material quality but the building blocks are only available in simple shapes as spheres, cubes, rods, . . . , and are difficult to position. This makes it extremely difficult until today to build

large area structures like e.g. long wave guides with corners with a bottom-up approach. At least the positioning problem can be tackled to some extent by means of DNA origami [146].

5.2 Focused ion-beam milling with Ga

Milling with a focused beam of accelerated gallium ions (FIB milling) has proven to be a viable material erosion tool, capable to work very controlled also in complex environments, e.g. on AFM-tips, when other techniques like electron beam lithography cannot be applied. The only requirement is the sample to be conductive, so that it does not charge during treatment, which would distort the ion beam. The working principle of an ion column is comparable to a scanning electron microscope, except the ion source being a cone with a sharp tip pointing downwards covered with a thin layer of liquid gallium (Ga). A strong electrical potential applied at the cone ionizes Ga-atoms at the tip apex, which then get repelled by electrostatic forces and leave the liquid. This works as a point-like source of Ga-ions which are accelerated further, focused and spatially controlled by electron optics.

Accelerated Ga-ions have multiple effects on hitting the target material, which are depicted in Fig. 5.2. The simplest and also the desired behavior for structuring is a Ga-ion being reflected back into the vacuum chamber after depositing a fraction of its kinetic energy in the top layer of the target, sputtering atoms. By steering the ion beam in a controlled path over the target, complex structures can be carved from the material. The Ga-ions can also penetrate the target material, leading to (i) doping of the target (also called implantation), which is a major problem for structuring semi-conductors and (ii) amorphisation, where the crystal structure of the target is broken up by the kinetic energy of the decelerating Ga-ions. Finally a fraction of the ablated target atoms redeposit at the target surface nearby the patterning position. In all these interactions also electrons are set free, which can be used for imaging.

All FIB-milling in this work was performed with a Helios NanoLab Dual-beam system from FEI, capable of performing combined SEM and FIB within the same vacuum chamber. The acceleration voltage for the Ga-ion beam was always 30 kV to ensure maximal resolution, which is nominally 4 nm. For the

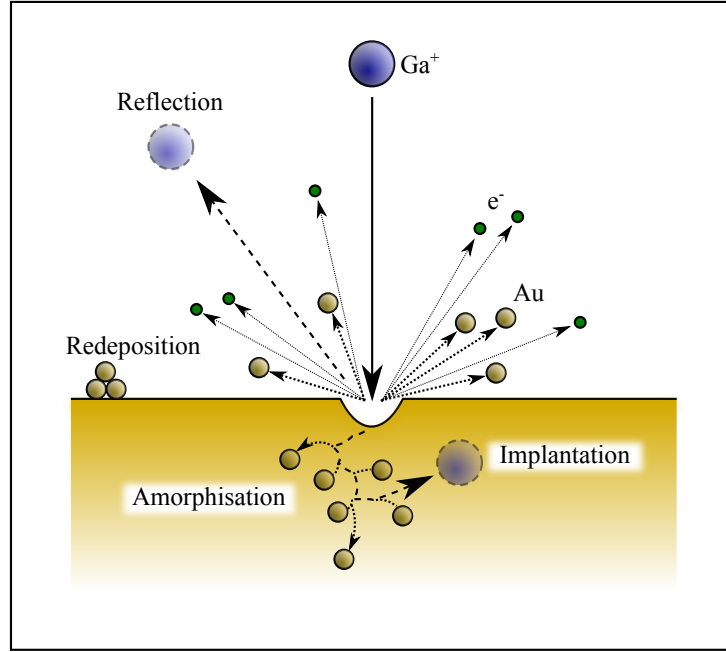


Figure 5.2: Impact of accelerated Ga-ions on a gold substrate. The various effects are discussed in the text.

structuring of plasmonic geometries the beam current was always set to the minimal value of $I_{\text{beam}} = 1.5 \text{ pA}$, to avoid beam widening due to electrostatic repulsion of the ions. Soft materials (like gold), sample drift and charging effects reduce the resolution further, making it necessary to optimize parameters for each material/acceleration voltage/beam current combination.

5.3 Monocrystalline gold flakes

The ideal basis for nanostructuring would be a thin, yet large area monocrystalline metal film for further treatment with top-down approaches. The wet-chemically synthesis of nearly monocrystalline flakes in a bottom-up process provides such a substrate made from gold. These flakes can easily be drop-casted from a solution, and, thus, replace evaporated gold as two-dimensional raw material of high quality [150].

The recipe to grow gold flakes in solution is illustrated in Fig. 5.3: An aqueous solution of hydrogen tetrachloroaurate ($\text{HAuCl}_4 \cdot 4\text{H}_2\text{O}$) is heated to 50°C and then reduced via addition of ethylene glycol. After a few seconds small gold crystal seeds have grown and aniline is added, which will cover the

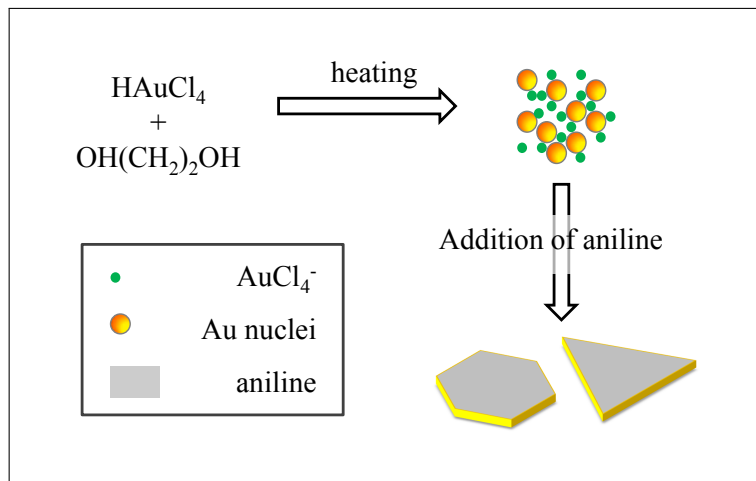


Figure 5.3: Recipe for the chemical syntheses of monocrystalline gold flakes: the gold salt HAuCl_4 is reduced by means of ethylene-glycol. Aniline is added after a few seconds to cover the (111) surface of the emerging gold crystal seeds prohibiting their growth in one dimension, ensuring two-dimensional monocrystalline flake growth (repainted [151]).

(111)-surface of the crystallites and thus prevent further gold atoms to attach at this crystal facet. Therefore, further growth is only possible perpendicular to the (111)-surface and the resulting crystals have the shape of thin platelets. After 48h at constant temperature of 50°C the reaction is stopped and the resulting flakes are cleansed by multiple solvent exchanges to ethanol. The flakes have a side length of up to $100\ \mu\text{m}$ showing shapes from triangular to hexagonal, and thicknesses between 40 and 80 nm, constant within one flake. A more detailed study revealed the existence of a few planar defects parallel to the (111)-plane in probably every flake [152].

Figure 5.4(a) shows monocrystalline gold flakes as drop-casted on an ITO covered glass substrate. Panel (b) shows a close-up of a small rectangle milled into a flake. The flake as well as the milling edges are smooth within the SEM resolution, while an evaporated 30 nm thick Au film shows a rough surface due to it consisting of crystallites with different orientations (Fig. 5.4(c)). A transmission electron microscope (TEM) analysis reveals minor irregularities of a FIB cut edge as depicted in Fig. 5.4(d). While the crystallinity keeps intact, redeposited particles lead to a roughness of about 2 nm. Figures 5.4(e) and (f) show SEM images of an elongated two-wire transmission line, fabri-

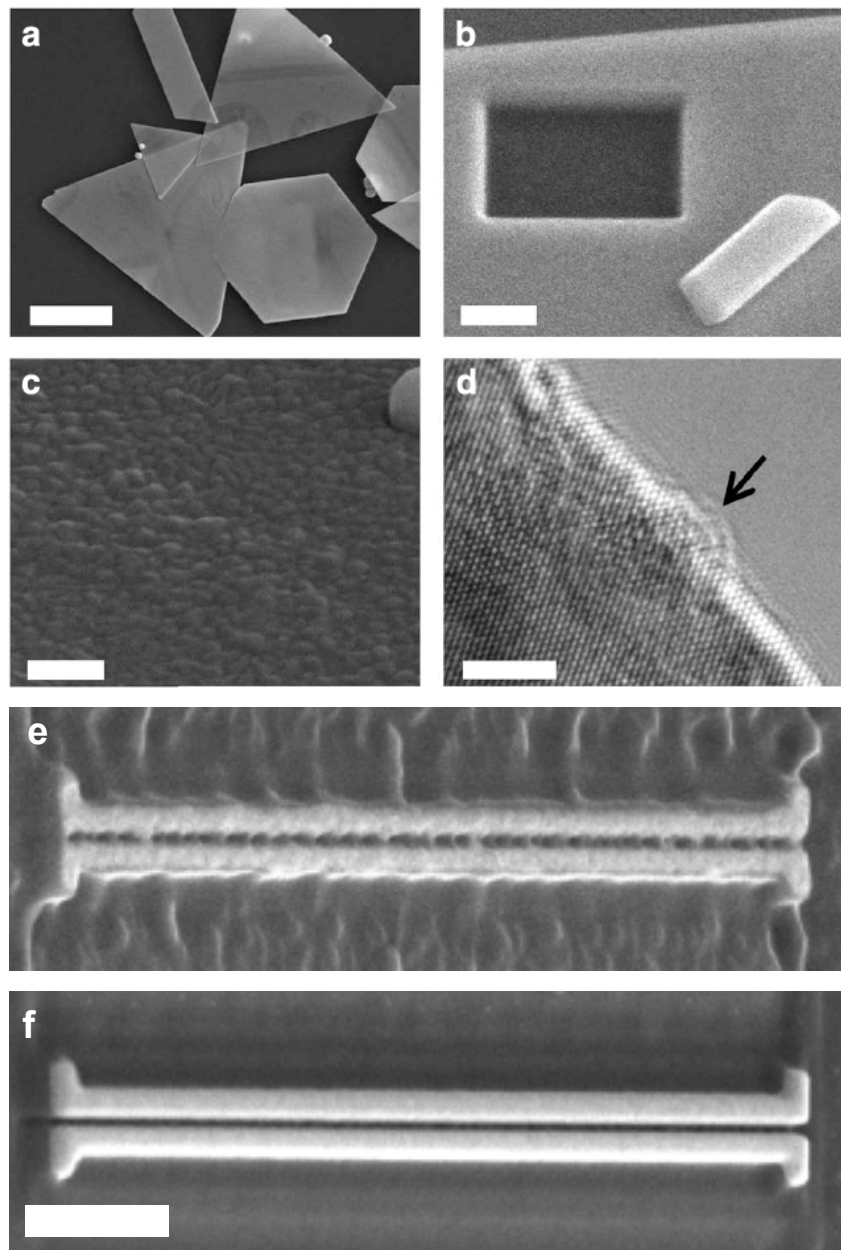


Figure 5.4: Properties of chemically grown gold flakes [150]. a) Stack of flakes as drop-casted direct on ITO-covered glass (SEM; scale bar $5 \mu\text{m}$). b) Zoom in of the surface of a gold flake with FIB-milled rectangle (SEM; scale bar 200 nm) c) Rough surface of evaporated gold on the identical substrate (SEM; scale bar 200 nm). d) High-resolution image TEM of a FIB-cut flake edge. The arrow points at a redeposited particle (scale bar 2 nm). e) and f) Comparison between two-wire transmission-lines with 25 nm center trench build from different substrates: e) 30 nm of electron beam evaporated gold. f) gold flake polished to a height of 30 nm (scale bar 500 nm).

cated in evaporated gold and in monocrystalline gold flakes, respectively. For evaporated gold the center gap is very irregular and at some points shortcut. This will hamper the desired functionality, leading to highly damped plasmon propagation. However, with flakes as substrate plasmonic nanostructures with geometric features of high aspect ratio can be built reproducibly, enabling sophisticated waveguide geometries [90, 153].

5.4 Sample preparation

For fabrication of plasmonic structures, which are optical accessible through the substrate as well as conductive for imaging by means of SEM and treatment by means of FIB, the following recipe was used: Microscope cover slips (Menzel, $24 \times 24 \text{ mm}^2$, 0.17 nm thick) were covered with 200 nm of sputtered ITO. A gold marker structure was evaporated and processed by means of optical lithography. Wet-chemically grown gold flakes were drop-cast and the resulting sample was plasma cleaned for 60 s in a 30 W low pressure oxygen plasma. Then selected areas of the gold flakes were polished down to the desired thickness of 30 nm by means of FIB milling

Polishing As the thickness of chemically grown gold flakes is statistically distributed between about 40 to 80 nm, the desired height of a future nanostructure has to be predefined by polishing an area of the flake. For this an ion current of 48 pA was chosen, allowing the ablation of more material per time as resolution is no issue in this step. First the milling depth has to be calibrated, since the predefined material milling parameters of the machine are only guidelines and the aperture of the machine is subject to degradation over time due to constant ion damage, leading to an ion current increase over time. Atomic force microscopy (AFM - see next chapter) measurements of the ablation rate lead to a calibration curve as depicted in Fig. 5.5(a). A linear fit intersecting with the origin delivers a scaling factor between the set value and the final value, e.g. of 1.396 ± 0.015 .

Figure 5.5(b) shows an AFM image of a flake with pristine, polished and patterned areas containing the final optical antenna geometries. The pristine flake has a thickness of $48 \pm 1 \text{ nm}$ (area marked green) and the polished area is

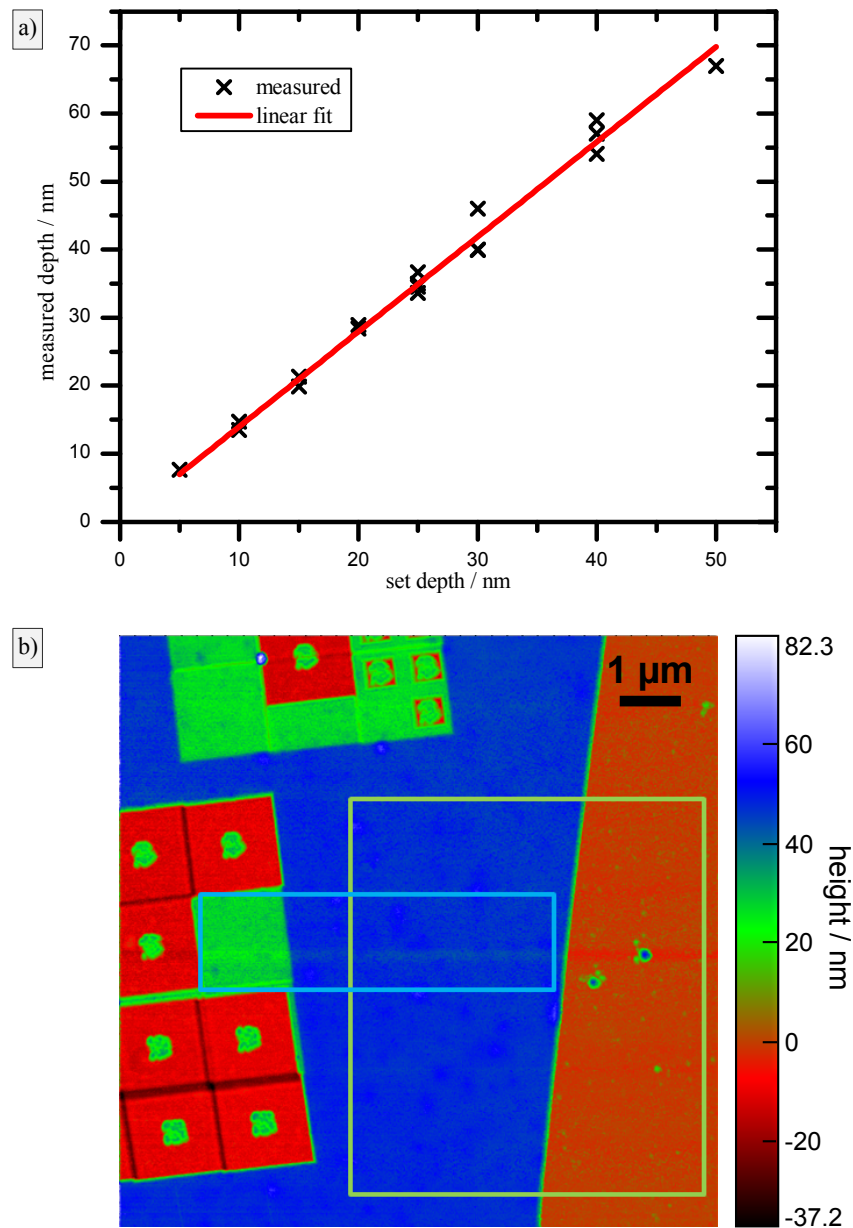


Figure 5.5: a) Calibration of FIB-polishing: for a given ion current of 48 pA and acceleration voltage of 30 kV the set depth values are compared with AFM measurements, yielding a linear calibration factor. b) AFM measurement used for the determination of optical antenna thickness. The green and blue marked areas were used to evaluate height histograms.

reduced in height by 20 ± 1 nm (area marked blue). This results in a measured optical antenna thickness of 28 ± 2 nm, which is only slightly less than the intended 30 nm.

It has to be mentioned, that polishing flakes on glass with the given beam properties deposits a lot of heat in the gold, leading to the formation of bubble-like surface deformations, when the refresh-time – the time between two FIB milling passes – is not set to a very large value of 500 ms. This leads to very long structuring times, which can be avoided by using a substrate with better heat conductivity (e.g. Si), or by decreasing the ion acceleration voltage to 10 kV. Then monocrystalline gold layers with thicknesses down to 10 nm can be realized [152].

Chapter 6

Characterization

Optical characterization of plasmonic nanostructures is not straight forward, as their geometrical features are often smaller than the diffraction limit. Scanning near-field optical microscopy seems to be the method of choice and has been employed with great success. Today it is possible to map plasmonic mode-fields in a three-dimensional volume [154,155]. However, also far-field techniques like confocal microscopy can be used to examine simple optical antennas, as non-linear processes deliver information about modal near-field patterns dependent on the excitation position [101].

This work relies on far-field detection only. Therefore the first section of this chapter introduces the physical principles of two-photon photo-luminescence (TPPL), which is a non-linear process used to retrieve information about the near-field concentration within plasmonic structures. The confocal microscopy setup used within this work is then described in the second section.

6.1 Two-photon photo-luminescence

Illuminating a metal with monochromatic light with energy sufficient to excite a valence (= d-band) electron into an unoccupied conductance band state (= sp-band), gives rise to a broadband photo-luminescence (PL) response due to non-radiative relaxation prior to re-emission of a lower energy photon [156]. The PL-spectrum can be used to examine the band structure of metal films [157], but can also reveal resonance positions of plasmonic nanostructures [148].

For pulsed illumination with high peak power, the photon density is suffi-

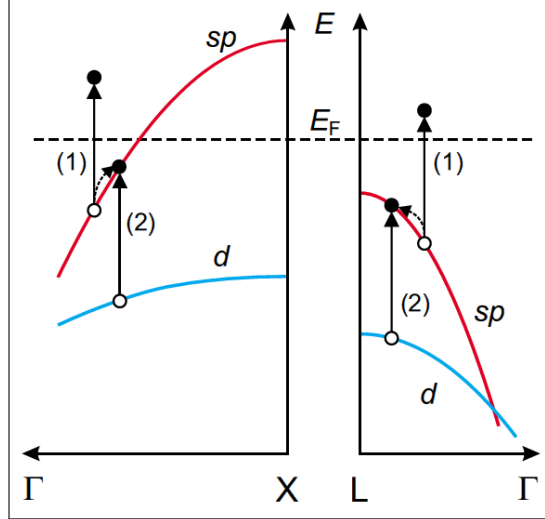


Figure 6.1: Bandstructure of gold with the photon induced electron transitions involved in TPPL [99]. The sp -band (conduction band) is sketched red crossing the Fermi energy E_F , the d -band (valence band) is sketched blue. The abscissa denotes the position within the Brillouin-Zone.

cient to give rise to two-photon photo-luminescence (TPPL), where two photons are absorbed consecutively. TPPL allows the imaging of plasmonic modes for large geometries [158] and the discrimination between modes for simple geometries smaller than the diffraction limit, when prior knowledge about the involved modes is available [101].

Figure 6.1 shows the band structure of gold together with the involved processes for TPPL. A first photon excites an intraband transition in the sp -band (step (1) in Fig. 6.1). The hole starts to relaxate to the Fermi level in a time scale of ≈ 1 ps [99]; in the meantime a second photon is able to perform an intraband excitation from the d -band into the hole (step (2)). Finally, the first excited electron and the second excited hole recombine, emitting a photon with a maximum energy of the two photons.

TPPL can be used to experimentally probe the relative change of near-field intensity enhancement (NFIE) of optical antennas with a high signal-to-noise-ratio [101]. Since TPPL is a two-photon process, its emission intensity I_{TPPL} scales with the squared excitation field intensity. Thus, numerical results of optical antennas allow to calculate the TPPL signal in good approximation via the integral of the forth power of the electrical field \mathbf{E} within the volume

of the antenna V_{ant} [159]:

$$I_{\text{TPPL}} \propto \int_V \mathbf{E}^4 dV_{\text{ant}} \quad . \quad (6.1)$$

Yet, the TPPL process is dipole forbidden and needs strong field gradients introduced by the curvature of the nanostructures, leading also to vanishing signal at flat metal films. Due to its proportionality to E^4 inside the material the vast majority of the TPPL signal emitted by focusing optical antennas originates from the volume near the hotspot, providing an integrated measure for the relative amount of NFIE present in an individual antenna. However, a given NFIE can be realized by different geometries using varying amounts of material, leading to differing TPPL signals. Thus, the comparison of TPPL signals of different optical antennas is only meaningful, when the geometry at the volume of highest near-field concentration is very similar.

As final remark, it is important to distinguish TPPL from second harmonic generation (SHG), where two photons are absorbed simultaneously [160, 161].

6.2 Scanning confocal microscopy

All optical measurements were performed with a self-built confocal microscope setup (see section 2.2 for the working principle) capable of imaging and spectroscopy (full setup sketched in Fig. 6.2). Together with the option to use multiple light sources, different filter sets and an atomic force microscope (AFM), this setup is able to analyze multiple parameters of optical antennas. Only the parts used for the measurements presented in this work will be described in detail.

The excitation for the TPPL scans is realized with a frequency coupled femtosecond-pulsed Ti:Sapphire laser (Coherent Mira 900) at $\lambda = 830$ nm with a pulse length directly after the laser of 150 fs. After a single mode fiber used for spatial filtering and creating a point light source the pulse length is about 1 ps (measured with a CARPE auto-correlator; A.P.E., Berlin), which is sufficient for the desired TPPL excitation of gold (see previous section). After collimation of the beam its polarization was linearized with a broadband $\lambda/2$ -plate (FocTec; 700 – 1000 nm). A neutral density filter allows excitation power adjustment and a 50:50 non-polarizing cube-beam-splitter separates excitation

and detection beam path. The excitation light enters the back of a NA=1.4 oil immersion objective (Nikon 100x Plan-Apochromat) which is attached on a PIFOC (Physical Instruments) for focusing. The sample is fixed on a closed-loop x - y -piezo stage (Physical Instruments, $100\ \mu\text{m} \times 100\ \mu\text{m}$ scan range) for scanning through the focus.

In the detection light path after the 50:50 beam-splitter a holographic 830 nm notch-filter (OD > 6.0; Kaiser Optical Systems) blocks the direct reflection of the excitation beam. Two additional shortpass-filters (both Semrock; SP785 & SP680) ensured that only the TPPL-signal arrives at a single photon counting module (Perkin-Elmer SPCM-AQR 14). Additional polarizers can be inserted in both excitation and detection beam path to analyze polarization dependencies of optical antennas. For comfortable sample positioning a flip mirror allows to image the sample with a CCD camera.

Atomic force microscopy All information about the topology of gold flakes and optical antennas was acquired by atomic force microscopy (AFM) under ambient conditions with tapping mode operating at a resonance frequency of 240–280 kHz and a scanning rate of 0.2 Hz (DMLS scanning head, Nanoscope IIIa, Digital Instruments).

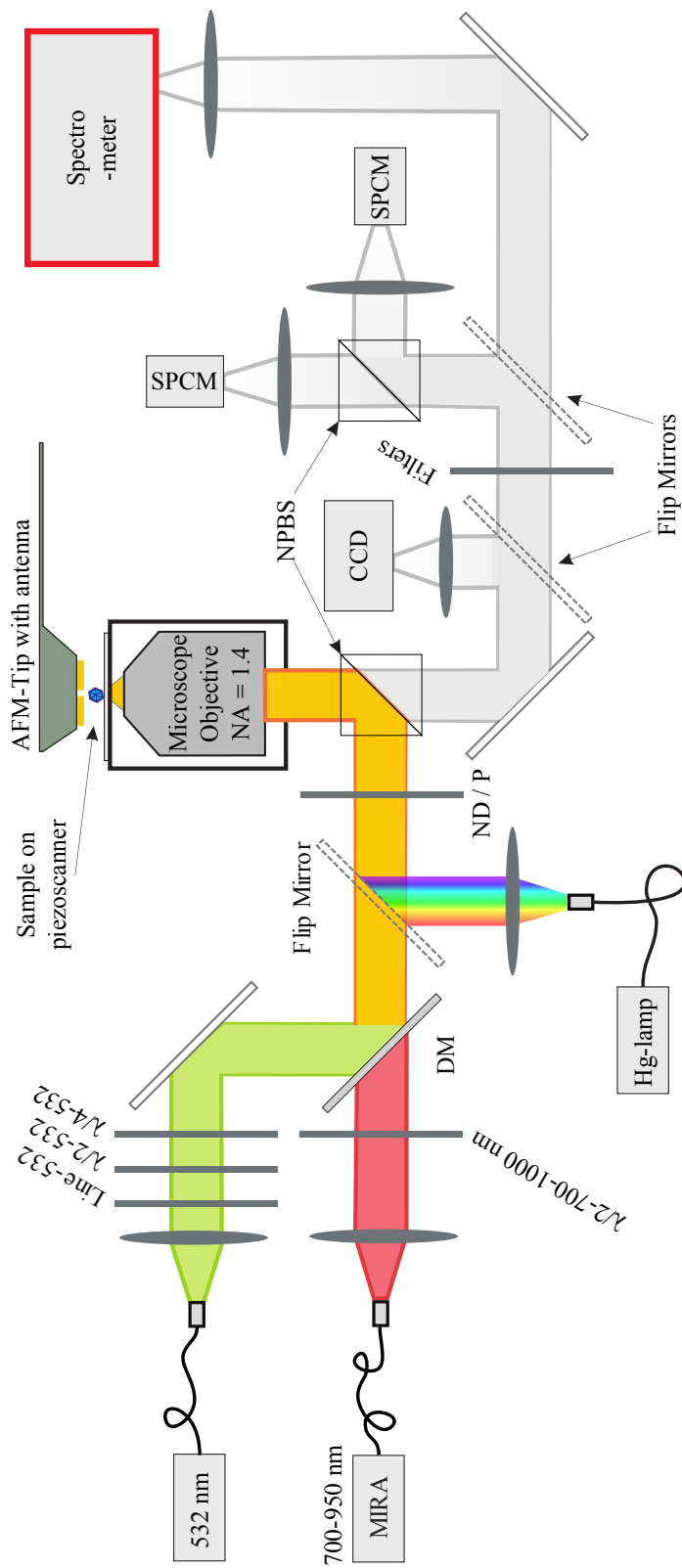


Figure 6.2: Sketch of the self-built optical setup used for all presented measurements. Three different light sources can be used to excite a sample positioned on a scanning piezo-stage above an immersion objective. Additional an AFM can be used in parallel. The detection is possible with a CCD-camera, with single photon counting modules (SPCM) or with a spectrometer. DM: dichroic mirror, ND: neutral density filter, P: polarizer, NPBS: non-polarizing beam splitter. Detailed information in text.

Part III

Results

Chapter 7

Evolutionary optimization of 2D focusing optical antennas

A checkerboard-type implementation of an evolutionary algorithm (EA) starting with random geometries will be introduced to optimize plasmonic nanostructures for focusing far-field radiation in a single near-field hot spot. The fittest (=best) resulting structure surpasses a classical dipole reference antenna by a factor of 2. It can be reduced to a simplified geometry resembling a split-ring-two-wire antenna hybrid. By shifting the $n=1$ split-ring resonance into the optical regime it outperforms optical antenna designs inspired by rf-technology¹.

For the vocabulary used to describe evolutionary optimization as well as for an overview on previous application in plasmonics, see section 4.3.

7.1 Algorithm

A genetic representation of complex-shaped thin-film nanoantennas is realized by composing structures (matrix antennas) from discrete gold cubes with fixed dimensions ($10 \times 10 \times 11 \text{ nm}^3$) positioned on a 21×21 square matrix in vacuum. The genetic information is represented in a unique binary code, where matrix elements are set to '1', if occupied by a gold cube and to '0' when empty (see Fig. 7.1(a)). An example showing a bow-tie antenna represented in a 5×5 array is depicted in Fig. 7.1(b). The resulting configuration space of about $4 \cdot 10^{132}$

¹Most of this chapter has been published nearly identically in [102].

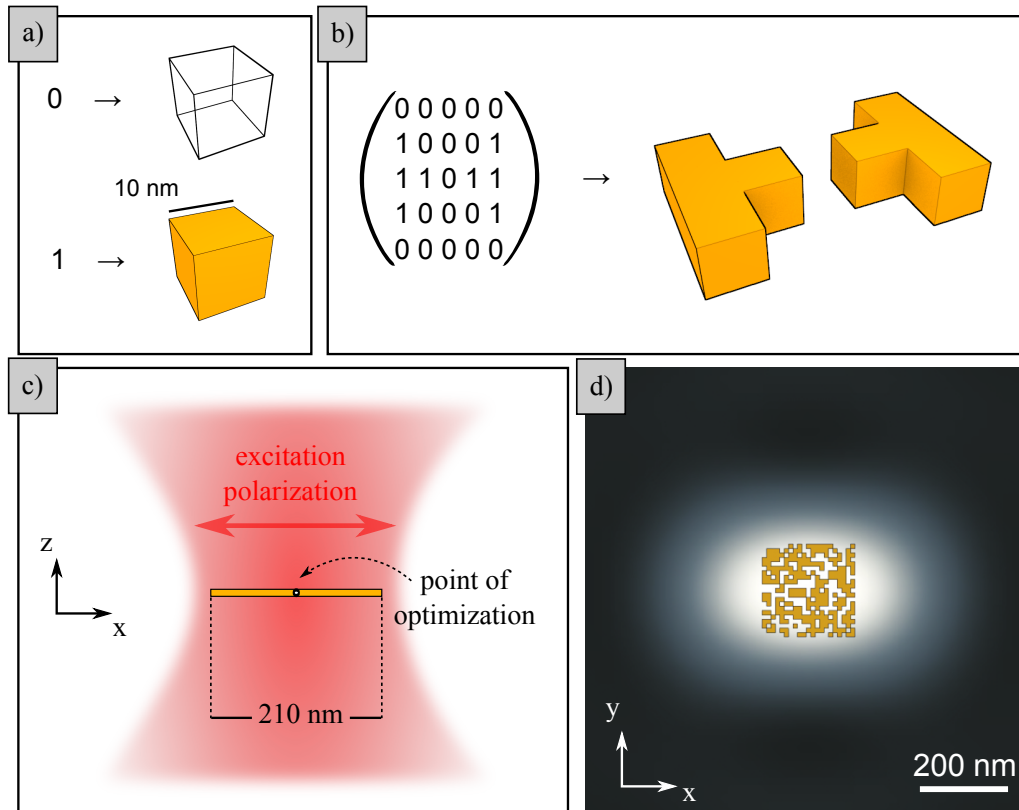


Figure 7.1: Binary encoding and simulation of evolutionary plasmonic nanostructures: a) Translation of '0' to a cube of background material and of '1' to a cube of gold. b) Example 5×5 matrix and its corresponding matrix antenna. c) Side view of the simulation setup, a Gaussian focus illuminating the floating matrix antenna. d) Size of the evolutionary antenna (yellow) compared to the Gaussian focus (greytones) in the antenna plane [102].

different individual structures ensures geometrical variety but is impossible to explore by brute force methods, since the evaluation of an individual structure takes about 20 minutes.

As fitness parameter we choose the normalized near-field intensity enhancement (NFIE) in the focus of an illuminating Gaussian beam ($\lambda = 647$ nm, $NA = 1$, 4.3 fs pulse duration, 144 nm bandwidth) centered on the antenna as illustrated in Fig. 7.1(c). The size of the focal spot and the area occupied by the gold cube matrix are comparable (see Fig. 7.1(d) and section 2.2), ensuring that the whole matrix antenna area influences its fitness.

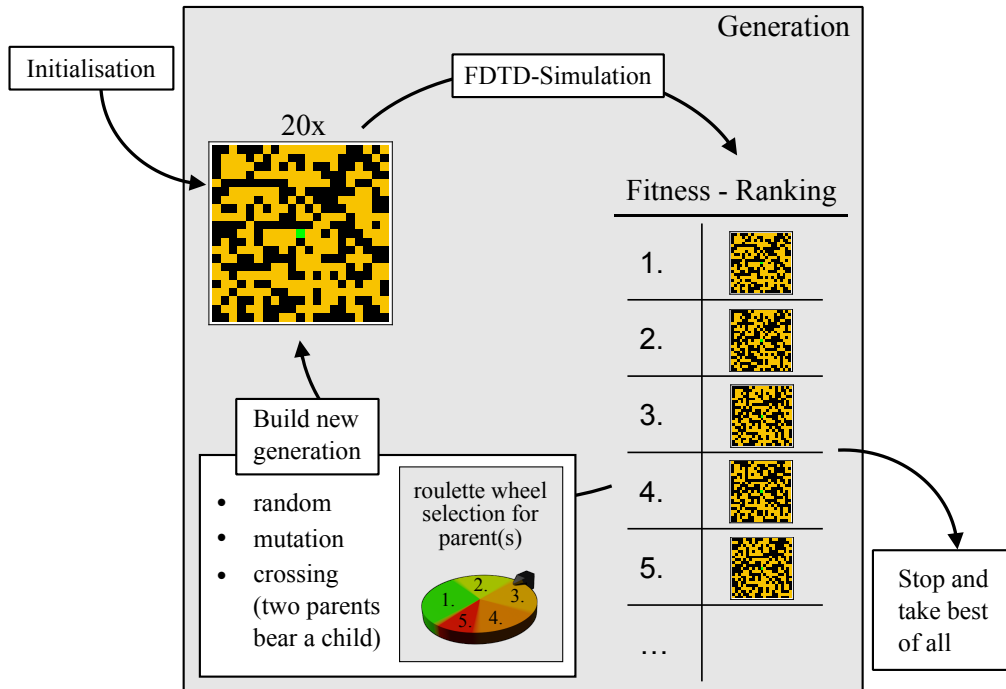


Figure 7.2: Scheme of the evolutionary algorithm. After an initialization step, all individuals of a generation are evaluated by means of FDTD-simulations and ranked by the figure of merit. The best five are then taken to generate the individuals for the next generation (see [102] - Suppl. Material).

The evolutionary algorithm as depicted in Fig. 7.2 is implemented in Mat-
Lab². It is a (5,20/30)-strategy, which means it uses generations consisting
of 20 or 30 individual matrix antennas selecting the five fittest structures as
parents for the next generation.

The very first generation is filled with random individuals, with a filling
factor of 0.7, which delivers faster progress in the evolution in the first few
generations. With carefully chosen mechanisms for crossover and mutation
of the genomes, consecutive generations constantly improve in the sense that
their maximum fitness parameter increases. To create descendants in a first
step one of the fittest five parents is selected by roulette wheel selection with
a probability that is proportional to its fitness (parent A). Three methods are
then applied until a total of 20 (or 30) new individuals have been generated for
the next generation. The three different mechanisms to generate individuals
for generation $n + 1$ after evaluation of generation n are:

²The code is available online [162]

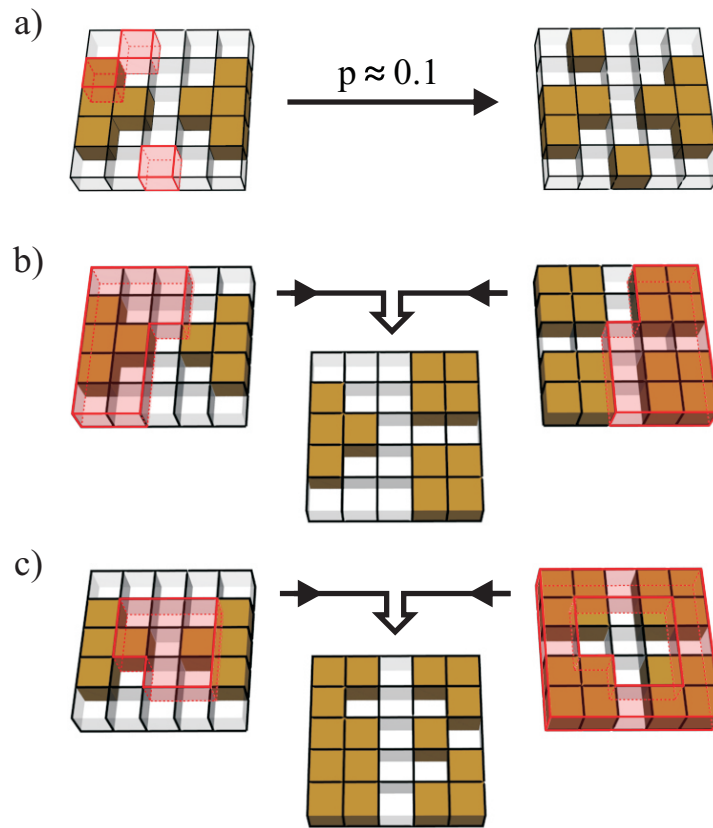


Figure 7.3: Methods used for creating individuals for generation $n + 1$ after generation n has been evaluated. a) Mutation: Each block is eventually toggled with a given probability. b) and c): Crossing of the genomes of two parents which are divided into b) left and right parts (linear crossing) or into c) inner and outer parts (spiral crossing). Not depicted is the generation of complete random new structures ([102] - Suppl. Material).

(i) *Random*: Completely random structures are generated with a 70% chance of each block being gold or void. These structures are independent of the parent pool and intended to introduce diversity into the genetic material.

(ii) *Mutation*: Each block of parent A is toggled between gold and void with a chance of 10% (reddish blocks in Fig. 7.3(a)). This allows good structures to enhance further without intermixing with other genomes.

(iii) *Linear and spiral crossing*: The line-by-line (spiral-) encoded genomes (see Fig. 7.3(b) and (c)) of two parents, A and B , are crossed by combining the first half of the genome of A with the second half of the genome of B preserving

the overall genome length. The point at which the individual genomes are split is chosen randomly. This method allows the combination of the left (inner) part of parent antenna A with the right (outer) part of a second parent B (reddish areas in Fig. 7.3(b) and (c)).

Each method to generate a subsequent individual is applied with equal probability. Method (iii) requires a second parent B that also is chosen from the pool of the remaining four fittest individuals in the same way as A . The new individuals are checked if they or a physically redundant structure already has been simulated and are replaced in that case with newly generated individuals (see appendix A).

To reduce the computational effort, simulations were terminated after 35 fs, when more than 98% of the excitation power has left the simulation volume. Although such a short simulation is not sufficient to reach a very high absolute accuracy, it is still possible to determine the relative hierarchy of simulated antennas in terms of fitness parameters such as near-field intensity. Considering that a full FDTD simulation of an antenna structure generally takes 70 – 80 fs to fully converge, the overall simulation time is cut by about a factor of two. The best individuals after termination on the GA are re-simulated until full convergence in order to obtain physically accurate results.

After a sufficient amount of generations has been simulated, a so called *toggle plot analysis* is performed, which consists of running 21x21 simulations in which every block is toggled individually (see Fig. 7.4). Color-coding the block positions according to the magnitude of the fitness change associated with the individual toggle event shows the relative importance of single blocks, the potential for further improvement of a matrix antenna, and also eventually produces new individuals with enhanced fitness. This is in principle the brute force realization of a hill climber algorithm on the described setup, neglecting pair- and higher-order correlations.

7.2 Results

Only the EA yielding the very best antenna geometry will be presented here. More information about test runs with different parameters and geometries can be found in the master's thesis of Markus Kiunke [125] and Oleg Selig [163].

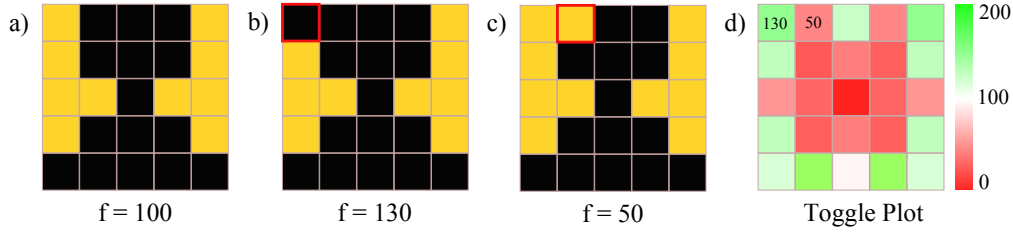


Figure 7.4: Explanation of the toggle plot: a) original antenna structure with a given fitness, defining the 100% level. b) single toggle of a gold block to void, increasing the fitness. c) Toggle of a single void space into a gold block, decreasing the fitness. d) Map of effect of all matrix element toggles, called Toggle Plot (values are fictitious; adapted from [163]).

Figure 7.5 displays the progress of the evolutionary optimization as a function of generation number. Panel a) shows the NFIE in the gap of all 2000 simulated individuals of the first run. It is important to note, that the individuals have only been simulated for 35 fs and therefore their fitness parameter is underestimated typically by 10–20%. The first generation contained 20 random individuals with field enhancements between 0.2 and 43.8. Figure 7.5(b) shows, to the very left, the probability of each matrix space of the best 10 structures of the first generation to be occupied with gold (Gen: 1). The low saturation reflects the randomness of each single matrix position. While the algorithm develops, the NFIE gradually increases and surpasses the enhancement of the reference antenna in generation 42.

The probability plots in Fig. 7.5(b) clearly illustrate the development of structural features: left of the gap a small arm with 40×20 nm size evolves, while on the right side a more triangular structure emerges. On the way to a better structure the individuals in a single generation get more similar within the first 10 generations and show only small differences henceforth. The development of some important features leads to a jump in the maximum fitness of a generation, when they are established the first time. The first such feature is a gap, which ensures the minimal possible distance of charge carriers to the optimization position. Then the areas next to the gap are getting more solid, to establish currents and supply the gap with a larger surface charge density. The first big jump in the fitness originates from the removal of the block directly above the center, opening the gap.

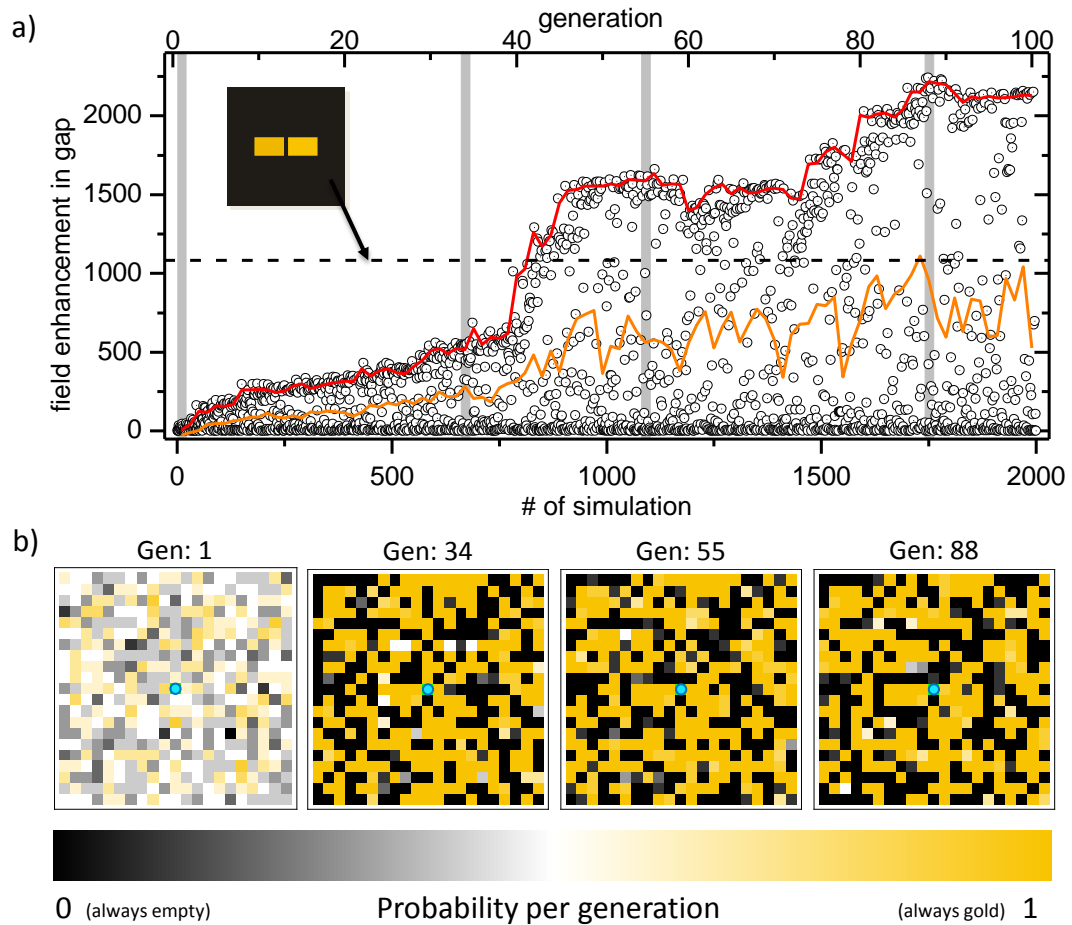


Figure 7.5: Overview over the evolution process. a) shows the development of the NFIE as the number of generations progresses. Twenty simulations make up one generation. Number 1, 34, 55, and 88 are denoted by grey bars for further discussion in b). The red curve shows the maximal obtained enhancement, the orange the mean enhancement of a generation respectively. The black dashed horizontal line marks the field enhancement of the reference dipolar antenna. b) shows the probability of each 21×21 -matrix position for hosting a gold cube for the 10 best structures of the respective generation. The blue spot at the center marks the "gap", where the optimization took place and thus always was set empty.

The fitness also occasionally reduces, which may occur, when a local maximum of the configuration space was found and among the offspring structures there is not yet an individual that includes a new key feature. As crossing will not produce offspring with a novel geometry, more and more individuals will be generated by mutation, thus eventually lowering the fitness in the next generation but also create new features, which will finally lead to the formation of new structural elements that will finally generate even better structures.

In the following we discuss the fittest evolutionary antenna (FEA) obtained by running the EA for 100 generations with 20 individuals each (as shown in Fig. 7.5), a subsequent toggle plot analysis and further 30 generations with 30 individuals each, starting with combinations of the best five structures obtained from the toggle plot analysis.

The excitation wavelength of $\lambda = 650$ nm coincides with the resonance of a linear dipole nanoantenna consisting of two end-to-end aligned $46 \times 30 \times 11$ nm³ gold rods (width = 3 cubes, height = 1 cube) separated by a 10 nm gap (Fig. 7.6(a), top panel) which serves as a reference structure. It exhibits a resonant normalized NFIE of about 1800 in the center of its feed gap. Other geometries, such as bow-tie antennas, were also tested but showed no higher fitness.

The FEA (Fig. 7.6(a), lower panel) exhibits a remarkably high fitness, as indicated by its near-field spectrum in Fig. 7.6(b) which is recorded in the optimization point (indicated as blue dot in (a)) after a broadband excitation. Its maximal NFIE of 3500 is nearly twice as high as that of the reference antenna. Both spectra show single, nearly Lorentzian peaks with Q-factors of $Q=20$ and 23 , respectively.

According to the reciprocity theorem (see chpt. 2.4.3) the FEA should also improve the radiative properties of a quantum emitter positioned in the spot of highest field enhancement. Indeed for the reference antenna we find a radiation enhancement of 2126 and a radiation efficiency of 0.255, while for the FEA the radiation enhancement is 4271 with a radiation efficiency of 0.268.

Surprisingly, the directivity of the FEA remains very similar to that of the reference antenna despite its complex shape as shown in Fig. 7.7. The reference antenna shows a symmetrical dipolar radiation pattern with a directivity (defined in eq. (2.45)) of $D_{\text{ref}} = 2.09$ dBi which is only slightly smaller than

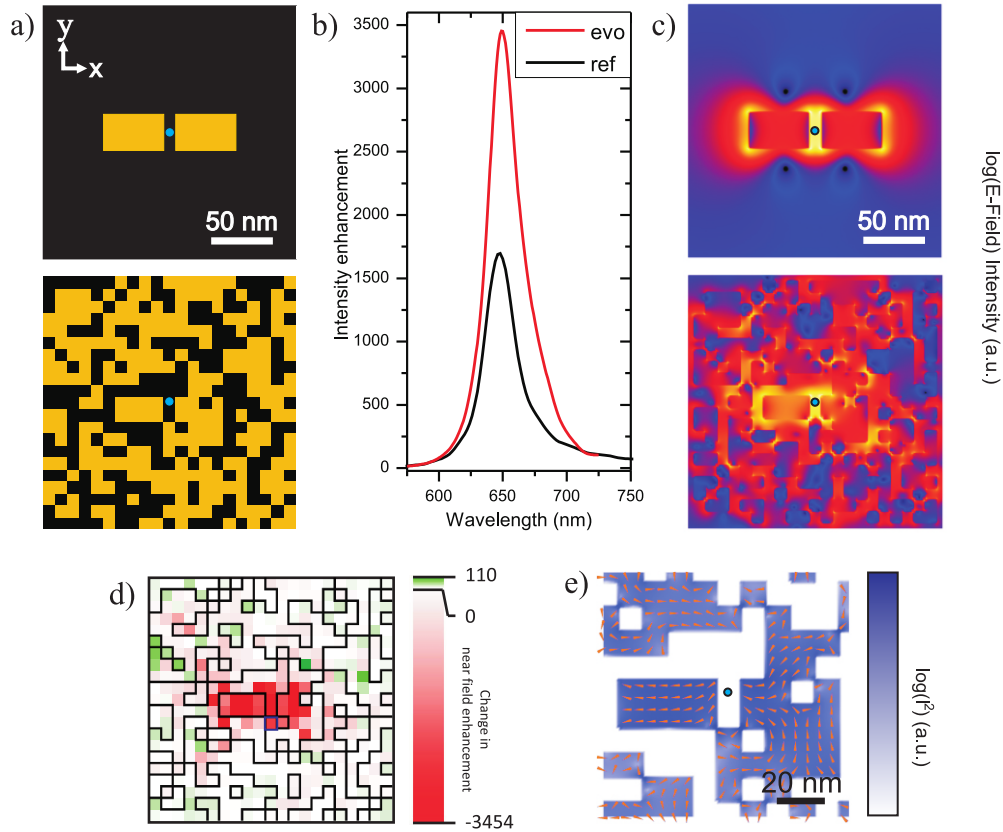


Figure 7.6: Comparison of a resonant linear dipole nanoantenna build from two 10 nm separated rectangular arms of $46 \times 30 \times 11$ nm³ with the FEA obtained from the EA as described in the text. (a) shows the geometry of both structures from the +z direction. The blue spot denotes the position of the near-field optimization by the EA. The spectra in (b) are taken at this marked position during a broadband Gaussian excitation. (c) shows the logarithmic near-field intensities at $\lambda = 647$ nm when the structures are illuminated by a monochromatic Gaussian focus with NA = 1. The scales are normalized and not comparable. In (d) the the change of NFIE at the optimization position is shown for each single block, when it is toggled. (e) is a zoom of the center part of the EA antenna, showing strength and direction of the currents [102].

$D_{\lambda/2} = 2.15$ dBi of an ideal thin wire half wave dipole (compare with Fig. 2.7). The radiation pattern of the FEA deviates only slightly from the reference antennas radiation pattern, yet, it exhibits a more pronounced radiation in z -direction. Considering reciprocity, its enhanced directivity of $D_{\text{EA}} = 2.31$ dBi reflects the optimization to irradiation by a directed gaussian beam. However, the deviation is not large, which is attributed to the FEA being smaller than $\lambda_{\text{res}}/2$. Multipole excitations within these small area are only able to interfere very weakly with each other since the phase differences of the constituting dipoles can not add up to significant values.

The FEA exhibits three noticeable geometrical features:

- (i) a small gap in the center between two compact rod(-like) structures, being slightly displaced in y -direction with respect to the point of optimization.
- (ii) a single gold block directly below the gap which creates a current path connecting the rod-like structures and
- (iii) a seemingly random arrangement of gold blocks further away from the center.

It is important to note that the optimal structure found by the EA depends on both the available primitive elements as well as on possible boundary conditions. Using a different block size or imposing boundary conditions, e.g. limiting the gap width, would lead to different fittest structures.

We now consider the NFIE maps of both reference and FEA in Fig. 7.6(c). The small displacement of the rod-like structures increases the NFIE by a small factor because of the proximity of the corners of the rod-like structures to the point of optimization. However, this alone by far cannot explain the observed increase of the NFIE. The achievable enhancement by displacing the reference antenna in a similar way amounts to a factor of 1.1.

The result of a *toggle plot analysis* is displayed in Fig. 7.6(d). It indicates that changing individual blocks does not yield considerable additional NFIE, but rather a severe reduction. We therefore believe that the structure's fitness is close to a (local) maximum in the configuration space. The by far strongest reduction of fitness occurs when toggling gold blocks near the center. This indicates that the compact structure in the proximity of the gap is dominating the field enhancement and is most critical for achieving the observed performance. Assuming that it is excited at an eigenmode, this also explains the

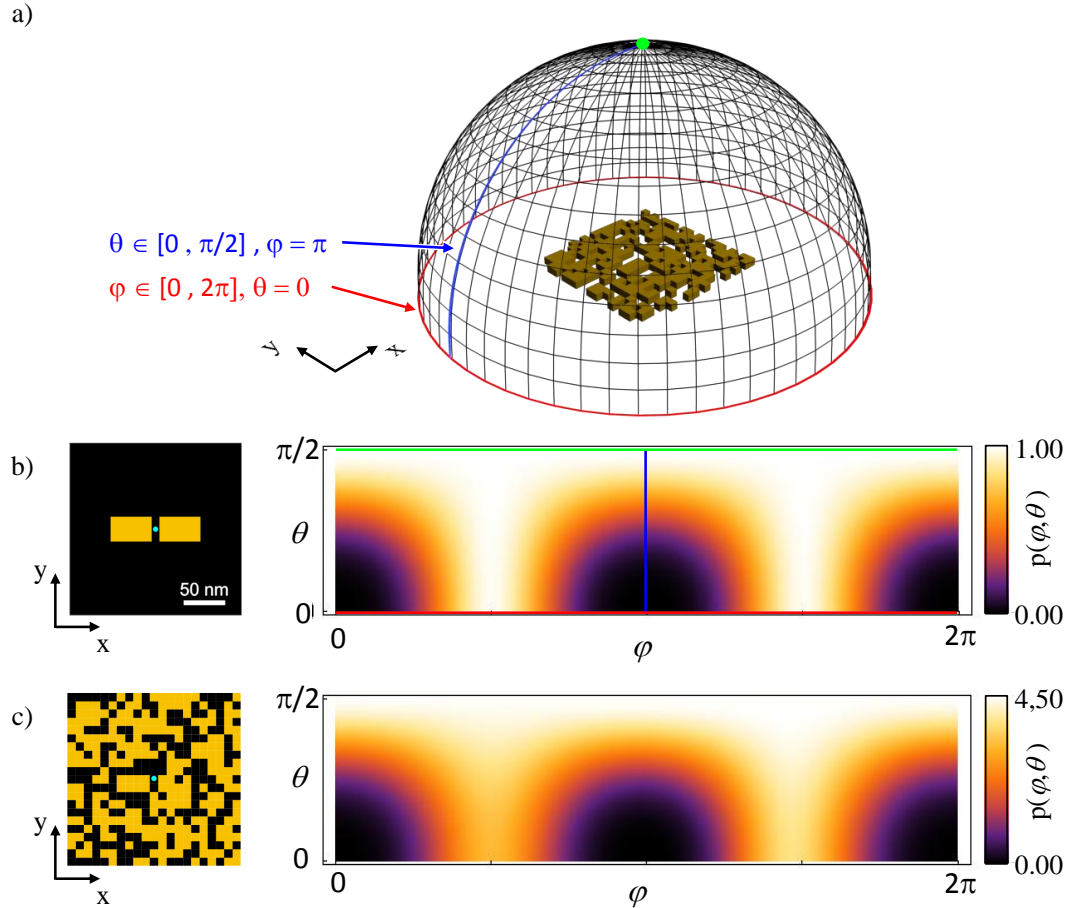


Figure 7.7: Radiation patterns of reference antenna and FEA. a) Definition of spherical coordinates θ and φ with respect to the antenna orientation. A point dipole emitter emitting at the resonance wavelength $\lambda_{\text{res}} = 650$ nm is placed at the position of highest NFIE. Since the structures are symmetrical in z -direction, only the radiation power in the upper half space needs to be evaluated. The colored markings (red, blue, green) denote particular constant-coordinate lines. b) shows geometry and normalized dipolar radiation pattern in cylindrical projection for the reference antenna. c) shows geometry and radiation pattern of the FEA normalized to the reference antenna (compare with Fig. 2.7; [102] - Suppl. Material).

single narrow Lorentzian resonance. As apparent from the toggle plot, the random structures far away from the center do hardly influence the field enhancement in the gap. Nevertheless, it is possible that collective effects of the peripheral blocks do influence the fitness of the structure to some extent which due to the inherent complexity could not be discussed in further detail.

Of particular interest is the single gold block below the gap. It provides a current path via the cube edges between the two rod-like structures that form the gap as can be observed by taking a closer look at the currents in the central part of the FEA in Fig. 7.6(e). Surprisingly, we find that removing this block severely lowers the fitness of the resulting matrix antenna instead of increasing it. Closer inspection reveals two particular current paths, one located in the rod-like structures corresponding to a bonding linear dipolar nanoantenna mode, but also a second one, which flows from one upper gap edge through the connecting gold block to the other upper gap edge, corresponding to a fundamental split ring mode.

7.3 The split-ring antenna

In order to better understand the effects that lead to the increased NFIE, in the following we study a reduced model system, i.e. a mixture of a split-ring and a linear two-wire antenna called *split-ring antenna* (SRA) that retains the important features of the FEA but can be described by a small number of freely tunable parameters. Its geometry is depicted in Fig. 7.8(a). The structure can be interpreted either as linear two-wire antenna with an asymmetric short circuit, a split-ring resonator with attached wires or a long single nanowire that is deformed in a particular way.

For a proof of principle we started with the reference antenna defined by $g = h = 10$ nm and $w = 30$ nm, and linked the two arms with a connection as would be possible within the EA and set $l_c = 30$ nm and $w_c = 10$ nm as depicted in Fig. 7.8(a). The antenna length l had to be re-optimized for resonant behavior at $\lambda = 650$ nm and the resulting antenna had $l_{\text{SRA}} = 108$ nm compared to the original antenna with $l = 102$ nm (see Fig. 7.8(b) and (c)).

The NFIE of the SRA in the center plane is depicted in Fig. 7.8(b), showing a strong field concentration towards the open side of the SRA gap as it was

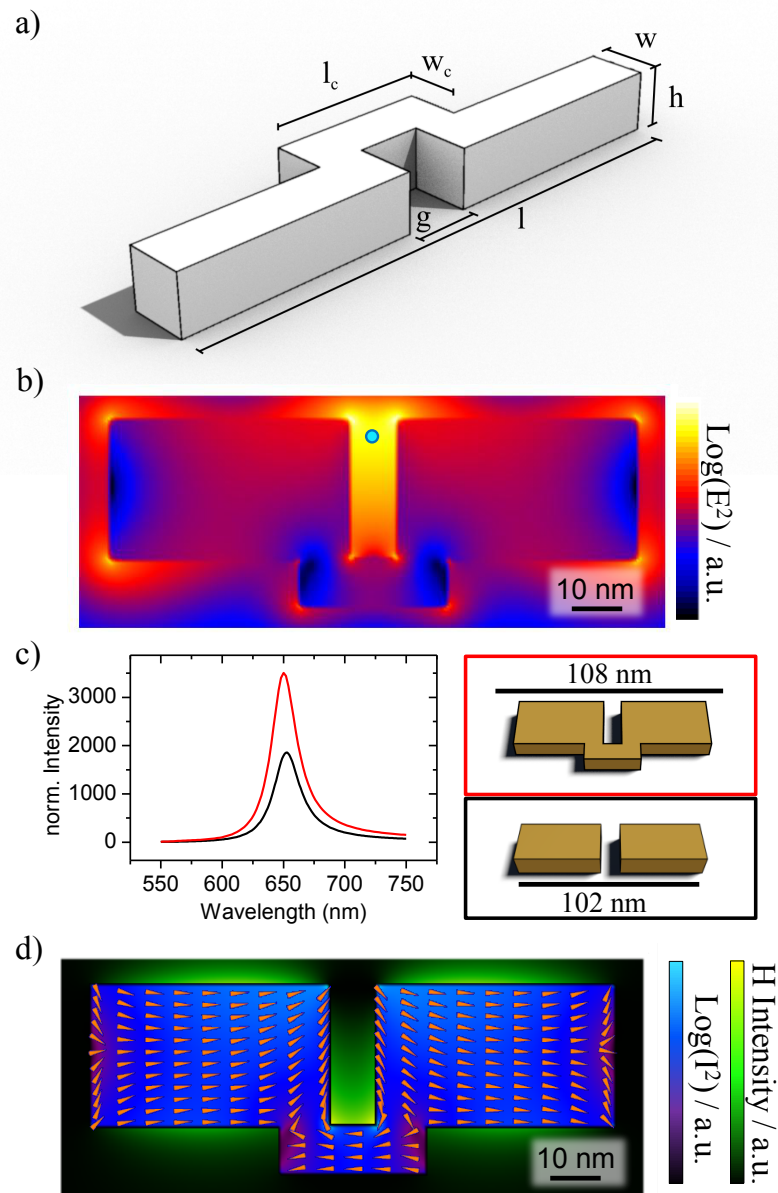


Figure 7.8: The split-ring antenna (SRA). a) General geometry of a split ring antenna. l is the overall length, l_c the length of the conductive connection. w the width of the antenna arms and w_c the width of the connection. h defines the height of the overall structure and g the extension of the center gap. b) Near-field intensity of the SRA as described in the text, showing the very concentrated fields in the open end of the gap. The blue dot denotes the the point of measurement for the spectrum figured in c). The $Q \approx 25$ for the SRA (red) is comparable to the reference antenna (black). d) is an overlay of the current intensities (blue) and direction (arrows) inside the material, as well as the magnetic near-fields (green) outside the structure (b) – d) from [102]).

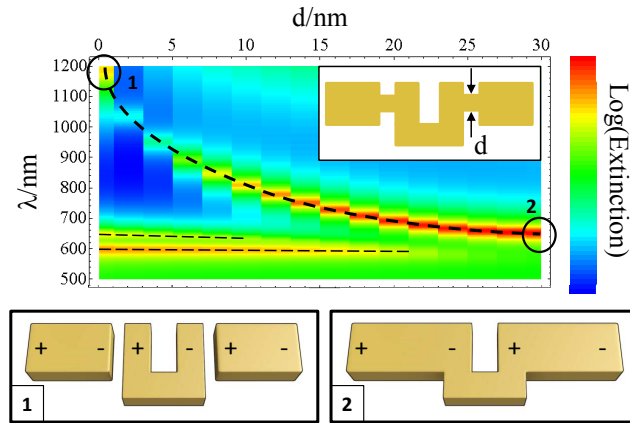


Figure 7.9: Wavelength shift of the extinction cross section resonance for the combined two-wire antenna and the $n = 1$ split ring resonance, as a conductive link between two antenna rods and a split ring (see inset) increases in thickness (marked thick dashed). Also visible are the bonding and anti-bonding $n = 3$ -modes, which also shift slightly into the blue and get very weak (marked thin dashed). The sketches at the bottom show the geometries of the fully disconnected and fully connected structures together with the position and sign of their mode's charge density maxima [102].

already observed in the FEA. Figure 7.8(c) compares the spectra of the resonances of a SRA with a non short-circuited dipolar antenna of identical arm cross section, gap size and resonance frequency. Both spectra were obtained at the point of highest NFIE along the y -axis. Also in the present model system the split-ring antenna surpasses the classical dipole antenna design in terms of maximum NFIE by a factor of 2.

The current pattern of the SRA can be decomposed into a fundamental ($n=1$) split-ring mode (see chpt. 3.2.5) and a dipolar mode current in each antenna arm which is running 180° out-of-phase to the current in the short circuit (Fig. 7.8(d)), adding to the charge accumulation in the upper part of the gap and thus increasing the NFIE. Since the resonance is in the optical regime, the SRA is a way to circumvent the limitation of pure split-ring resonances to wavelengths longer than 900 nm due to kinetic inductance (see chpt. 3.2.5). The SRA represents a magnetic dipole in the visible, showing magnetic fields (Fig. 7.8(d)), which are only by a factor of 2.5 weaker than those of the isolated split-ring resonator at its resonance wavelength of 908 nm.

To confirm the shift of the fundamental split-ring mode from the infrared into the visible spectral range, we place two gold bars ($35 \times 30 \times 11 \text{ nm}^3$) separated by a 5 nm non conductive gap from the plain split-rings ends. The extinction cross section is examined while connecting the gold bars with the split-ring via successively thicker gold bridges at the center of the gap (see Fig. 7.9 and inset). In the unconnected geometry the fundamental split-ring resonance is shifted into the red to about 1200 nm due to the capacitive coupling across the gap (compare with the dipolar antenna in Fig. 3.10(b)). As the connection grows thicker (increasing d), the fundamental split-ring mode is shifted by more than 500 nm from the infrared into the visible. The shift of the resonance is of similar origin as the emergence of a charge transfer mode for a dipolar antenna with a conductive bridge [164]. However, here the fundamental split-ring mode is not disappearing but its phase is inverted (compare the charge distributions sketched in the lower panel of Fig. 7.9). For very thin conductive bridges both modes exist simultaneously (see also [164]) and cancel out each other, leading to a dip in the extinction cross section.

Conclusion By using the method of evolutionary optimization in a large parameter space, high-fitness plasmonic antennas can be found within a reasonable amount of time. Besides directly yielding optimized structures, a careful analysis of the working principles of the resulting geometries may provide new design strategies for high-performance plasmonic nanostructures. In the present example, an increase of the NFIE by nearly a factor of 2 compared to a dipolar antenna design can be obtained, caused by the intriguing cooperation of a fundamental split-ring mode and dipole antenna resonance. This novel antenna design additionally exhibits very large magnetic fields at optical frequencies. In particular, the fundamental split-ring resonance is shifted into the visible spectral range because of the formation of a charge-transfer-like hybrid resonance with two rods of a dipolar antenna. The method can be further adapted to include geometrical constraints imposed by microfabrication and therefore lead to structures that can directly be implemented in practical applications, which will be shown in the next chapter.

Chapter 8

Evolutionary optimization of realistic optical antennas

The results from the previous chapter proofed evolutionary optimization of optical antennas with a two dimensional binary matrix as genome to be feasible as well as instructive. Yet it is purely simulation work and the resulting geometries are unlikely to be realized in experiment.

This chapter presents the results of the next logical step, improving and adapting the evolutionary algorithm (EA) to realistic structure dimensions and rounded geometric features. For this the capabilities of high-detail focused ion beam (FIB; see section 5.2) fabrication using monocrystalline gold-flakes as substrates (see section 5.3) are evaluated. Then the EA is adapted to the minimal reproducible dimensions without changing the optimization goal, to maximize the near-field intensity enhancement (NFIE) at a single point in space. The fittest evolutionary antenna is investigated for its working principle, as its shape again is not comparable to any known radio-frequency antenna design. Afterwards, the resulting geometries are fabricated directly from the genomes, which are translated into FIB milling commands by a 'printer driver' MatLab script¹. An experimental study by means of two-photon-photo-luminescence confocal microscopy successfully reproduces the numerical results².

¹All the mentioned code can be accessed online [165]

²This work was published in very similar form here: [166]

8.1 Algorithm adaption

Figure 8.1 illustrates the encoding and geometrical interpretation of the planar antenna structures used to adapt the EA to realistic geometries. Antennas are assumed to consist of 30 nm thick gold on top of 200 nm indium tin oxide (ITO) on top of a glass substrate, corresponding to later experimental conditions. The high transparency and the good conductivity of the substrate are ideal for ion beam milling, SEM imaging, as well as optical characterization. The genome is a two dimensional square matrix with binary entries (see Fig. 8.1(b)). Each '1' denotes a cylindrical hole which approximates the structural primitive of FIB fabrication. As the antenna center is meant to be the area of maximum NFIE, the matrix center is always set to '1'. Figure 8.1(c) illustrates, how the topology of possible hole arrangements is converted to a realistic geometry that can be fabricated by FIB milling: adjacent holes are connected, leading to geometries as the one sketched in Fig. 8.1(d).

To identify the minimal parameters for the hole radius r_h and center-to-center hole distance d_h resulting in reproducible patterns when FIB milling a 30 nm thick single crystalline gold flake (see chpt. 5.3), an 11×11 matrix test pattern (see Fig. 8.2(a)) was developed. It includes all relevant structural primitives, such as e.g. isolated gold islands, individual missing pixels (holes) as well as solid gold rims and corners. Figure 8.2(b) shows an SEM picture of the structure with the final dimensions with holes of radius $r_h = 11$ nm and a center-to-center distance of $d_h = 30$ nm.

The evolutionary algorithm was run using also an 11×11 square array with the determined dimensions. In the simulations the antenna is excited using a Gaussian focus ($\text{NA} = 1.4$; $\lambda_{\text{exc}} = 830$ nm) at normal incidence, centered onto the structure. The resulting overall antenna area of 330 nm \times 330 nm fits the FWHM of the Gaussian focus of ≈ 390 nm. (comparable to the situation in Fig. 7.1(d)).

Contrary to chapter 7 the realistic EA was performed without the addition of random structures each generation, since they have no benefit in late generations. We proved, that the algorithm is still capable of leaving local maxima (see appendix B). Each new individual is generated via mutation with a probability of 0.4 or crossing with a probability of 0.6. Mutation happens by

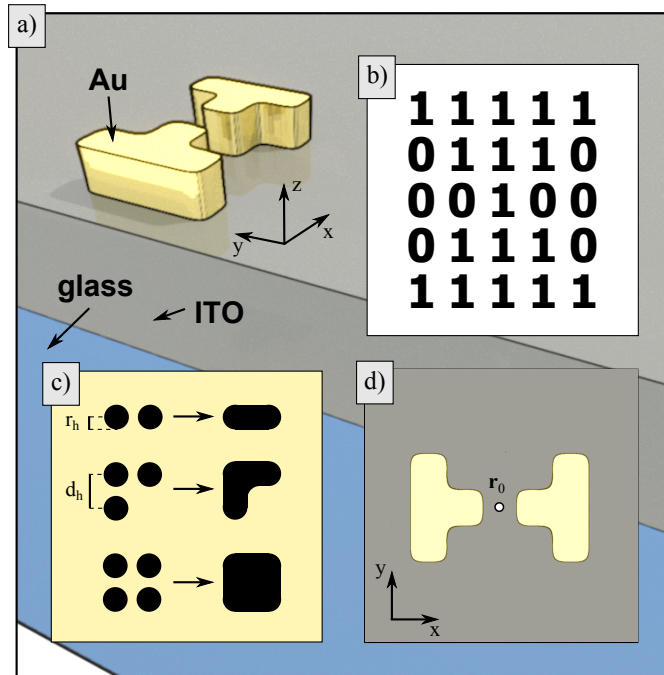


Figure 8.1: Genome and topological constraints. a) 3D sketch of an exemplary geometry on top of an ITO layer covering a glass substrate. The rounded features emulate constraints due to FIB milling. b) binary 5×5 genome of a small optical bow-tie-like antenna, where '1' denotes the positions at which the gold will be removed. c) Rules for replacing neighboring hole arrangements by structures that can be fabricated by FIB. r_h : hole radius, d_h : center-to-center hole distance. d) top view of the structure resulting from the genome in b) after applying the rules sketched in c). r_0 denotes the point of optimization for the NFIE.

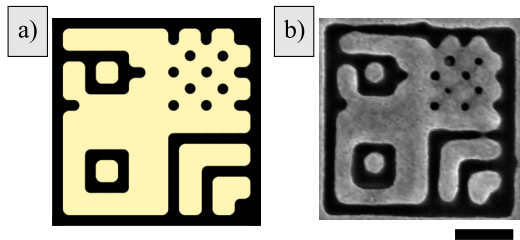


Figure 8.2: 11×11 test pattern design for FIB benchmarking. a) Sketch of geometry. b) SEM picture of the resulting structure produced by FIB milling in 30 nm thick monocrystalline gold (scale bar = 100 nm).

switching each bit of the binary genome with a probability $p_{fl} = 0.01$, resulting in an average of $\sum_{i=0}^n p_{fl}(1 - p_{fl})^i = 0.7$ flips for $n = 120$ matrix elements ($11^2 - 1$; center spot is always free). We increased the amount of individuals to 30 per generation and took the 8 fittest structures as parents for building subsequent generations. The first generation again consisted of random structures with a filling factor of 0.7.

8.2 Result of evolution

As in the previous chapter, only the EA yielding the very best antenna geometry – called fittest evolutionary antenna (FEA) – will be presented here. More information about test runs with different parameters and geometries can be found in the Masters thesis of Oleg Selig [163].

The evolution (see Fig. 8.3) started favorable with a single individual in the first random generation with a fitness of over 300, being most likely the parent of all subsequent generations due to the implemented roulette wheel mechanism (see section 7.1). After a phase of rapid progress around generation 15 the fitness gain per generation seems to decrease exponentially towards a final value, which is, why we decided to stop the EA after generation 58. Another reason was our experience from the theoretical algorithm, that the center part of the antenna responsible for the near-field concentration will not change any more in later generations.

The FEA is a compact asymmetric structure with a high filling factor of 65 % with an L-shaped gap in the very center (see lower part of Fig. 8.4(a)). We compare its fitness to a dipolar antenna with corresponding geometrical

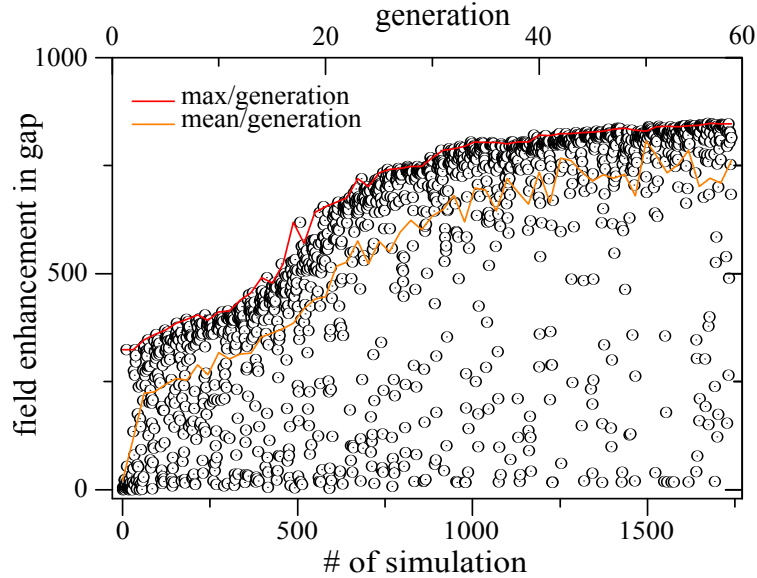


Figure 8.3: Development of the realistic EA. Each dot represents the fitness parameter of a single individual. Also the best fitness per generation (red) as well as the mean fitness per generation (orange) are shown.

constrains (depicted in Fig. 8.4(a), top), its arm dimensions being $112 \times 38 \times 30 \text{ nm}^3$ with a gap of 22 nm optimized via its arm length to exhibit a NFIE in the gap at $\lambda = 830 \text{ nm}$.

The NFIE spectra of both antennas show a Lorentzian-shaped resonance with a maximum of 1100 at $\lambda_{\text{FEA}} = 832 \text{ nm}$ for the FEA and of 640 at $\lambda_{\text{res}} = 835 \text{ nm}$ for the reference antenna (see Fig. 8.4(b)) with a full width at half maximum of $\Delta\lambda_{\text{FEA}} = 74 \text{ nm}$ compared to $\Delta\lambda_{\text{ref}} = 105 \text{ nm}$. This corresponds to a Q-factor $Q_{\text{FEA}} = \lambda_{\text{FEA}}/\Delta\lambda_{\text{FEA}} = 11.2$ for the FEA and $Q_{\text{ref}} = \lambda_{\text{ref}}/\Delta\lambda_{\text{ref}} = 8.0$ for the reference antenna, respectively. As a higher Q-factor originates from lower combined radiative and Ohmic losses (see chpt. 2.4), the far-field coupling of the FEA is reduced in comparison to the reference antenna. Nevertheless, the FEA exhibits an 1.7-fold higher NFIE in the antenna center, which further highlights its improved energy concentration mechanism.

The asymmetry of the FEA geometry originates from the still too coarse discretization provided by the antennas primitive elements: changing antenna dimensions in steps of 30 nm results in large shifts of resonance frequency making it difficult to perfectly match the optimization frequency with a symmetric geometry. The importance of individual FEA building blocks for the

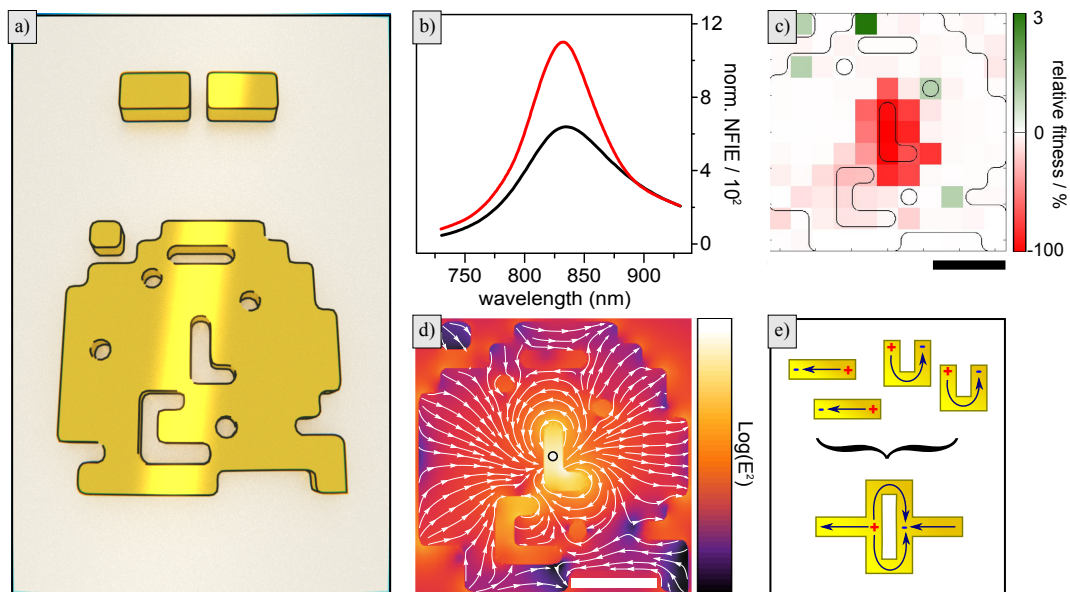


Figure 8.4: Properties of the fittest evolutionary antenna (FEA): a) 3D sketch of the reference dipolar antenna (top) and the FEA (bottom) on substrate. b) Near-field intensity enhancement (NFIE) spectrum at the very center of the reference antenna (black) and the FEA (red). c) Toggle plot of FEA (for details see text). d) NFIE and current direction (white arrows) in the center plane of the FEA. e) Model for the operation principle of the FEA constructively combining current patterns from two split-ring resonators and two rod antennas. All scale bars are 100 nm.

obtained NFIE can be assessed using a toggle plot (Fig. 8.4(c); explained in chpt. 7.1). It clearly demonstrates that the pixels close to the center play the most important role for the antenna performance. Some green areas indicate that the FEA structure does not correspond to the absolute global maximum in the configuration space of the EA and a slight increase of NFIE up to 3 % can be achieved by switching single elements in the periphery.

To understand the working principle of the FEA we analyze the NFIE distribution (color coded in Fig. 8.4(d)) and a temporal snapshot of the current pattern (white lines and arrows). The near-field intensity at the optimization point (marked with circle) yields a 1100-fold normalized enhancement which is nearly fully x -polarized. The current pattern suggests an accumulation of charges at positions close to the optimization point within the antenna even in the absence of tip-like structures. Only the kink of the L-shaped central void contributes to the enhancement by means of the lightning rod effect.

The FEA current pattern can be described by a constructive superposition of two fundamental modes (see Fig. 8.4(e)): (i) dipolar antenna currents comparable to the lowest order bonding-mode current pattern of linear two-wire antennas (compare to Fig. 3.10(b)) with the well-known benefits of good far-field coupling as well as accumulation of opposite charges at either side of the gap as well as; (ii) the current pattern of fundamental split-ring like modes (see chpt. 3.2.5) above and below the gap, leading to additional charge accumulations at the center and resulting in a larger NFIE as for a plain dipolar antenna. This is the logical extension of the split-ring antenna concept from chpt. 7.3.

8.3 Experiment

The generation of the FIB pattern from the binary matrix involves a specialized algorithm [165] written in MatLab, which transforms the '1' entries into polygons. These are connected like the structures in the simulations, but with all rectangular edges. The round shapes are created automatically by the limited resolution of the ion beam. Finally all polygons, still with scales discretized by the $30 \times 30 \text{ nm}^2$ grid, are decreased in extension by 3 nm. This yields after fabrication the dimensions as simulated representing a "printer driver" for the

FIB machine. Special care had to be taken for single holes, as the machine-intern milling algorithm results in smaller or even incompletely milled holes for the optimized settings of the bigger polygons. We automatically adjusted the milling depth for single holes by a factor of 1.4, which was determined by empirical tests. This pattern was written four times, each pass with a different direction (top to bottom, left to right, ...) to ensure the milled features being regularly shaped. Milling in only one direction leads to undesired redeposition effects.

The FEA as well as five antenna structures from earlier generations with a decreasing fitness were fabricated using the 'printer driver' (see Fig. 8.5(a)). To evaluate the reproducibility, each structure was fabricated six to eight times in a row, the first row denoted #1 containing the FEA. The thickness of the structures after FIB milling has been measured by AFM to be 28 ± 2 nm, closely matching the intended 30 nm. To account for the small deviation in thickness all geometries were re-simulated with decreased thickness of 28 nm resulting in a slightly reduced fitness for all geometries, while preserving the hierarchy of relative fitness, except for a slight increase for structure #5 (see appendix C).

Two-photon-photo-luminescence (TPPL) is used to experimentally probe the relative change of near-field intensity enhancement of the fabricated antenna structures (see chpt. 6.1). In good approximation the intensity I_{TPPL} of the TPPL signal is proportional to the integral of the forth power of the electrical field \mathbf{E} within the volume of the antenna V_{ant} :

$$I_{\text{TPPL}} \propto \int_V \mathbf{E}^4 dV_{\text{ant}} \quad . \quad (8.1)$$

Equation (8.1) allows to numerically calculate the relative changes of emitted TPPL signal based on simulated antenna modes.

The vast majority of the signal originates from the volume near the antenna hot spots, where the field gradients are largest. The fabricated EA antennas show nearly identical geometries around the central hot spot. They can therefore be compared reliably by means of TPPL, which provides a measure for the relative NFIE, assuming $I_{\text{TPPL}} \propto I_x^2(\mathbf{r}_0)$. The gap of the reference antenna strongly deviates in shape from the EA antennas and their TPPL signals cannot be compared quantitatively.

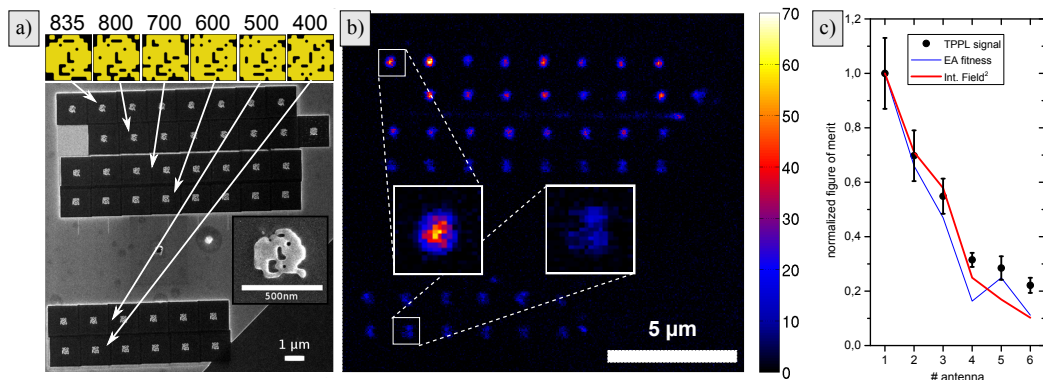


Figure 8.5: Experimental realization of evolutionary antennas: a) Fitness, sketches and SEM image of the EA antenna array realized by means of FIB milling. Each row contains eight times the similar structure sorted by fitness from top to bottom. b) TPPL map of the fabricated array. The insets show detailed maps of one of the very best and of the worst antenna geometry. c) evaluation of the TPPL data (black dots) together with simulated values for the fitness (NFIE - red line) and the simulated TPPL value (integrated forth power of the electric field inside the metal - blue line).

TPPL of the fabricated antennas is recorded by scanning confocal microscopy using a 300 fs Ti:Saph laser at a center wavelength of 830 nm (see chapter 6). Figure 8.5(b) shows the resulting TPPL map. The antennas are clearly distinguishable and the trend of decreasing signal for antennas with lower fitness is obvious.

Figure 8.5(c) shows the comparison between experimental and numerical results. The experimental data points are acquired by integrating the TPPL count rates over the area of the individual antennas. Mean value and standard deviation are calculated and normalized to the value of the FEA. As numerical results both the fitness parameter as well as the simulated TPPL signal (equation (8.1)) for 28 nm thick antennas are plotted, each also normalized to the respective value of the FEA. There is good agreement for the relative changes of measured TPPL signal, simulated fitness and simulated TPPL signal. The trend of increasing error bars with increasing fitness can be explained by the influence of different hole sizes due to fabrication inaccuracies. The NFIE of the antennas depends heavily on the central area geometry due to the capacitive coupling across the width of the center gap (see appendix C).

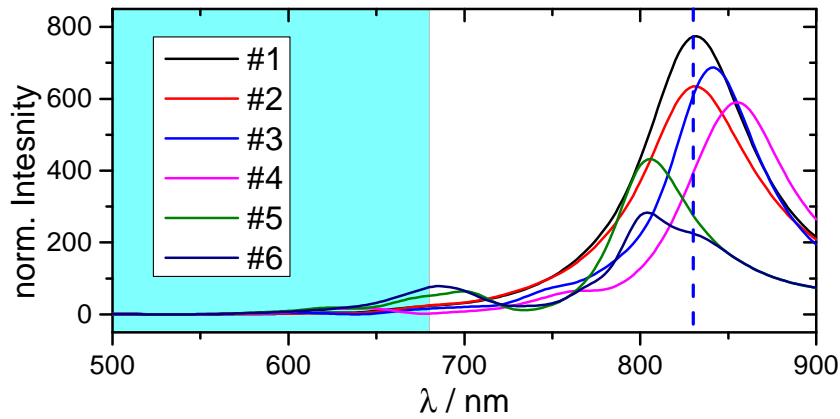


Figure 8.6: Near-field spectra of the evolutionary antennas in the point of optimization. The dark blue dashed line denotes the excitation wavelength of 830 nm, while the light blue area shows the wavelengths contributing to the TPPL signal in the experiment.

For the two antennas with lowest fitness the measured normalized count rates are consistently higher than the simulated relative signal strengths. This may be due to different effects: i) the simulated broadband spectra (see Fig. 8.6) show an additional small resonance peak at about $\lambda = 670$ nm for those two geometries, which will lead to an enhancement of the TPPL signal compared to the other antennas [167]. ii) antennas #5 and #6 do not show a single central peak in the TPPL map. This most probably originates in the existence of multiple or higher order modes, not included in the simulations with the excitation focus being fixed in the very center of their geometries. Both effects were not considered.

Conclusion In the end an evolutionary algorithm describing realistic planar optical antenna geometries was realized with feature sizes of ≈ 22 nm that can be directly printed via FIB milling. The fittest antenna resulting from an optimization of near field intensity enhancement is a rather compact, yet complex geometry which exhibits a surprisingly clean Lorentian resonance. The responsible mode can be described by a superposition of a dipolar antenna resonance and split ring resonances. Comparison of experimental two-photon photo luminescence data and corresponding numerical simulations show good agreement and prove the possibility to establish a direct link between evo-

lutionary optimization and fabrication of optimized structures which indeed display the expected high performance.

In the next chapter a novel theoretical framework will be developed that explains the outstanding functionality of the antenna mode of the FEA on a more fundamental level.

Chapter 9

Modematching for optical antennas

In this chapter Poynting's theorem is combined with reciprocity to derive a novel description of quantum emitter (QE) emission enhancement mediated by a focusing optical antenna (FOA) that is similar to mode matching [54,168]. Its validity is proven analytically at the case of a point dipole in front of a sphere. By introducing a second mode-matching condition for the coupling of the FOA to the far-field two optimal FOA mode patterns are identified. This allows to re-asses the functionality of plasmonic structures resulting from the previous two chapters. Furthermore, from one of the optimal mode patterns a plasmonic cavity antenna (PCA) geometry is devised and numerically investigated. The presented PCA design is not fully optimized, but as similar as possible to an established dipolar two-wire antenna geometry, which it surpasses clearly¹.

9.1 Theory

We consider a classical point dipole p with a dipolar moment \mathbf{p} , emitting photons at frequency ω , which is situated at \mathbf{r}_p . The dipole represents a QE without intrinsic losses whose emission rate depends on $\rho(\mathbf{r}_p, \omega)$, the partial LDOS at the QE position \mathbf{r}_p parallel to its dipole moment \mathbf{p} (compare with

¹This chapter is very similar to a paper that was in preparation at the time the thesis was handed in and can now be found here: [169].

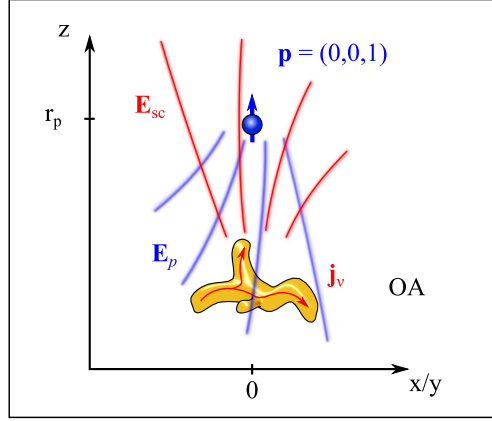


Figure 9.1: (color online) General setup of a dipole \mathbf{p} situated at $\mathbf{r}_p = (0, 0, r_p)$ with an oscillating dipole moment \mathbf{p} being the source of electromagnetic fields \mathbf{E}_p . In its environment a metallic nanoparticle is situated with a single excitable mode ν leading to scattered fields $\mathbf{E}_{d/\nu}$ originating from source currents $\mathbf{j}_{d/\nu}$.

chpt. 2.3.2):

$$\gamma = \frac{\pi\omega^2}{12\varepsilon_0} |\mathbf{p}|^2 \rho(\mathbf{r}_p, \omega) \quad (9.1)$$

, with ε_0 being the dielectric constant of vacuum. Classically the emitted power P of a dipole in arbitrary environment depends on the Green's tensor $\bar{\mathbf{G}}$ of the system as introduced in eq. (2.16). The enhancement of QE emission power in an inhomogeneous environment can be calculated based on Poynting's theorem as already introduced in eq. (2.27):

$$\frac{\gamma}{\gamma_0} = \frac{P}{P_0} = 1 + \frac{6\pi\varepsilon_0}{|\mathbf{p}|^2} \frac{1}{k^3} \text{Im} \{ \mathbf{E}_{sc}(\mathbf{r}_p) \cdot \mathbf{p}^* \} . \quad (9.2)$$

, with

$$\text{Im} \{ \mathbf{E}_{sc}(\mathbf{r}_p) \cdot \mathbf{p}^* \} = |\mathbf{E}_{sc}(\mathbf{r}_p) \cdot \mathbf{p}| \text{Im} \{ e^{i\Delta\phi} \} . \quad (9.3)$$

Here k is the wave vector, \mathbf{E}_{sc} the field scattered by the environment and $\Delta\phi = \phi_{sc} - \phi_p$ the phase between dipolar moment and scattered field.

We take a closer look on a radiating dipole positioned on the z -axis at $\mathbf{r}_p = (0, 0, r_p)$ with a dipolar moment of $\mathbf{p} = (0, 0, 1)$ defining the current $\mathbf{j}_p(\mathbf{r}) = -i\omega\mathbf{p}\delta(\mathbf{r} - \mathbf{r}_p)$ in close proximity to a FOA with $k \cdot r_p \ll 1$, as shown in Fig. 9.1. The FOA is a single metallic nano particle or a collection of these with its center of mass in the coordinate origin. It shows a set of linearly independent plasmonic eigenmodes at the emission wavelength of the QE. In the following we assume without loss of generality the MNP showing a single

mode ν which can be excited at ω . The scattered field in equation (9.3) can then be expressed as:

$$\mathbf{E}_{\text{sc}}(\mathbf{r}_p) = i\omega\mu_0 \int_{V_\nu} \bar{\mathbf{G}}_0(\mathbf{r}_p, \mathbf{r}') \mathbf{j}_\nu(\mathbf{r}') d^3r' \quad (9.4)$$

, where $\bar{\mathbf{G}}_0(\mathbf{r}_p, \mathbf{r}')$ is the Green's tensor for a point dipole at position \mathbf{r}' acting on position \mathbf{r}_p , and \mathbf{j}_ν is the mode current being the source of the scattered field.

For a FOA made from a local, dispersive and lossy material like gold, which is described by the dielectric function $\varepsilon(\omega)$, the reciprocity theorem eq. (2.53) implies a symmetry of the Green's tensor:

$$\bar{\mathbf{G}}(\mathbf{r}_p, \mathbf{r}') = \bar{\mathbf{G}}(\mathbf{r}', \mathbf{r}_p) \quad . \quad (9.5)$$

Inserted into eq. (9.4) the scattered fields at \mathbf{r}_0 now depend on the Green's function of the emitting dipole at \mathbf{r}_p evaluated inside the FOA:

$$\mathbf{E}_{\text{sc}}(\mathbf{r}_p) = i\omega\mu_0 \int_{V_\nu} \bar{\mathbf{G}}_0(\mathbf{r}', \mathbf{r}_p) \mathbf{j}_\nu(\mathbf{r}') d^3r' \quad (9.6)$$

Exciting the FOA at resonance in a quasistatic system leads to $\Delta\phi = \pi/2$ everywhere and thus to $\text{Im}\{e^{i\Delta\phi}\} = 1$. Entering this and eq. (9.6) into a slightly rearranged eq. (9.3) leads to:

$$\frac{\gamma}{\gamma_0} = \frac{P}{P_0} = 1 + \frac{6\pi\varepsilon_0}{|\mathbf{p}|^2} \frac{1}{k^3} \cdot \omega\mu_0 \int_{V_\nu} |\bar{\mathbf{G}}_0(\mathbf{r}', \mathbf{r}_p) \mathbf{p} \mathbf{j}_\nu(\mathbf{r}')| d^3r'(\mathbf{r}_p) \quad (9.7)$$

Using $\mathbf{E}_p(\mathbf{r}) = \omega^2\mu_0 \bar{\mathbf{G}}(\mathbf{r}, \mathbf{r}_p) \cdot \mathbf{p}$ the main result of this paper is derived:

$$\frac{P_{\text{tot}}}{P_0} = 1 + \frac{6\pi c\varepsilon_0}{k^4} \int_{V_\nu} |\mathbf{E}_p(\mathbf{r}') \cdot \mathbf{j}_\nu(\mathbf{r}')| d^3r' \quad (9.8)$$

, with c the speed of light in vacuum.

9.2 Dipole in front of sphere

To prove the derived formalism we look at the analytically solvable case of a dipole in front of a sphere with radius R , which was treated already in section 3.2.4. A generalized term for the emission power enhancement for small spheres based on their polarizability is derived in [170], which we will reproduce here.

We start with rewriting the mode current in terms of the OA mode fields:

$$\mathbf{j}_\nu = i\omega\varepsilon_0(\varepsilon(\omega) - 1)\mathbf{E}_\nu \quad (9.9)$$

leading to

$$\frac{P}{P_0} = 1 + \frac{6\pi\varepsilon_0^2}{k^3} \cdot \text{Im} \left\{ (\varepsilon(\omega) - 1) \int_{V_\nu} |\mathbf{E}_p(\mathbf{r}') \cdot \mathbf{E}_\nu(\mathbf{r}')| d^3r' \right\}. \quad (9.10)$$

The dipolar fields inside the sphere volume are:

$$\mathbf{E}_p(\mathbf{r}, \omega) = \sum_\nu D_\nu [p_\nu \mathbf{M}_\nu^{(1)}(k\mathbf{r}) + q_\nu \mathbf{N}_\nu^{(1)}(k\mathbf{r})] \quad (9.11)$$

$\mathbf{M}_\nu^{(1)}$ and $\mathbf{N}_\nu^{(1)}$ are the spherical vector wave functions, as defined in chapter 3.2.4 for a given set of control variables $\nu = n, m, \sigma$ with $n \in \mathbb{N}, m \leq n \in \mathbb{N}$ and $\sigma = \text{odd or even}$, $D_\nu = \xi[(2n+1)(n-m)!]/[4n(n+1)(n+m)!]$ with $\xi = 1$ if $m = 0$ or $\xi = 2$ if $m > 0$, and

$$p_\nu = \frac{ik^3}{\varepsilon_0\pi} \mathbf{M}_\nu^{(3)}(k\mathbf{r}_0) \cdot \mathbf{p} \quad (9.12)$$

$$q_\nu = \frac{ik^3}{\varepsilon_0\pi} \mathbf{N}_\nu^{(3)}(k\mathbf{r}_0) \cdot \mathbf{p} \quad (9.13)$$

being prefactors originating from the Greens tensor as given in [171].

The sphere mode fields are²:

$$\mathbf{E}_{\text{sph}}(\mathbf{r}) = \sum_\nu D_\nu [f_\nu \mathbf{M}_\nu^{(1)}(k_1\mathbf{r}) + g_\nu \mathbf{N}_\nu^{(1)}(k_1\mathbf{r})] \quad (9.14)$$

, with $k_1 = k \cdot \sqrt{\varepsilon(\omega)}$, and the factors

$$f_\nu = \alpha_n p_\nu \quad ; \quad g_\nu = \beta_n q_\nu \quad (9.15)$$

, where α_n and β_n are complex valued Mie-like coefficients which are derived from the boundary conditions for electric fields at the sphere surface [106].

For spheres with vanishing radius and small distances $R \ll r_p \ll \lambda$ we can restrict our calculation to the emission power enhancement due to the fundamental dipolar sphere mode $\mathbf{N}_{1,0,\text{odd}}^{(1)} = \mathbf{N}_p$ leading to:

$$\int_{V_{\text{sph}}} \mathbf{E}_p \cdot \mathbf{E}_\nu dV = \int_{V_{\text{sph}}} (D_1 q_{1,0,\text{odd}} \mathbf{N}_p(k\mathbf{r})) \cdot (D_1 \beta q_{1,0,\text{odd}} \mathbf{N}_p(k_1\mathbf{r})) dV. \quad (9.16)$$

²Ruppın [106] missed the prefactor D_ν , which is correctly included in the work of Kerker [171]

Here we made use of the fact that the spherical vector wave functions are eigenfunctions of a Hilbert space with

$$\int_{V_{\text{sph}}} A_\nu \cdot B_\mu^* dV = 0 \quad (9.17)$$

for $A, B \in \mathbf{N}^{(1)}, \mathbf{M}^{(1)}$ with $A \neq B$ and arbitrary ν, μ .

In the limit of small spheres the terms of the integral can be developed into series of kR and kr_p respectively, which leads with h_1 being the Hankel function of the first kind to the following intermediate results:

$$q_1 = \frac{ik^3}{\pi\varepsilon_0} \frac{2}{kr_p} \cdot h_1(kr_p) \quad (9.18)$$

$$\text{with } h_1(kr_p) = e^{ikr_p} \left(\frac{1}{kr_p} - \frac{i}{(kr_p)^2} \right) \quad (9.19)$$

$$\beta = \frac{3}{\varepsilon(\omega) + 2} + \mathcal{O}(k^2 R^2) \quad (9.20)$$

$$\int_{V_{\text{sph}}} \mathbf{N}_p(k\mathbf{r}') \cdot \mathbf{N}_p(k_1\mathbf{r}') d^3r' = \frac{16}{27}\pi R^3 + \mathcal{O}(R^5) \quad (9.21)$$

Putting the integral together with $D_1 = 3/8$ and inserting it into eq. (9.10) leads to the final result:

$$\frac{P}{P_0} = 1 + \frac{3k^3}{2\pi} \cdot \text{Im} \left\{ \alpha_0(\omega) e^{2ikr_p} \left[\frac{1}{(kr_p)^4} - \frac{2i}{(kr_p)^5} - \frac{1}{(kr_p)^6} \right] \right\} \quad (9.22)$$

, which is identical to the result in [170], yet with $\alpha_0 = 4\pi R^3(\varepsilon(\omega) - 1)/(\varepsilon(\omega) + 2)$ being the quasi-static polarizability of a small sphere. Taking more terms of β into account the same result can be derived for the effective polarizability including also radiative losses [172].

9.3 Revisiting the split-ring-antenna

In chapter 7 an antenna type called split-ring-antenna (SRA; sketched in Fig. 9.2a) was introduced. It has been shown that it outperforms a comparable two-wire dipolar nano antenna, reasoned by the additional current from the shortcut across the antenna gap enabling a split-ring like mode, which adds up constructively with the dipolar antenna currents for charge accumulation at the gap. With the mode matching formalism we now can understand, that

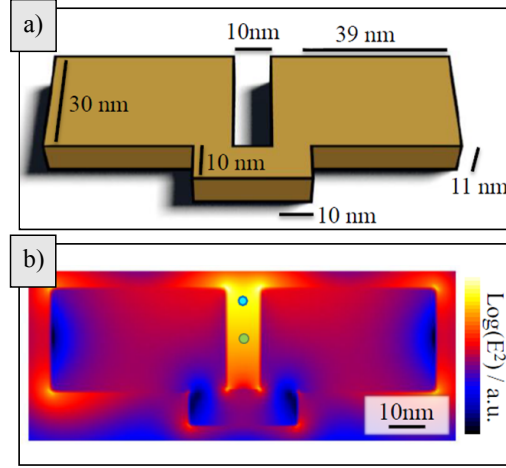


Figure 9.2: Evaluation of a split-ring antenna (SRA) via the mode-matching method. a) geometry of SRA as introduced in [102]. b) Near-field intensity distribution in the center x - y -plane. The green and blue dot represent the center of the antenna and the position of highest fields along the y -axis, respectively (adapted from [102]; more information in text).

the short cut adds a current path resembling dipolar fields in the very center of the SRA.

We use the SRA for a numerical test of the mode-matching theory, as it shows only the excitable antenna mode depicted in Fig. 9.2(b). We chose two positions for the dipole, one in the very center of the gap (green circle), one in the point of highest fields along the y -axis in 11 nm distance from the center (blue circle). The ratio of mode near-field at the given positions is evaluated by illuminating the antenna with a normalized Gaussian of NA= 1 and $\lambda = 650$ nm, yielding a power ratio of $P_{\text{rel}} = E_{\text{max}}/E_{\text{center}} = 1.441$.

To check the validity of eq. (9.8), it is integrated numerically to retrieve mode-matching power enhancement P_{mm} :

$$P_{\text{mm}} = \frac{P}{P_0} \propto \sum_r \mathbf{E}_\nu(r) \cdot \mathbf{E}_{\text{dip}}(r) \quad . \quad (9.23)$$

Here r is indexing all Yee-Cells within the antenna volume. The antenna shows a field enhancement, large enough to omit the contribution of the dipole emission directly into vacuum. \mathbf{E}_ν was calculated with the above mentioned Gaussian excitation, the two \mathbf{E}_{dip} with a dipole source at a center frequency $\lambda_{\text{dip}} = 650$ nm and a pulse length of ≈ 4 fs at the respective positions and a subsequent Fourier-transformation to retrieve the quasi-static fields. The

ratio $P_{\text{mm,max}}/P_{\text{mm,center}} = 1.451$ differs from P_{rel} only by a factor of 0.007 which is within any error margin and most probably originates in numerical inaccuracies due to using different light sources.

9.4 Intelligent design of nanoantennas

The integral in eq. (9.8) over the product of dipolar fields and mode currents within the FOA volume is comparable to mode matching formalisms used to determine coupling efficiencies between propagating modes at surfaces [54,168]. Here, however, the three-dimensional volume of the FOA has to be considered. It is no surprise that the power transfer from the QE to the FOA is the basis of the overall emission power enhancement, since the dipole is the only energy source in the given system. However, contrary to eq. (9.2) the mode-matching formalism eq. (9.8) allows to draft intuitive qualitative rules that optimize the LDOS enhancement at the QE position:

$$\frac{P}{P_0} \propto \int_{V_\nu} \underbrace{\mathbf{E}_m}_{(i)} \cdot \underbrace{\mathbf{j}_\nu}_{(ii)} \underbrace{dV}_{(iii)} \quad (9.24)$$

has to be maximal. This can be achieved by:

1. Aligning dipolar and mode field as good as possible. The particles surface defines the current direction of its supported modes which can be adjusted as well as the distortion of the single emitter field due to the angle between field and metal surface.
2. Maximizing the mode current strength at each point inside the plasmonic antenna. This is mainly a material issue as $\mathbf{j} = \sigma \cdot \mathbf{E}_\nu$ depends on the conductivity σ .
3. Maximizing the overall volume of the overlap integral.

Rules number (ii) and (iii) suggest that the established two particle geometries are not the optimum for focusing by means of plasmonic resonances. Instead, a FOA should fully enclose the QE, which we propose the term plasmonic cavity antenna (PCA) for.

However, a FOA has to be optimized for two tasks (compare to [21]): In addition to providing a maximal LDOS it also has to couple efficiently to

propagating far-fields. For small particles within the quasistatic limit this is achieved by maximizing its polarizability, which links the overall dipolar moment to impinging plane waves (see chpt. 3.2.2). Therefore, we extend the setting and add a plane wave at the position of the QE-FOA system which is polarized along the QE dipole moment. This results in a second mode-matching criterion for optimizing the far-field coupling of FOAs in addition to its near-field coupling to the QE. The optimal mode field pattern to fulfill both mode-matching criterion is a linear combination of quasi-static dipolar fields:

$$\mathbf{E}_d = \frac{1}{4\pi\epsilon_0} \frac{3\mathbf{n}(\mathbf{n}\mathbf{p}) - \mathbf{p}}{r^3} \quad (9.25)$$

, now with $\mathbf{p} = \hat{\mathbf{x}}$ aligned along the x -axis and a constant field pointing along the QE dipole moment:

$$\mathbf{E}_m = \mathbf{E}_d + a \cdot \hat{\mathbf{x}} \quad . \quad (9.26)$$

The scalar factor a can be positive or negative, leading to two fundamentally different optimal focusing antenna mode patterns as illustrated in Fig. 9.3(a), which we will denote 'n-type' mode (left) and 'p-type' (right) mode. In the very center of these modes dipolar fields dominate. As the distance gets larger, the dipolar field falls off with $1/r^3$ and the homogeneous field starts to dominate. This leads to points with zero field strength on the x -axis for the n-type mode and on a ring in the y - z -plane for the p-type mode (marked with white dashed circles).

Figure 9.3(b) is a reprint of Fig. 8.4(b). With the here presented mode-matching formalism it is now possible to recognize the current pattern of this evolutionary optimized FOA as a p-type mode (areas with vanishing fields marked with white dashed circles) and understand its working principle. The antenna center is surrounded with gold, realizing the 2D-equivalent of an PCA. The currents switch direction as one moves from the antenna center along the y -axis to match the needs for optimal far-field coupling.

Figure 9.3(c) introduces a PCA geometry in three dimensions demonstrating the n-type mode, which to our knowledge has not yet been realized in an OA until now. Its rotational symmetric geometry is based on a reference antenna (RA) in the shape of a two wire dipolar antenna with a 10 nm gap, 15 nm wire diameter with spherical end caps and an overall length $l = 110$ nm made from gold (see small black cross section in Fig. 9.3(d)). The RA

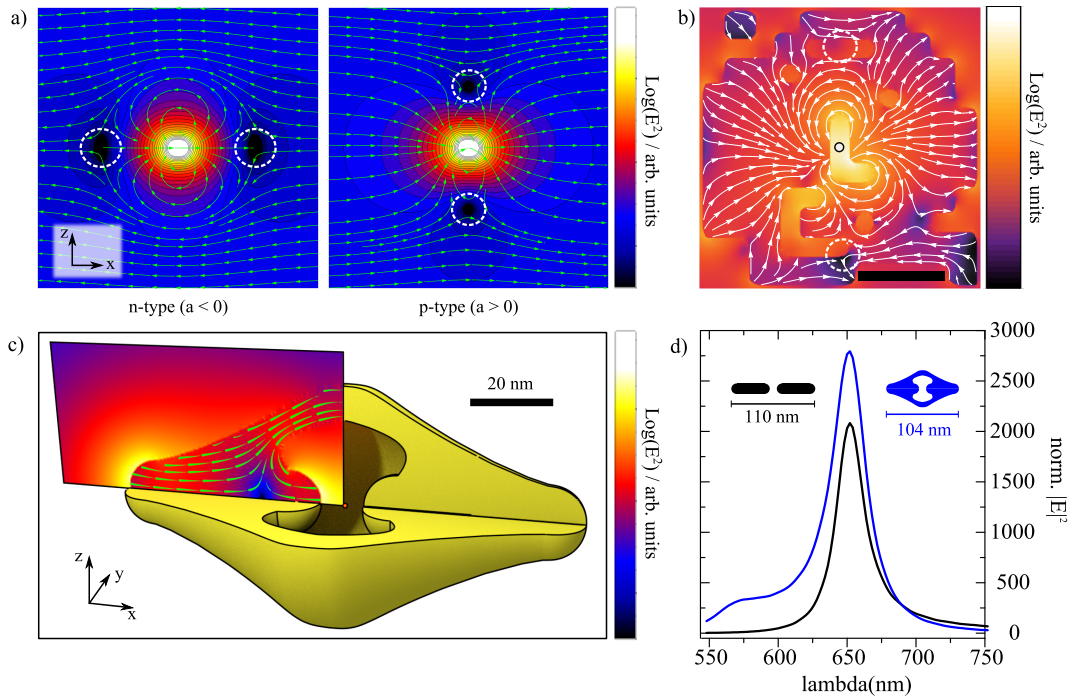


Figure 9.3: (color online) Plasmonic antenna modes with double mode-matching. (a) x - y -cross section of the linear combination of quasistatic dipolar field and constant field pointing in x -direction as described by equation (9.26) for $a < 0$ (left) and $a > 0$ (right). The white dashed circles mark point of vanishing fields for better orientation in panel (b), showing the near field intensity enhancement (color scale) and the current direction (white arrows) of a planar antenna geometry optimized an evolutionary algorithm for maximum fields in the center (marked by small circle; scale-bar 100 nm) [166]. (c) Antenna design carrying a resonant mode resembling panel (a) left. The originally rotational symmetric geometry is shown with a 90° cutaway for improved visualization. Additionally the near-field intensity (color) as well as the current direction (green arrows) are overlay for a quarter cross section. The small orange dot marks the center, where a QE is to be placed. (d) Near-field intensity enhancement spectra at the green point in panel (c) (blue) as well as at the center of a two wire dipole reference antenna, with identical end cap radius (black). The small insets show a x - y -plane cross section of both geometries.

is optimized for being resonant at $\lambda = 650$ nm (black graph, Fig. 9.3(d)). To realize the PCA, interconnects were attached between the antenna arms to allow additional current paths, surrounding the QE with gold at the full solid angle of 4π . The length of the PCA was tuned to be again resonant at $\lambda = 650$ nm resulting in a slightly reduced length of $l = 104$ nm, 5.5% shorter than the RA. This is predicated on the PCA being a single particle showing a $\lambda/2$ -resonance contrary to the RAs λ -resonance (compare with sections 2.4.2 and 3.3.2), which is visible in the inset of Fig. 9.3(c)³. In the arms of the PCA the mode exhibits areas of vanishing fields along the x -axis, as expected for a n-type PCA mode.

Figure 9.3(d) shows broad band near field intensity enhancement (NFIE) spectra with $\lambda = 550 - 750$ nm at the antenna center of both the PCA and the RA when illuminated by a Gaussian focus with a numerical aperture of $NA = 1$. Both antenna spectra show a Lorentzian resonance shape peaking at $\lambda = 650$ nm with $NFIE_{PCA,max} = 2.79 \cdot 10^3$ and $NFIE_{RA,max} = 2.08 \cdot 10^3$ exhibiting Q-factors $Q = \lambda/\Delta\lambda$ of $Q_{PCA} = 22.0$ and $Q_{RA} = 27.1$. The PCA spectrum shows a second shallow peak at 570 nm, which originates in a mode comparable to the RA where the current density in x -direction does not change direction within the antenna volume. Q_{PCA} is 19% lower compared to Q_{RA} , pointing out more loss channels. An analysis of the antenna cross sections under plane wave illumination at $\lambda = 650$ nm results for the PCA in an absorption cross section of $\sigma_{PCA,abs} = 4.17 \cdot 10^4$ nm² and a scattering cross section of $\sigma_{PCA,sc} = 1.77 \cdot 10^4$ nm², yielding a scattering efficiency of $\eta_{PCA} = \sigma_{PCA,sc}/(\sigma_{PCA,abs} + \sigma_{PCA,sc}) = 0.298$. The numbers for the RA are $\sigma_{RA,abs} = 2.34 \cdot 10^4$ nm² and $\sigma_{RA,sc} = 0.362 \cdot 10^4$ nm², instead, leading to a 55% lower $\eta_{RA} = 0.134$ compared to the PCA. For particles small compared to the impinging wavelength the best coupling to the far-field is achieved, when $\sigma_{sc} = \sigma_{abs} \Rightarrow \eta = 0.5$ [70], so the PCA seems not only to optimize the near-field coupling, but also the far-field coupling. This originates in the PCA mode currents on the outer antenna surface resembling that of a $\lambda/2$ -antenna, which is in general more efficient than a lambda-antenna.

³The mode and the spectra were numerically acquired in Lumerical FDTD Solutions, with a $\lambda = 550 - 750$ nm broadband Gaussian focus illumination ($NA=1$, 3.9 fs pulse length). The gold material was implemented as introduced in section 3.1

9.5 p-type mode PCA

To realize a plasmonic cavity antenna (PCA) with cylindrical symmetry and an p-type mode on basis of the reference antenna (RA), its inner ends have to be shortcut in a shape resembling the dipole field loops. To asses the optimal thickness of such a geometry we examined the simplest realization: a spherical shell. Figure 9.4 shows the near-field intensity enhancement in the center of spherical shells for an incoming plane wave with $\lambda = 650$ nm, while radius r and shell thickness d are varied (compare also to [173]).

For small radii with dimensions of typical optical antenna gaps, the resonance shell thickness has to be comparably thin, between 1 and 3 nm. This can be understood by an effective wavelength argument: The geometry in Fig. 9.3(b) realizes the gap shortcut in a planar gold sheet with 30 nm thickness via two wires with a 'rectangular' cross section. To transform it into a spherical shell while keeping the overall shortcut cross section area about constant, the 'height' of the wire increases and its width shrinks. This keeps the effective plasmon wavelength roughly constant and thus conserve the resonance peak position [14].

Simply combining a plasmonic dipolar antenna with a 10 nm gap with a spherical shell of $r = 10$ nm and $d = 1$ nm results in the desired mode in quasi-static simulations. Yet, it was not possible to validate it by means of full wave FDTD simulations, as down to a center volume mesh size of 0.25 nm the stair-casing effect of the thin spherical shell leads to a severe mode shift and therefore to different NFIE spectra. Finer meshing was not feasible due to large simulation times. Anyway, this geometry is of pure academic value, as a 1 nm spherical gold shell filled with air is far from an experimental realization at the moment.

9.6 Discussion and Conclusion

The PCA design in Fig. 9.3(c) is only one possible realization and most probably not the best. The presented design guidelines are not sufficient to fully define the optimal antenna geometry. Instead, additional constraints like the effective wavelength, minimal curvature radii for fabrication should be given.

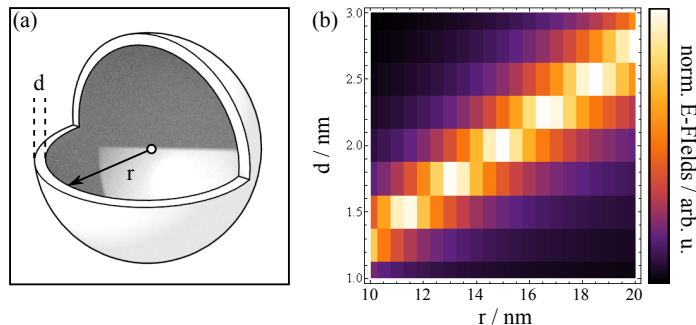


Figure 9.4: Resonances of sphere shells. (a) Sketch of an air filled metal shell, with cutaway for better visibility of the dimensions r , the inner radius and d , the shell thickness. (b) Normalized electric fields in the very center (white circle) of a gold nanoshell for a quasi-static excitation at $\lambda = 650$ nm for changing shell radius and thickness.

For larger antenna geometries the emergence of higher order modes with bad far-field mode-matching as well as retardation effects have to be kept in mind. Also the distortion of the fields as they penetrate the antenna surface at arbitrary angles is not taken into account in the optimal mode fields in Fig. 9.3(a). Finally the optimal magnitude of a in eq. (9.26) is still to be figured out.

Nevertheless, we have shown, that a combination of reciprocity with Poyntings theorem can be used to develop a three-dimensional mode-matching framework for describing optimal coupling between a quantum emitter and a plasmonic optical antenna. An analytically solved problem was used to prove the validity of the relation, which then allowed the development of new and superior geometries, so-called plasmonic cavity antennas on the basis of an already resonant two wire dipolar antenna. We also showed that the antenna coupling to the far-field can be tackled by mode-matching, leading to the important insight that the current pattern of a $\lambda/2$ -antenna should be realized at the outer antenna surface.

The proposed n-type PCA geometry is for sure not the best possible realization of the new antenna concept, as it has been designed to show as few changes as possible to a dipolar basic antenna for direct comparison. This framework can be generalized to more flexible antenna geometries and we believe it will help to optimize e.g. TERS-tips, leading to novel complex and surprising geometries as e.g. already shown in [174, 175]. To make use of the

full solid angle of 4π a combination of TERS tip and SERS substrate can be optimized together to realize plasmonic cavity antennas in experiment, which are not relying on the gap only.

Both near-field and far-field coupling tasks of an optical antenna can be modified to e.g. a larger volume for light concentration to e.g. optimize charge carrier excitation in semi-conductor nano structures, or to different and more complex excitation fields e.g. for non-perpendicular or radially polarized illumination as used in many TERS setups [176]. Finally this framework can be extended to multi-particle multi-mode systems, where several double mode-matching evaluations give the the overall far-field to near-field conversion efficiency. This might be a step to a better understanding of complex and large scale SERS-active substrates [177].

Chapter 10

Summary & Outlook

Optical antennas are powerful tools to enhance light-matter-interaction at the nano-scale as they can focus far-field radiation down to sub-diffraction-limited volumes by means of plasmon-mediated localized near-fields. They also can enhance the field intensity by several orders of magnitude when a plasmonic resonances is involved. Theory has made substantial progress in the last year describing the involved physics, e.g. the the mode volume of an optical antenna has been defined despite its non-negligible losses. However, an intuitive set of design rules more than 'smallest possible gaps' and 'sharpest possible tips' was missing. This is due to the necessity of solving the Green's function for a given system, which is rarely possible analytically. So the question was still open, if the regularly used antenna shapes inspired by radio-frequency technology are optimal, as plasmonic resonances introduce novel physical effects like volume currents and Ohmic losses as well as unusual driving schemes like the coupling to a quantum emitter.

A few groups already identified the focusing by means of a plasmonic structure as an optimization problem, using the heuristic approach of evolutionary optimization to find unexpected geometries. However the parameter space was always very limited, and no novel working principles had been discovered. In this work a novel genetic algorithm has been developed, fixing neither particle shape nor number. It is capable to describe complex planar geometries based on a binary matrix as genome encoding the positions of gold voxels in a plane. In the first implementation the best solution of the evolutionary algorithm surpasses every radio-frequency inspired design by a factor of 2 within the

configuration space of a 21×21 matrix of perfect 10 nm gold cubes at 650 nm excitation wavelength.

The second implementation was adapted to realistic geometries with rounded features originating from any fabrication method with a limited resolution. After identifying the minimal reproducible dimensions of an focused ion beam machine, an evolutionary antenna described by an 11×11 matrix representing a $(330 \text{ nm})^2$ area with 30 nm thickness surpassed comparable rf-designs, too, at 830 nm excitation wavelength. Additionally, a 'printer driver' was developed that allowed the direct fabrication of any genome as antenna from a polished monocrystalline gold flake. The hierarchy of six evolved structures was reproduced in experiment when measuring the two-photon-photo-luminescence by means of confocal microscopy.

More interestingly, the shapes of the evolutionary antennas were not intuitive at first sight. A systematic examination allowed to derive novel underlying physical principles. Currents resembling fundamental split-ring resonator modes can be added to the well-known dipolar antenna modes to enhance the concentration of charge density at the gap of a nanoantenna. This setup also allows to drive the fundamental magnetic dipole mode of a split-ring at frequencies not possible for single rings due to kinetic inductivity.

A closer look to the mode current pattern of the best realistic evolutionary antenna spawned the idea that the split-ring-like mode currents might resemble field lines of a point dipole. As a matter of fact a three-dimensional mode-matching formalism for the antenna mode and the dipole fields inside an optical antenna could be derived from first principles, which is able to describe the energy transfer from an excited quantum emitter to an optical antenna. An analytical prove for the case of a dipole in front of a sphere has been given.

From the mode-matching formalism a new set of intuitive design rules was derived for focusing to a single point in space by means of an optical antenna. In addition, by adding a second mode-matching condition to optimize far-field coupling, two different optimal mode patterns could be identified, differing in the phase between radiation fields and dipolar near-fields. One of these patterns fits to the modes found within the evolutionary antennas.

From the second optimal mode pattern an enhanced focusing optical antenna, a so-called plasmonic cavity antennas, could be devised on the basis of a

reference dipole antennas, proving the existence of these modes in rotationally symmetric geometries and their potential for optimized focusing. Surprisingly, it seems that the coupling to the far-field was a limiting factor for the dipolar antennas, too, as the novel modes suggest an ideal optical antenna to show a $\lambda/2$ -mode current instead of a λ -mode current at its outer surface.

Do we have an answer to the question, how the optimal focusing antenna should look like? Unfortunately not yet. The journey is not over. But a substantial progress has been made and the direction of the next steps seems to be clear. At least three paths for further research at focusing optical antennas are available:

(I) Experimental realization: The possibilities of the split-ring antenna can be explored further. It has already some applications due to its comparably simple shape. It has been shown, that the incoupling into two-wire waveguides can be optimized (unpublished results, together with Peter Geisler and Florian Bauer) and that SERS can be enhanced in mass fabricated arrays [178]. Unfortunately, the SRA with the dimensions shown in this work is not very useful as meta-material building block, as its absorption is too large (unpublished work). Larger variations with better far-field coupling might still be useful, which still has to be checked.

Furthermore, the fabrication of fully three-dimensional structures is desirable, to realize plasmonic cavity antenna geometries derived from the mode-matching formalism. Therefore, a combination of topographically structured metal surfaces with a structured metal AFM-tip could be used to combine two half antennas and realize a complete new class of plasmonic nano structures.

The fabrication by means of FIB milling with a Ga-ion-beam limits the miniaturization of reproducible feature sizes to about 20 nm. Since a few years, also Helium ions can be used for microscopy (HIM) as well as for nanofabrication [144]. At the University of Bielefeld the test pattern introduced in chapter 8 has been milled in gold-flakes by means of HIM. Since the machine was quite new, the milling parameters were not optimized to maximum extent. Still Fig. 10.1 shows the feasible dimensions being reduced by a factor of 6.

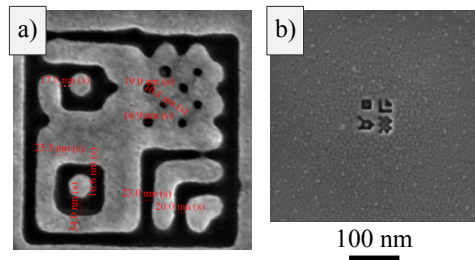


Figure 10.1: Minimal reproducible dimensions for ion-beam-milling with a) Ga-ions; b) He-ions.

(II) Evolutionary algorithm: The simplest advancement is the adaption of the evolutionary algorithm the new minimum dimensions, enabled by milling with He-ions. This will allow to optimize planar antennas further.

But the evolutionary approach is very flexible. Other optimization goals can be e.g. broadband focusing or directed scattering for photovoltaics, magnetic switching in small volumes and optimized second-harmonic generation. With extended numerical approaches to solve multi-physics problems incorporating also mechanics, heat transport, etc. the possible applications are enormous. An extreme case could be the optimization of electrodes for solar-fuel synthesis, where the optical behavior of metal and semi-conductor nano-structures is only one figure of merit. In addition heat generation influences chemical rate equations, which are further altered by the catalytic properties of different electrode materials. Also the generation of charge carriers in semi-conductors, their diffusion and recombination on surfaces plays an important role, not to forget the material transport of the solar-fuel educts and products in liquids.

(III) Mode-matching formalism: Until now there is still no simple recipe to retrieve the shape of an optimized antenna for the simple setup described within this work (Fig. 9.1). The next step is not to stick to geometries similar to a reference antenna, but to constrain e.g. only the minimum feature curvature. The overlap integral formalism might also allow the application of other optimization schemes, like variational principles.

The double mode-matching criterion can also be applied for other experimental environments e.g. different tip-enhanced Raman spectroscopy setups, depending on the illumination direction (side or annular) [176] and the polarization to be detected (in-plane or out-of-plane). The presented framework can

easily be extended to dielectric particles or more complex experimental conditions and might open a way to understand the working principles of complex shaped metal nano-devices e.g. substrates used for surface enhanced Raman spectroscopy (SERS) [177]. For large scale plasmonic devices an extension of the mode-matching formalism to capture retardation effects is desirable.

Finally, it seems that there are still many steps to go until an optimal shape of a focusing optical antenna has been defined, which might be in a few decades automatically recognized, the same way as the shape of a hammer is recognized today. But to be realistic, there might be too many different applications for only one optical antenna shape to become canonical. For example in the field of SERS a large area is illuminated and the substrate should provide multiple hot spots. Most likely there will not be a single most effective geometry. However, the mode-matching framework might help to understand and improve the working principle behind the most effective geometries, for SERS and many other applications.

Part IV
Appendix

Appendix A

Number of non redundant binary odd-sized square matrices with one symmetric and one antisymmetric axis

Given is a binary $n \times n$ -matrix A with odd n , $A_{x,y} \in [0, 1]$ and $A_{(n+1)/2,(n+1)/2} = 0$. It describes a plasmonic nano structure which is oriented in the x - y -plane centered on the z -axis and thus to the optical axis of the system. The linear excitation polarization is oriented along the x -axis resulting in electric fields, that are symmetric with respect to the x - z -plane and antisymmetric with respect to the y - z -plane. Consequently, structures that differ among each others only by a respective symmetry operation will result in the same physical behavior, although the matrix apparently changes. For matrix sizes with $n \rightarrow \infty$ one can estimate that about 3/4 of the possible structures are physically redundant. Considerable computational effort can therefore be avoided by checking each newly generated structure for redundancy with already simulated structures.

First we calculate the number of structures with special symmetries within the set of all matrices as defined above.

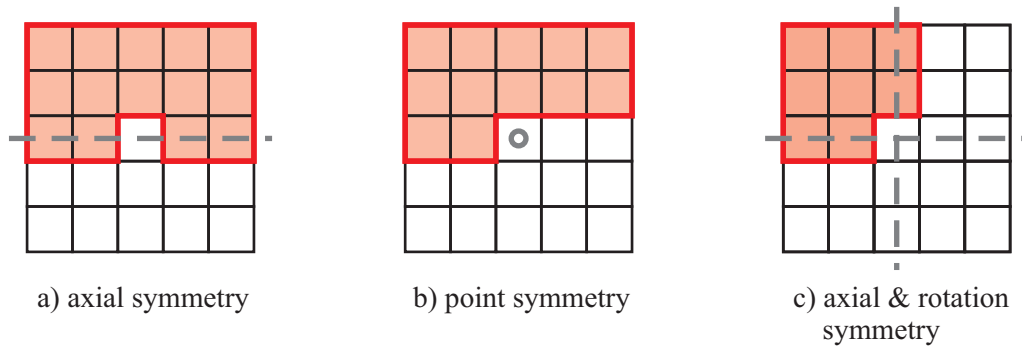


Figure A.1: At the example of 5×5 matrices, the necessary areas to describe structures with given symmetry axes (grey) are marked in red.

Axial symmetry

In the case of axial symmetry the values in one row containing the center ($n-1$ elements) and a half matrix (rectangle of $n \cdot (n-1)/2$ elements; see Fig. A.1(a)) completely define a structure. The overall number N_A of independent structures is thus:

$$N_A = 2^{(n-1)+n \cdot \frac{n-1}{2}} = 2^{(n-1)(\frac{n}{2}+1)} \quad (\text{A.1})$$

Point symmetry

In the case of point symmetry, the values in half a row ($(n-1)/2$ elements) and half a matrix completely describe the structures (see Fig. A.1(b)), yielding

$$N_P = 2^{\frac{n-1}{2} + \frac{n(n-1)}{2}} = 2^{\frac{n^2-1}{2}} \quad (\text{A.2})$$

different configurations.

Point and axial symmetry

Every matrix, which is symmetric to both axis is also point symmetric, and every matrix which is symmetric to the origin and to one axis, is also symmetric to the other axis. Thus only one overlapping set of all three single symmetry sets has to be computed. It is defined by a quarter matrix including the on-axis

elements and excluding the center block (see Fig. A.1(c)):

$$N_{AP} = 2^{\left(\frac{n+1}{2}\right)^2 - 1} \quad (\text{A.3})$$

Counting

Each matrix, which does not have one of the described symmetries can be transformed into three physical identical matrices by mirroring at the x - and y -axis. Thus the number of non physically redundant non symmetric structures is their complete number N_{NS} divided by four. N_{NS} can be computed as the number of all possible structures $N_{\infty} = 2^{n^2-1}$ minus all symmetric structures. As there are two mirror axes, the number of axis symmetric matrices N_A has to be subtracted twice and the number of point symmetric structures once. The set of both point- and axis-symmetric matrices has then been subtracted three times and is re-added 2 times therefore. This leads to:

$$N_{NS} = \frac{N_{\infty} - 2N_A - N_P + 2N_{AP}}{4} \quad (\text{A.4})$$

Each axis and point symmetric structure can be mirrored into exactly one physical redundant but geometrical different structure. So to get the number of physical unique matrices, their number has to be divided by two after subtracting the structures with both symmetries.

$$N_{A,P} = \frac{2 \cdot N_A + N_P - 3 \cdot N_{AP}}{2} \quad (\text{A.5})$$

The structures with axes and point symmetry have to be counted completely, since no symmetry operation changes them neither geometrically nor physically.

The resulting complete number N of physically unique square matrices with odd side length n is:

$$N = N_{NS} + N_{A,P} + N_{AP} \quad (\text{A.6})$$

$$\Rightarrow N = \frac{1}{8} \left(2^{n^2} + 2^{\frac{1}{2}(n^2+1)} + 2^{\frac{1}{2}(n^2+n+2)} \right) \quad (\text{A.7})$$

An evaluation of this formula for increasing matrix sizes is depicted in Fig. A.2. It shows, that for matrix sizes of 5 and bigger 75 percent of all structures are redundant. A considerable speed enhancement of the evolutionary

algorithm is achieved by checking newly generated matrices for redundancies with already evaluated structures.

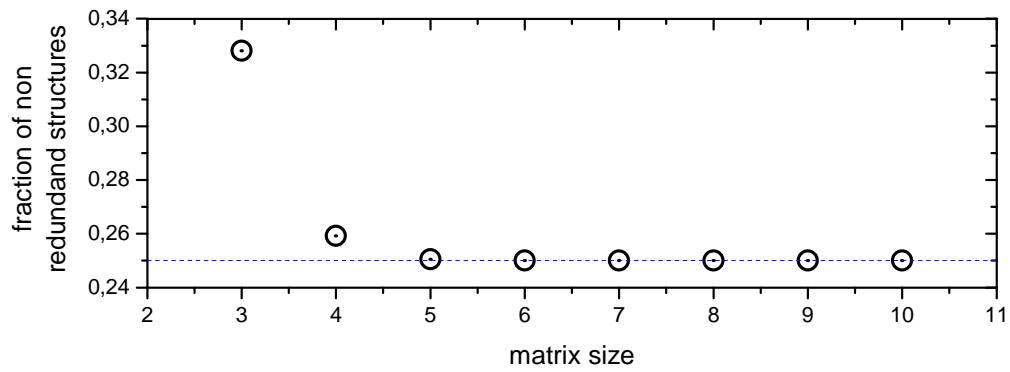


Figure A.2: Amount of non redundant structures for the setup described in the text. For larger matrix sizes the limit of the fraction of not physically redundant square matrices is 0.25 (blue dashed line).

Appendix B

Local configuration space maxima in experimental EA

Fig. B.1 shows a exemplary run of the realistic evolutionary algorithm as described in detail in chapter 8, getting into and leaving a local maximum in configuration space.

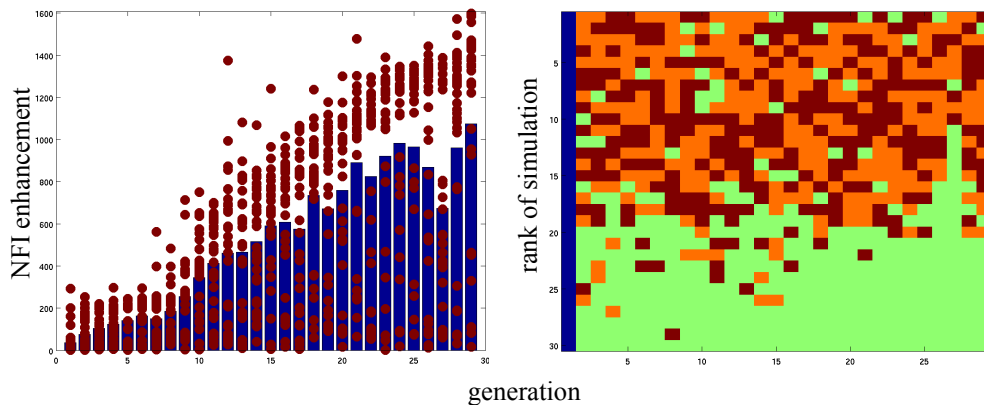


Figure B.1: Left: Near-field intensity (NFI) enhancement for all individuals (red dots) together with mean NFI enhancement per generation (blue bars) of one evolutionary run. Right: Origin of single individuals sorted after generation and after fitness within one generation. The first generation is generated from random matrices with a filling factor of 0.7 (blue), the rest is inherited via mutation (green), spiral crossing (red) and linear crossing (orange).

The left part shows the improvement of each consecutive generation, except of a major dip in the mean fitness per generation (blue bars) at generations 26

to 28. The right part shows the origin of each single individual (see caption for legend) and the fraction of individuals per generation is normally fixed to 0.4 mutation, and 0.3 for each crossing. However, in generation 27 a greater fraction is generated by mutation compared to crossings.

This originates in the implemented test for redundant structures (see also appendix A) which is performed after each crossing step and starts a new crossing try if a redundant structure was generated. This only is done 200 times to eliminate infinity loops and thus replaced by mutation.

Having lots of mutation-generated antennas in generation 27 together with the drop in the fitness is a clear sign of a local maximum in configuration space, which has been explored nearly completely by the algorithm. No new geometries with similar features and comparable or better fitness can be generated via crossings and thus mutation is the only way to create new and non-simulated antennas. This will eventually lead to a worse antenna fitness first, but will by chance introduce new structural features which can finally lead to further enhancement as can be seen already in the very last generation.

We have observed this behavior in many different runs of the EA and data can be made public after request.

Appendix C

Fitness changes in realistic evolutionary antennas due to fabrication inaccuracies.

To assess the effect of a decreased thickness on the fitness of the evolutionary antennas, simulations of the six fabricated geometries were performed and the results plotted in Fig. C.1(a). The fitness is reduced for thinner antennas, as the resonance shifts into the red [71], away from the wavelength of optimization. Except for antenna #5 the fitness hierarchy is maintained which can be explained with the spectra of all antennas (Fig. 8.6). Antenna #5 is the only one with a relative blue shift with respect to the optimization wavelength, therefore being the only antenna optimized by the red shift.

The fabrication of the holes and lines needed to realize the evolutionary antennas has a uncertainty of ± 1 nm. The influence of such a deviation in the geometry on the fitness all six fabricated antennas has been simulated by increasing as well as decreasing all hole diameters by 1 nm. The results in Fig. C.1(b) show nearly no influence of this parameter on the relative fitness hierarchy. The large absolute fitness increase for smaller hole sizes – which is about 100 nm^{-1} – originates from the enhanced capacitive coupling in the center gap, when the accumulating charges are less separated. This observation also explains the error bar within the TPPL measurements for all structures.

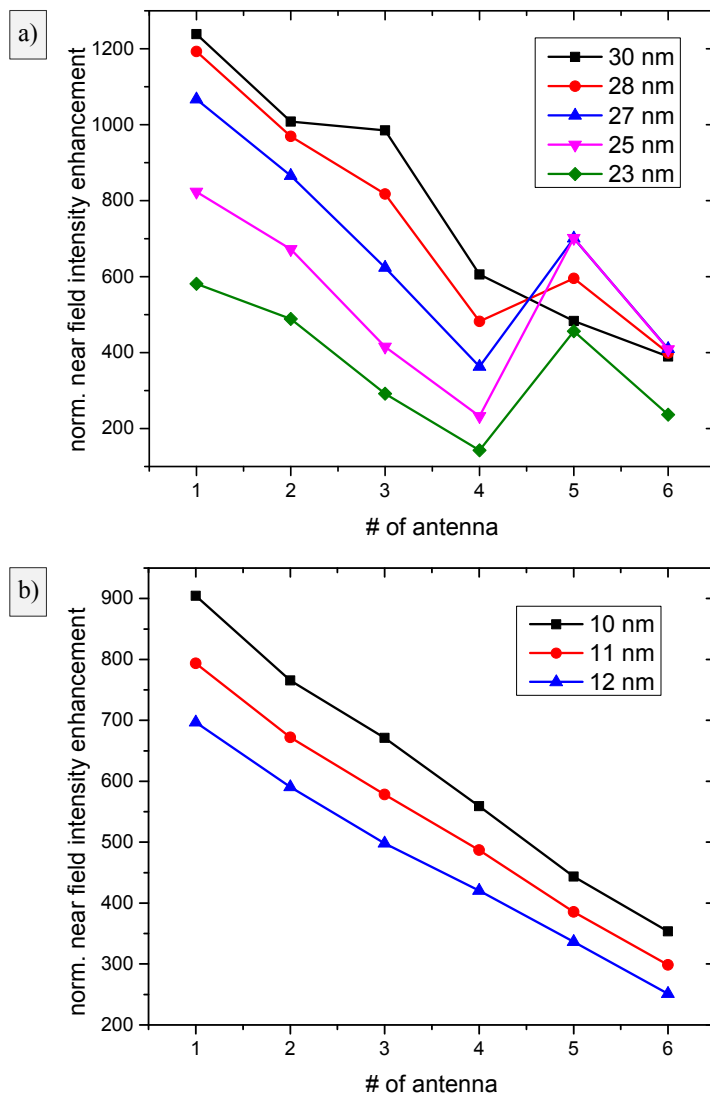


Figure C.1: a) Change in fitness of evolutionary antennas for different layer thicknesses. The best four antennas decrease in near-field intensity enhancement as their thickness is reduced, the last two behave not systematically. b) Change in fitness of evolutionary antennas dependent on the hole diameter / line width. As the width gets smaller, the near-field intensity enhancement increases by a large margin.

Appendix D

List of publications

Feichtner, T.; Christiansen S.; Hecht, B.: *Modematching for optical antennas*; arXiv:1611.05399 (submitted first 2016)

T. Feichtner, O. Selig, and B. Hecht, *Plasmonic nanoantenna design and fabrication based on evolutionary optimization*; arXiv1511.05438v1 (submitted first 2015).

C. Tessarek, S. Fladischer, C. Dieker, G. Sarau, B. Hoffmann, M. Bashouti, M. Göbelt, M. Heilmann, M. Latzel, E. Butzen, S. Figge, A. Gust, K. Höfflich, T. Feichtner, M. Büchele, K. Schwarzburg, E. Spiecker and S. Christiansen, *Self-catalyzed growth of vertically aligned InN nanorods by metal-organic vapor phase epitaxy*; Nano Lett. 16, 3415 (2016).

Chen K., Razinskas G., Feichtner T., Grossmann S., Christiansen S., Hecht B.: *Electromechanically Tunable Suspended Optical Antenna*; Nano Lett. 16, 2680 (2016).

B. Hoffmann, T. Feichtner, and S. Christiansen: *Gold platelets for high-quality plasmonics*; Mater. Today 19, 240 (2016).

B. Hoffmann, M.Y. Bashouti, T. Feichtner, M. Mackovic, C. Dieker, A.M. Salaheldin, P. Richter, O. Gordan, D. Zahn, E. Spiecker, and S. Christiansen, *New insights into colloidal gold flakes: structural investigation, micro-ellipsometry and patterning procedure towards ultrathin monocrystalline layers* Nanoscale 8, 4529-4536 (2016).

P. Then, G. Razinskas, T. Feichtner, P. Haas, A. Wild, N. Bellini, R. Oselame, G. Cerullo, and B. Hecht, *Remote detection of single emitters via optical waveguides*; Phys. Rev. A 89, 053801 (2014).

T. Feichtner, O. Selig, M. Kiunke, and B. Hecht, *Evolutionary Optimization of Optical Antennas*; Phys. Rev. Lett. 109, 127701 (2012).

J.-S. Huang, V. Callegari, P. Geisler, C. Brünig, J. Kern, J. C. Prangma, X. Wu, T. Feichtner, J. Ziegler, P. Weinmann, M. Kamp, A. Forchel, P. Biagioni, U. Sennhauser, and B. Hecht, *Atomically flat single-crystalline gold nanostructures for plasmonic nanocircuitry*; Nat. Commun. 1, 150 (2010).

J.-S. Huang, T. Feichtner, P. Biagioni, and B. Hecht, *Impedance Matching and Emission Properties of Nanoantennas in an Optical Nanocircuit*; Nano Lett. 9, 1897 (2009).

Bibliography

- [1] Stefan A. Maier. *Plasmonics: Fundamentals and Applications*. Springer-Verlag, 2007.
- [2] Ming Liu and Xiang Zhang. Nano-optics: Plasmon-boosted magneto-optics. *Nature Photonics*, 7(6):429–430, 2013.
- [3] Matthew E Stewart, Christopher R Anderton, Lucas B Thompson, Joana Maria, Stephen K Gray, John A Rogers, and Ralph G Nuzzo. Nanos-structured plasmonic sensors. *Chemical Reviews*, 108:494–521, 2008.
- [4] Yulan Fu, Xiaoyong Hu, Cuicui Lu, Song Yue, Hong Yang, and Qihuang Gong. All-optical logic gates based on nanoscale plasmonic slot waveguides. *Nano letters*, 12(11):5784–90, 2012.
- [5] Vladimir M. Shalaev. Optical negative-index metamaterials. *Nature Photonics*, 1(1):41–48, 2007.
- [6] Nina Meinzer, William L. Barnes, and Ian R. Hooper. Plasmonic meta-atoms and metasurfaces. *Nature Photonics*, 8(12):889–898, 2014.
- [7] Harry A Atwater and Albert Polman. Plasmonics for improved photovoltaic devices. *Nat Mater*, 9(3):205–213, 2010.
- [8] L. R. Hirsch, R. J. Stafford, J. A. Bankson, S. R. Sershen, B. Rivera, R. E. Price, J. D. Hazle, N. J. Halas, and J. L. West. Nanoshell-mediated near-infrared thermal therapy of tumors under magnetic resonance guidance. *Proceedings of the National Academy of Sciences*, 100(23):13549–13554, 2003.

- [9] Oara Neumann, Alexander S. Urban, Jared Day, Surbhi Lal, Peter Nordlander, and Naomi J. Halas. Solar vapor generation enabled by nanoparticles. *ACS Nano*, 7(1):42–49, 2013.
- [10] Nan Zhou, Xianfan Xu, Aaron T. Hammack, Barry C. Stipe, Kaizhong Gao, Werner Scholz, and Edward C. Gage. Plasmonic near-field transducer for heat-assisted magnetic recording. *Nanophotonics*, 3(3):141–155, 2014.
- [11] Dmitri K. Gramotnev and Sergey I. Bozhevolnyi. Nanofocusing of electromagnetic radiation. *Nature Photonics*, 8(1):13–22, 2013.
- [12] E. Abbe. Beiträge zur theorie des mikroskops und der mikroskopischen wahrnehmung. *Archiv für Mikroskopische Anatomie*, 9:413–418, 1873.
- [13] Lukas Novotny and Stephan J Stranick. Near-field optical microscopy and spectroscopy with pointed probes. *Annual review of physical chemistry*, 57:303–331, 2006.
- [14] Lukas Novotny. The history of near-field optics. *Progress in optics*, 50:137–184, 2007.
- [15] Vasilii V. Klimov, M. Ducloy, and V. S. Letokhov. Spontaneous emission of an atom in the presence of nanobodies. *Quantum Electronics*, 31(7):569, 2001.
- [16] Lukas Novotny and Bert Hecht. *Principles of Nano-Optics*. Cambridge University Press, 2nd edition, 2012.
- [17] Gleb M. Akselrod, Christos Argyropoulos, Thang B. Hoang, Cristian Ciraci, Chao Fang, Jiani Huang, David R. Smith, and Maiken H. Mikkelsen. Probing the mechanisms of large Purcell enhancement in plasmonic nanoantennas. *Nature Photonics*, 8(11):835–840, 2014.
- [18] R. Zhang, Y. Zhang, Z. C. Dong, S. Jiang, C. Zhang, L. G. Chen, L. Zhang, Y. Liao, J. Aizpurua, Y. Luo, J. L. Yang, and J. G. Hou. Chemical mapping of a single molecule by plasmon-enhanced Raman scattering. *Nature*, 498(7452):82–86, 2013.

- [19] Yuanjie Pang and Reuven Gordon. Optical trapping of a single protein. *Nano letters*, 12(1):402–6, 2012.
- [20] Thang B Hoang, Gleb M Akselrod, Christos Argyropoulos, Jiani Huang, David R Smith, and Maiken H Mikkelsen. Ultrafast spontaneous emission source using plasmonic nanoantennas. *Nature communications*, 6:7788, 2015.
- [21] R L Olmon and M B Raschke. Antenna–load interactions at optical frequencies: impedance matching to quantum systems. *Nanotechnology*, 23(44):444001, 2012.
- [22] Constantine A Balanis. Antenna theory: A review. *Proceedings of the IEEE*, 80:7–23, 1992.
- [23] Jens Dorfmueller, Ralf Vogelgesang, Worawut Khunsin, Carsten Rockstuhl, Christoph Etrich, and Klaus Kern. Plasmonic nanowire antennas: experiment, simulation, and theory. *Nano letters*, 10(9):3596–603, 2010.
- [24] J. Zhou, Th. Koschny, M. Kafesaki, E. N. Economou, J. B. Pendry, and C. M. Soukoulis. Saturation of the magnetic response of split-ring resonators at optical frequencies. *Phys. Rev. Lett.*, 95:223902, 2005.
- [25] P. Mühlischlegel, H-J H.-J. J Eisler, O. J. F. Martin, B. Hecht, and D. W. Pohl. Resonant Optical Antennas. *Science*, 308(5728):1607–1609, 2005.
- [26] P. J. Schuck, D. P. Fromm, A. Sundaramurthy, G. S. Kino, and W. E. Moerner. Improving the mismatch between light and nanoscale objects with gold bowtie nanoantennas. *Physical Review Letters*, 94(1):17402, 2005.
- [27] J. N. Farahani, D. W. Pohl, H.-J. Eisler, and B. Hecht. Single Quantum Dot Coupled to a Scanning Optical Antenna: A Tunable Superemitter. *Physical Review Letters*, 95(1):17402, 2005.
- [28] Alberto G Curto, Giorgio Volpe, Tim H Taminiau, Mark P Kreuzer, Romain Quidant, and Niek F van Hulst. Unidirectional Emission of a Quantum Dot Coupled to a Nanoantenna. *Science*, 329(5994):930–3, 2010.

- [29] John David Jackson. *Classical Electrodynamics*. John Wiley & Sons, New York, third edition edition, 1998.
- [30] Kai Fong Lee. *Principles of antenna theory*. Friedr. Vieweg & Sohn Verlag | GWV Fachverlage GmbH, 1984.
- [31] Ruben Esteban, Andrei G. Borisov, Peter Nordlander, and Javier Aizpurua. Bridging quantum and classical plasmonics with a quantum-corrected model. *Nature Communications*, 3:825, 2012.
- [32] D.C. Marinica, A.K. Kazansky, P. Nordlander, J. Aizpurua, and A. G. Borisov. Quantum plasmonics: Nonlinear effects in the field enhancement of a plasmonic nanoparticle dimer. *Nano Letters*, 12(3):1333–1339, 2012.
- [33] Peng Song, Peter Nordlander, and Shiwu Gao. Quantum mechanical study of the coupling of plasmon excitations to atomic-scale electron transport. *The Journal of Chemical Physics*, 134(7):074701–074701–5, 2011.
- [34] Jorge Zuloaga, Emil Prodan, and Peter Nordlander. Quantum description of the plasmon resonances of a nanoparticle dimer. *Nano Letters*, 9(2):887–891, 2009.
- [35] Jeffrey M McMahon, Stephen K Gray, and George C Schatz. Nonlocal Optical Response of Metal Nanostructures with Arbitrary Shape. *Physical Review Letters*, 103(9):97403, 2009.
- [36] Huigao Duan, Antonio I. Fernandez-Dominguez, Michel Bosman, Stefan A. Maier, and Joel K. W. Yang. Nanoplasmonics: Classical down to the nanometer scale. *Nano Letters*, 12(3):1683–1689, 2012.
- [37] Kevin J. Savage, Matthew M. Hawkeye, Ruben Esteban, Andrei G. Borisov, Javier Aizpurua, and Jeremy J. Baumberg. Revealing the quantum regime in tunnelling plasmonics. *Nature*, 491(7425):574–577, 2012.
- [38] Jonathan A. Scholl, Ai Leen Koh, and Jennifer A. Dionne. Quantum plasmon resonances of individual metallic nanoparticles. *Nature*, 483(7390):421–427, 2012.

- [39] Jonathan A. Scholl, Aitzol Garcia-Etxarri, Ai Leen Koh, and Jennifer A. Dionne. Observation of quantum tunneling between two plasmonic nanoparticles. *Nano Letters*, 13(2):564–569, 2013.
- [40] M. S. Tame, K. R. McEnery, S. K. Ozdemir, J. Lee, S. A. Maier, and M. S. Kim. Quantum plasmonics. *Nature Physics*, 9(6):329–340, 2013.
- [41] Paul J. Nahin. *Oliver Heaviside: The Life, Work, and Times of an Electrical Genius of the Victorian Age*. JHU Press, 2002.
- [42] Stefan W. Hell. Far-field optical nanoscopy. *Science*, 316:1153–1158, 2007.
- [43] M. Minsky. Memoir on inventing the confocal scanning microscope. *Scanning*, 10(4):128–138, 1988.
- [44] Feng Wang, Gordana Dukovic, Louis E. Brus, and Tony F. Heinz. Time-Resolved Fluorescence of Carbon Nanotubes and Its Implication for Radiative Lifetimes. *Physical Review Letters*, 92(17):177401, 2004.
- [45] M. Arcari, I. Söllner, A. Javadi, S. Lindskov Hansen, S. Mahmoodian, J. Liu, H. Thyrrstrup, E. H. Lee, J. D. Song, S. Stobbe, and P. Lodahl. Near-Unity Coupling Efficiency of a Quantum Emitter to a Photonic Crystal Waveguide. *Physical Review Letters*, 113(9):093603, 2014.
- [46] E. M. Purcell. Proceedings of the american physical society. *Phys. Rev.*, 69:674–674, 1946.
- [47] Karl H. Drexhage. Interaction of light with monomolecular dye layers. In E. Wolf, editor, *Progress in Optics XII*, pages 163 – 232. Elsevier, 1974.
- [48] Rodney Loudon. *The Quantum Theory of Light*. Oxford University Press, 2000.
- [49] Kerry J Vahala. Optical microcavities. *Nature*, 424(6950):839–46, 2003.
- [50] H. Hertz. *Electric Waves: Being Researches on the Propagation of Electric Action with Finite Velocity Through Space*. Dover books on history of science and classics of science. Dover Publications, 1893.

- [51] John P. Snyder. *Flattening the Earth: Two Thousand Years of Map Projections*. University of Chicago Press, 1997.
- [52] J. N. Walford, J. A. Porto, R. Carminati, J.-J. Greffet, P. M. Adam, S. Hudlet, J.-L. Bijeon, A. Stashkevich, and P. Royer. Influence of tip modulation on image formation in scanning near-field optical microscopy. *Journal of Applied Physics*, 89(9):5159–5169, 2001.
- [53] R J Potton. Reciprocity in optics. *Reports on Progress in Physics*, 67(5):717–754, 2004.
- [54] Patrick Then, Gary Razinskas, Thorsten Feichtner, Philippe Haas, Andreas Wild, Nicola Bellini, Roberto Osellame, Giulio Cerullo, and Bert Hecht. Remote detection of single emitters via optical waveguides. *Physical Review A*, 89(5):053801, 2014.
- [55] Julian Schwinger, Lester L Jr Deraad, and K. A. Milton. *Classical Electrodynamics - Chpt. 12*. Westview Press, 1998.
- [56] J M Pitarke, V M Silkin, E V Chulkov, and P M Echenique. Theory of surface plasmons and surface-plasmon polaritons. *Reports on Progress in Physics*, 70:1–87, 2007.
- [57] James Patterson and Bernard Bailey. *Solid-State Physics: Introduction to the Theory*. Springer Berlin Heidelberg, 2011.
- [58] P. B. Johnson and R. W. Christy. Optical constants of the noble metals. *Physical Review B*, 6(12):4370–4379, 1972.
- [59] P. G. Etchegoin, E. C. Le Ru, and M. Meyer. An analytic model for the optical properties of gold. *The Journal of Chemical Physics*, 125(16):164705, 2006.
- [60] P. G. Etchegoin, E. C. Le Ru, and M. Meyer. Erratum: An analytic model for the optical properties of gold. *The Journal of Chemical Physics*, 127(18):189901, 2007.
- [61] T F Villesen, Christian Uhrenfeldt, B Johansen, J Lundsgaard Hansen, H U Ulriksen, and Arne Nylandsted Larsen. Aluminum nanoparticles

- for plasmon-improved coupling of light into silicon. *Nanotechnology*, 23(8):085202, 2012.
- [62] Mark W Knight, Nicholas S King, Lifei Liu, Henry O Everitt, Peter Nordlander, and Naomi J Halas. Aluminum for plasmonics. *ACS nano*, 2013.
- [63] Edward D. Palik. *Handbook of Optical Constants of Solids*. Academic Press, 1997.
- [64] Robert L. Olmon, Brian Slovick, Timothy W. Johnson, David Shelton, Sang-Hyun Oh, Glenn D. Boreman, and Markus B. Raschke. Optical dielectric function of gold. *Physical Review B*, 86(23):235147, 2012.
- [65] Katja Höflich, Ulrich Gösele, and Silke Christiansen. Are Volume Plasmons Excitable by Classical Light? *Physical Review Letters*, 103(8):87404, 2009.
- [66] Lukas Novotny. Effective wavelength scaling for optical antennas. *Physical Review Letters*, 98(26):266802, 2007.
- [67] Suchita A. Kalele, Neha R. Tiwari, Suresh W. Gosavi, and Sulabha K. Kulkarni. Plasmon-assisted photonics at the nanoscale. *Journal of Nanophotonics*, 1:1–20, 2007.
- [68] Michael Faraday. The bakerian lecture: experimental relations of gold (and other metals) to light. *Philosophical Transactions of the Royal Society of London*, 147:145–181, 1847.
- [69] Gustav Mie. Beiträge zur optik trüber medien, speziell kolloidaler metallösungen. *Annalen der Physik*, 25(3):377 – 445, 1908.
- [70] Sergei Tretyakov. Maximizing Absorption and Scattering by Dipole Particles. *Plasmonics*, 9(4):935–944, 2014.
- [71] Paolo Biagioni, Jer-Shing Huang, and Bert Hecht. Nanoantennas for visible and infrared radiation. *Rep. Prog. Phys.*, 75(2):024402, 2012.
- [72] Craig F. Bohren and Donald R. Huffman. *Absorption and scattering of light by small particles*. Wiley, 1983.

- [73] Kathryn M. Mayer and Jason H. Hafner. Localized Surface Plasmon Resonance Sensors. *Chemical Reviews*, 111(6):3828–3857, 2011.
- [74] Julius Adams Stratton. *Electromagnetic Theory*. McGraw-Hill Book Company, Inc, 1941.
- [75] Carsten Rockstuhl, Falk Lederer, Christoph Etrich, Thomas Zentgraf, Juergen Kuhl, and Harald Giessen. On the reinterpretation of resonances in split-ring-resonators at normal incidence. *Opt. Expr.*, 14(19):8827–36, 2006.
- [76] Romain Fleury, Francesco Monticone, and Andrea Alù. Invisibility and Cloaking: Origins, Present, and Future Perspectives. *Physical Review Applied*, 4(3):037001, 2015.
- [77] K. G. Lee, X. W. Chen, H. Eghlidi, P. Kukura, R. Lettow, A. Renn, V. Sandoghdar, and S. Gotzinger. A planar dielectric antenna for directional single-photon emission and near-unity collection efficiency. *Nat Photon*, 5(3):166–169, 2011.
- [78] Mark W. Knight, Heidar Sobhani, Peter Nordlander, and Naomi J. Halas. Photodetection with active optical antennas. *Science*, 332(6030):702–704, 2011.
- [79] Shaunak Mukherjee, Florian Libisch, Nicolas Large, Oara Neumann, Lisa V. Brown, Jin Cheng, J. Britt Lassiter, Emily A. Carter, Peter Nordlander, and Naomi J. Halas. Hot electrons do the impossible: Plasmon-induced dissociation of h₂ on au. *Nano Letters*, 13(1):240–247, 2013.
- [80] M. Righini, P. Ghenuche, S. Cherukulappurath, V. Myroshnychenko, R. Quidant, and F. J. Garcia de Abajo. Nano-optical trapping of rayleigh particles and escherichia coli bacteria with resonant optical antennas. *Nano Letters*, 9(10):3387–91, 2009.
- [81] R. K. Li, H. To, G. Andonian, J. Feng, A. Polyakov, C. M. Scoby, K. Thompson, W. Wan, H. A. Padmore, and P. Musumeci. Surface-Plasmon Resonance-Enhanced Multiphoton Emission of High-Brightness Electron Beams from a Nanostructured Copper Cathode. *Physical Review Letters*, 110(7):074801, 2013.

- [82] Michael Beversluis, Alexandre Bouhelier, and Lukas Novotny. Continuum generation from single gold nanostructures through near-field mediated intraband transitions. *Physical Review B*, 68(11):115433, 2003.
- [83] M. Sivis, M. Duwe, B. Abel, and C. Ropers. Extreme-ultraviolet light generation in plasmonic nanostructures. *Nature Physics*, 9(5):304–309, 2013.
- [84] Fengwei Huo, Gengfeng Zheng, Xing Liao, Louise R Giam, Jinan Chai, Xiaodong Chen, Wooyoung Shim, and Chad A Mirkin. Beam pen lithography. *Nat Nano*, advance on:—, 2010.
- [85] Setu Kasera, Frank Biedermann, Jeremy J Baumberg, Oren a Scherman, and Sumeet Mahajan. Quantitative sers using the sequestration of small molecules inside precise plasmonic nanoconstructs. *Nano letters*, 12:5924–5928, 2012.
- [86] L. Cançado, A. Jorio, A. Ismach, E. Joselevich, A. Hartschuh, and L. Novotny. Mechanism of Near-Field Raman Enhancement in One-Dimensional Systems. *Physical Review Letters*, 103(18):186101, 2009.
- [87] M Burrelli, D van Oosten, T Kampfrath, H Schoenmaker, R Heideman, A Leinse, and L Kuipers. Probing the magnetic field of light at optical frequencies. *Science*, 326(5952):550–3, 2009.
- [88] B.C. Stipe, T.C. Strand, C.C. Poon, Hamid Balamane, T.D. Boone, J.A. Katine, J.L. Li, Vijay Rawat, Hiroaki Nemoto, Akemi Hirotsune, and Others. Magnetic recording at 1.5 Pb m⁻² using an integrated plasmonic antenna. *Nature photonics*, 4(7):484–488, 2010.
- [89] Hui Huang, A. Hoorfar, and S. Lakhani. A comparative study of evolutionary programming, genetic algorithms and particle swarm optimization in antenna design. *Antennas and Propagation Society International Symposium, 2007 IEEE*, 1:1609 – 1612, 2007.
- [90] Peter Geisler, Gary Razinskas, Enno Krauss, Xiao-Fei Wu, Christian Rewitz, Philip Tuchscherer, Sebastian Goetz, Chen-Bin Huang, Tobias Brixner, and Bert Hecht. Multimode Plasmon Excitation and In Situ

- Analysis in Top-Down Fabricated Nanocircuits. *Physical Review Letters*, 111(18):183901, 2013.
- [91] Catalin C Neacsu, Samuel Berweger, Robert L Olmon, Laxmikant V Saraf, Claus Ropers, and Markus B Raschke. Near-field localization in plasmonic superfocusing: a nanoemitter on a tip. *Nano letters*, 10(2):592–6, 2010.
- [92] Anika Kinkhabwala, Zongfu Yu, Shanhui Fan, Yuri Avlasevich, Klaus Müllen, W. E. Moerner, and Klaus Mueller. Large single-molecule fluorescence enhancements produced by a bowtie nanoantenna. *Nature Photonics*, 3(11):654–657, 2009.
- [93] M a Noginov, G Zhu, a M Belgrave, R Bakker, V M Shalaev, E E Narimanov, S Stout, E Herz, T Suteewong, and U Wiesner. Demonstration of a spaser-based nanolaser. *Nature*, 460(7259):1110–2, 2009.
- [94] Frerik van Beijnum, Peter J. van Veldhoven, Erik Jan Geluk, Michiel J. A. de Dood, Gert W. 't Hooft, and Martin P. van Exter. Surface Plasmon Lasing Observed in Metal Hole Arrays. *Physical Review Letters*, 110(20):206802, 2013.
- [95] Palash Bharadwaj, Bradley Deutsch, and Lukas Novotny. Optical antennas. *Advances in Optics and Photonics*, 1(3):438–483, 2009.
- [96] Lukas Novotny and Niek van Hulst. Antennas for light. *Nat Photon*, 5(2):83–90, 2011.
- [97] P. Zijlstra and M. Orrit. Single metal nanoparticles: optical detection, spectroscopy and applications. *Reports on Progress in Physics*, 74(10):106401, 2011.
- [98] Andrea Alu and Nader Engheta, editors. *Optical Antennas*. Cambridge University Press, 1st edition, 2013.
- [99] P. Biagioni, M. Celebrano, M. Savoini, G. Grancini, D. Brida, S. Mátéfi-Tempfli, M. Mátéfi-Tempfli, L. Duò, B. Hecht, G. Cerullo, and M. Finazzi. Dependence of the two-photon photoluminescence yield of gold

- nanostructures on the laser pulse duration. *Physical Review B*, 80(4):1–5, 2009.
- [100] E Prodan, C Radloff, N J Halas, P Nordlander, and Nordländer P. A Hybridization Model for the Plasmon Response of Complex Nanostructures. *Science*, 302(5644):419–422, 2003.
- [101] Jer-Shing Huang, Johannes Kern, Peter Geisler, Pia Weinmann, Martin Kamp, Alfred Forchel, Paolo Biagioni, and Bert Hecht. Mode Imaging and Selection in Strongly Coupled Nanoantennas. *Nano Letters*, 10(6):2105–2110, 2010.
- [102] Thorsten Feichtner, Oleg Selig, Markus Kiunke, and Bert Hecht. Evolutionary optimization of optical antennas. *Physical Review Letters*, 109:127701, 2012.
- [103] M. Fleischmann, P.J. Hendra, and A.J. McQuillan. Raman spectra of pyridine adsorbed at a silver electrode. *Chemical Physics Letters*, 26(2):163–166, 1974.
- [104] E. C. Le Ru, E. Blackie, M. Meyer, and P. G. Etchegoin. Surface enhanced raman scattering enhancement factors - a comprehensive study. *The Journal of Physical Chemistry C*, 111(37):13794–13803, 2007.
- [105] Katrin Kneipp, Yang Wang, Harald Kneipp, Lev T. Perelman, Irving Itzkan, Ramachandra R. Dasari, and Michael S. Feld. Single molecule detection using surface-enhanced Raman scattering (SERS). *Physical Review Letters*, 78(9):1667–1670, 1997.
- [106] R. Ruppin. Decay of an excited molecule near a small metal sphere. *J. Chem. Phys*, 76:1681–1684, 1982.
- [107] Jord C. Prangma, Johannes Kern, Alexander G. Knapp, Swen Grossmann, Monika Emmerling, Martin Kamp, and Bert Hecht. Electrically Connected Resonant Optical Antennas. *Nano Letters*, 12(8):3915–3919, 2012.

- [108] Johannes Kern, René Kullock, Jord Prangma, Monika Emmerling, Martin Kamp, and Bert Hecht. Electrically driven optical antennas. *Nature Photonics*, 9(9):582–586, 2015.
- [109] Kai Chen, Gary Razinskas, Thorsten Feichtner, Swen Grossmann, Silke Christiansen, and Bert Hecht. Electromechanically Tunable Suspended Optical Nanoantenna. *Nano letters*, 16(4):2680–5, 2016.
- [110] Andrea Alù and Nader Engheta. Tuning the scattering response of optical nanoantennas with nanocircuit loads. *Nature photonics*, 2:307–310, 2008.
- [111] Andrea Alù and Nader Engheta. Input Impedance, Nanocircuit Loading and Radiation Tuning of Optical Nanoantennas. *Physical Review Letters*, 101(4):43901, 2008.
- [112] Andrea Alù, Alessandro Salandrino, and Nader Engheta. Parallel, series, and intermediate interconnections of optical nanocircuit elements. 2. Nanocircuit and physical interpretation. *Journal of the Optical Society of America B*, 24(12):3014, 2007.
- [113] Jinwei Shi, Francesco Monticone, Sarah Elias, Yanwen Wu, Daniel Ratchford, Xiaoqin Li, and Andrea Alù. Modular assembly of optical nanocircuits. *Nature communications*, 5:3896, 2014.
- [114] Jer-Shing Huang, Thorsten Feichtner, Paolo Biagioni, and Bert Hecht. Impedance matching and emission properties of nanoantennas in an optical nanocircuit. *Nano Letters*, 9(5):1897–1902, 2009.
- [115] Jean-Jacques Greffet, Marine Laroche, and François Marquier. Impedance of a Nanoantenna and a Single Quantum Emitter. *Physical Review Letters*, 105(11):1–4, 2010.
- [116] Stefan A. Maier. Plasmonic field enhancement and SERS in the effective mode volume picture. *Optics Express*, 14(5):1957, 2006.
- [117] A. F. Koenderink. On the use of Purcell factors for plasmon antennas. *Optics letters*, 35(24):4208–4210, 2010.

- [118] C. Sauvan, J. P. Hugonin, I. S. Maksymov, and P. Lalanne. Theory of the Spontaneous Optical Emission of Nanosize Photonic and Plasmon Resonators. *Physical Review Letters*, 110(23):237401, 2013.
- [119] Philip Trøst Kristensen and Stephen Hughes. Modes and Mode Volumes of Leaky Optical Cavities and Plasmonic Nanoresonators. *ACS Photonics*, 1(1):2–10, 2014.
- [120] Alexander E Krasnok, Alexey P Slobozhanyuk, Constantin R Simovski, Sergei A Tretyakov, Alexander N Poddubny, Andrey E Miroshnichenko, Yuri S Kivshar, and Pavel A Belov. An antenna model for the Purcell effect. *Scientific reports*, 5:12956, 2015.
- [121] Roberto Fernández-García, Yannick Sonnefraud, Antonio I. Fernández-Domínguez, Vincenzo Giannini, and Stefan A. Maier. Design considerations for near-field enhancement in optical antennas. *Contemporary Physics*, 55(1):1–11, 2014.
- [122] Xue-Wen Chen, Mario Agio, and Vahid Sandoghdar. Metallodielectric Hybrid Antennas for Ultrastrong Enhancement of Spontaneous Emission. *Physical Review Letters*, 108(23):1–5, 2012.
- [123] Allen Taflov and Susan C Hagness. *Computational electrodynamics: the finite-difference time-domain method*. Artech House, Inc., 3rd edition, 2005.
- [124] Kane S. Yee. Numerical solution of initial boundary value problems involvin maxwell’s equations in isotropic media. *IEEE Transactions on Antennas and Propagation*, 14(3):302–307, 1966.
- [125] Markus Kiunke. Evolutionäre optimierung plasmonischer nanostrukturen. Master’s thesis, Julius-Maximilians-Universität Würzburg, Fakultät für Physik und Astronomie, 2010.
- [126] <http://www.luxpop.com>.
- [127] Jean-Pierre Berenger. A perfectly matched layer for the absorption of electromagnetic waves. *Journal of Computational Physics*, 114(2):185–200, 1994.

- [128] Thorsten Feichtner. FDTD-Simulationen an optischen Antennen. Diplomarbeit, 2008.
- [129] Gerald F. Joyce. The antiquity of RNA-based evolution. *Nature*, 418(6894):214–221, 2002.
- [130] John Henry Holland. *Adaptation in natural and artificial systems: an introductory analysis with applications to biology, control, and artificial intelligence*. University of Michigan Press, 1975.
- [131] Krzysztof Wloch and Peter J. Bentley. Optimising the performance of a formula one car using a genetic algorithm. In Xin Yao, Edmund K. Burke, Jose A. Lozano, Jim Smith, Juan Julian Merelo-Guervos, John A. Bullinaria, Jonathan E. Rowe, Peter Tino, Ata Kaban, and Hans-Paul Schwefel, editors, *Parallel Problem Solving from Nature - PPSN VIII*, number 3242 in Lecture Notes in Computer Science, pages 702–711. Springer Berlin Heidelberg, 2004.
- [132] Stefano Nolfi and Dario Floreano. *Evolutionary Robotics: The Biology, Intelligence, and Technology of Self-Organizing Machines*. Mit Press, 2000.
- [133] Shu-Heng Chen. *Evolutionary Computation in Economics and Finance*. Springer, 2002.
- [134] Mario Fernandez Pantoja, Amelia Rubio Bretones, Senior Member, Rafael Gomez Martin, and Senior Member. Benchmark antenna problems for evolutionary optimization algorithms. *IEEE Trans. Antennas Propag.*, 55(4):1111–1121, 2007.
- [135] Martin Aeschlimann, Michael Bauer, Daniela Bayer, Tobias Brixner, Stefan Cunovic, Frank Dimler, Alexander Fischer, Walter Pfeiffer, Martin Rohmer, Christian Schneider, Felix Steeb, Christian Strüber, and Dmitri V Voronine. Spatiotemporal control of nanooptical excitations. *Proceedings of the National Academy of Sciences*, 107(12):5329–5333, 2010.
- [136] Carlo Forestiere, Alyssa J. Pasquale, Antonio Capretti, Giovanni Miano, Antonello Tamburrino, Sylvanus Y. Lee, Björn M. Reinhard, and Luca

- Dal Negro. Genetically engineered plasmonic nanoarrays. *Nano Letters*, 12(4):2037–2044, 2012.
- [137] D. Macias, P.-M. Adam, V. Ruiz-Cortes, R. Rodriguez-Oliveros, and J. A. Sanchez-Gil. Heuristic optimization for the design of plasmonic nanowires with specific resonant and scattering properties. *Optics Express*, 20(12):13146–13163, 2012.
- [138] Pavel Ginzburg, Nikolai Berkovitch, Amir Nevet, Itay Shor, and Meir Orenstein. Resonances on-demand for plasmonic nano-particles. *Nano Letters*, 11(6):2329–2333, 2011.
- [139] Martin Aeschlimann, Michael Bauer, Daniela Bayer, Tobias Brixner, F Javier García de Abajo, Walter Pfeiffer, Martin Rohmer, Christian Spindler, and Felix Steeb. Adaptive subwavelength control of nano-optical fields. *Nature*, 446(7133):301–4, 2007.
- [140] Martin Aeschlimann, Tobias Brixner, Alexander Fischer, Christian Kramer, Pascal Melchior, Walter Pfeiffer, Christian Schneider, Christian Strüber, Philip Tuchscherer, and Dmitri V. Voronine. Coherent two-dimensional nanoscopy. *Science*, 333(6050):1723–1726, 2011. PMID: 21835982.
- [141] Carlo Forestiere, Massimo Donelli, Gary F Walsh, Edoardo Zeni, Giovanni Miano, Luca Dal Negro, and Luca Dal Negro. Particle-swarm optimization of broadband nanoplasmonic arrays. *Optics Letters*, 35(2):133–135, 2010.
- [142] Massimo Donelli. Design of broadband metal nanosphere antenna arrays with a hybrid evolutionary algorithm. *Optics letters*, 38(4):401–3, 2013.
- [143] Shiwei Zhou, Xiaodong Huang, Qing Li, and Yi Min Xie. A study of shape optimization on the metallic nanoparticles for thin-film solar cells. *Nanoscale research letters*, 8(1):447, 2013.
- [144] B. W. Ward, John A. Notte, and N. P. Economou. Helium ion microscope: A new tool for nanoscale microscopy and metrology. In *PAPERS*

FROM THE 50th INTERNATIONAL CONFERENCE ON ELECTRON, ION, AND PHOTON BEAM TECHNOLOGY AD NANOFABRICATION, volume 24, pages 2871–2874. AVS, 2006.

- [145] Heiko Kollmann, Xianji Piao, Martin Esmann, Simon F. Becker, Dongchao Hou, Chuong Huynh, Lars-Oliver Oliver Kautschor, Guido Boesker, Henning Vieker, André Beyer, Armin Götzhäuser, Namkyoo Park, Ralf Vogelgesang, Martin Silies, Christoph Lienau, Guido Bösker, Henning Vieker, André Beyer, Armin Götzhäuser, Namkyoo Park, Ralf Vogelgesang, Martin Silies, and Christoph Lienau. Towards Plasmonics with Nanometer Precision: Nonlinear Optics of Helium-Ion Milled Gold Nanoantennas. *Nano Letters*, 14(8):4778–4784, 2014.
- [146] G. P. Acuna, F. M. Moller, P. Holzmeister, S. Beater, B. Lalkens, and P. Tinnefeld. Fluorescence enhancement at docking sites of DNA-Directed self-assembled nanoantennas. *Science*, 338(6106):506–510, 2012.
- [147] Nathan C. Lindquist, Prashant Nagpal, Kevin M. McPeak, David J. Norris, and Sang-Hyun Oh. Engineering metallic nanostructures for plasmonics and nanophotonics. *Reports on Progress in Physics*, 75(3):036501, 2012.
- [148] Johannes Kern, Swen Grossmann, Nadezda V. Tarakina, Tim Haeckel, Monika Emmerling, Martin Kamp, Jer-Shing Huang, Paolo Biagioni, Jord C. Prangma, and Bert Hecht. Atomic-scale confinement of resonant optical fields. *Nano Letters*, 12(11):5504–5509, 2012.
- [149] A.E. Grigorescu, M.C. van der Krogt, C.W. Hagen, and P. Kruit. 10 nm lines and spaces written in HSQ, using electron beam lithography. *Microelectronic Engineering*, 84(58):822–824, 2007.
- [150] Jer-Shing Huang, Victor Callegari, Peter Geisler, Christoph BrÄ¼ning, Johannes Kern, Jord C. Prangma, Xiaofei Wu, Thorsten Feichtner, Johannes Ziegler, Pia Weinmann, Martin Kamp, Alfred Forchel, Paolo Biagioni, Urs Sennhauser, and Bert Hecht. Atomically flat single-crystalline gold nanostructures for plasmonic nanocircuitry. *Nature Communications*, 1:150, 2010.

- [151] Zhirui Guo, Yu Zhang, Yun DuanMu, Lina Xu, Shengli Xie, and Ning Gu. Facile synthesis of micrometer-sized gold nanoplates through an aniline-assisted route in ethylene glycol solution. *Colloids and Surfaces A: Physicochemical and Engineering Aspects*, 278(1-3):33–38, 2006.
- [152] Björn Hoffmann, Muhammad Y Bashouti, Thorsten Feichtner, Mirza Mačković, Christel Dieker, Ahmed Mahmoud Salaheldin, Peter Richter, Ovidiu Gordan, Dietrich Zahn, Erdmann Spiecker, and Silke Christiansen. New insights into colloidal gold flakes: structural investigation, micro-ellipsometry and patterning procedure towards ultrathin monocrystalline layers. *Nanoscale*, 2015.
- [153] Christian Rewitz, Gary Razinskas, Peter Geisler, Enno Krauss, Sebastian Goetz, Monika Pawlowska, Bert Hecht, and Tobias Brixner. Coherent Control of Plasmon Propagation in a Nanocircuit. *Physical Review Applied*, 1(1):014007, 2014.
- [154] Andreas W. Schell, Philip Engel, Julia F M Werra, Christian Wolff, Kurt Busch, and Oliver Benson. Scanning single quantum emitter fluorescence lifetime imaging: Quantitative analysis of the local density of photonic states. *Nano Letters*, 14(5):2623–2627, 2014.
- [155] Nir Rotenberg, Boris le Feber, Taco D. Visser, and L. Kuipers. Tracking nanoscale electric and magnetic singularities through three-dimensional space. *Optica*, 2(6):540, 2015.
- [156] A. Mooradian. Photoluminescence of Metals. *Physical Review Letters*, 22(5):185–187, 1969.
- [157] G. T. Boyd, Z. H. Yu, and Y. R. Shen. Photoinduced luminescence from the noble metals and its enhancement on roughened surfaces. *Physical Review B*, 33(12):7923–7936, 1986.
- [158] Petru Ghenuche, Sudhir Cherukulappurath, Tim H Taminiau, Niek F van Hulst, and Romain Quidant. Spectroscopic Mode Mapping of Resonant Plasmon Nanoantennas. *Physical Review Letters*, 101(11):116805, 2008.

- [159] Kohei Imura, Tetsuhiko Nagahara, and Hiromi Okamoto. Near-Field Two-Photon-Induced Photoluminescence from Single Gold Nanorods and Imaging of Plasmon Modes. *J. Phys. Chem. B*, 109(27):13214–13220, 2005.
- [160] M. Finazzi, P. Biagioni, M. Celebrano, and L. Duò. Selection rules for second-harmonic generation in nanoparticles. *Physical Review B*, 76(12), 2007.
- [161] M. Zavelani-Rossi, M. Celebrano, P. Biagioni, D. Polli, M. Finazzi, L. Duo, G. Cerullo, M. Labardi, M. Allegrini, J. Grand, and P.-M. Adam. Near-field second-harmonic generation in single gold nanoparticles. *Applied Physics Letters*, 92(9):093119, 2008.
- [162] <https://sourceforge.net/projects/theoea-code/>.
- [163] Oleg Selig. Evolutionaere algorithmen fuer plasmonische nanoantennen - von der implementierung zur messung. Master's thesis, Julius-Maximilians-Universitaet Wuerzburg, Fakultaeet fuer Physik und Astronomie, 2012.
- [164] M Schnell, A Garcia-Etxarri, A J Huber, K Crozier, J Aizpurua, and R Hillenbrand. Controlling the near-field oscillations of loaded plasmonic nanoantennas. *Nat. Photon.*, 3(5):287–291, 2009.
- [165] <https://sourceforge.net/projects/expea-code/>.
- [166] Thorsten Feichtner, Oleg Selig, and Bert Hecht. Plasmonic nanoantenna design and fabrication based on evolutionary optimization. *arXiv:1511.05438v1 (accepted at Optics Express)*, page 16, 2015.
- [167] Matthias D Wissert, Konstantin S Ilin, Michael Siegel, Uli Lemmer, and Hans-Jürgen Eisler. Coupled nanoantenna plasmon resonance spectra from two-photon laser excitation. *Nano letters*, 10(10):4161–5, 2010.
- [168] AW Allan W. Snyder and J. D. Love. *Optical waveguide theory*. Science paperbacks. Springer US, London ; New York, 1983.
- [169] Thorsten Feichtner, Silke Christiansen, and Bert Hecht. Mode-matching for optical antennas. *arXiv:1611.05399*, page 9, 2016.

- [170] R. Carminati, J. J. Greffet, C. Henkel, and J. M. Vigoureux. Radiative and non-radiative decay of a single molecule close to a metallic nanoparticle. *Optics Communications*, 261(2):368–375, 2006.
- [171] Milton Kerker, Dau-Sing Wang, and H. Chew. Surface enhanced raman scattering (sers) by molecules adsorbed at spherical particles: errata. *Applied Optics*, 19(24):4159–4174, 1980.
- [172] William T. Doyle. Optical properties of a suspension of metal spheres. *Physical Review B*, 39(14):9852–9858, 1989.
- [173] Jörg Enderlein. Theoretical study of single molecule fluorescence in a metallic nanocavity. *Applied Physics Letters*, 80(2):315, 2002.
- [174] Aitzol García-Etxarri, Peter Apell, Mikael Käll, and Javier Aizpurua. A combination of concave/convex surfaces for field-enhancement optimization: the indented nanocone. *Optics express*, 20(23):25201–12, 2012.
- [175] Raju Regmi, Ahmed A Al Balushi, Hervé Rigneault, Reuven Gordon, and Jérôme Wenger. Nanoscale volume confinement and fluorescence enhancement with double nanohole aperture. *Scientific reports*, 5:15852, 2015.
- [176] B S. Yeo, J Stadler, T Schmid, R Zenobi, and W Zhang. Tip-enhanced Raman spectroscopy - Its status, challenges and future directions. *Chem. Phys. Lett.*, 472(1-3):1–13, 2009.
- [177] Sebastian Schlücker. Surface-enhanced Raman spectroscopy: concepts and chemical applications. *Angewandte Chemie (International ed. in English)*, 53(19):4756–95, 2014.
- [178] Tae Joon Seok, Arash Jamshidi, Michael Eggleston, and Ming C Wu. Mass-producible and efficient optical antennas with CMOS-fabricated nanometer-scale gap. *Optics express*, 21(14):16561–9, 2013.

Anhang E

Acknowledgements

This kind of work is not possible without the backing of many people and a social framework which provides energy, motivation, inspiration, criticism and cake (no lie). Despite deeply thanking herewith everybody involved, I want to highlight some special appearances without guaranteeing completeness:

Prof. Dr. Bert Hecht: No thesis without a supervisor. I want to thank for the interesting topic, the stimulating discussions and helpful advices in many parts, not only connected with this work. I learned a lot. I'm especially grateful for the chance to follow my own ideas, when the original tasks seemed to be invincible.

Markus Kiunke and Oleg Selig: Thank you both for a lot of programming and measurements as well as for becoming really good friends. It was a lot of fun working with you. This work would not exist in this form without you.

Heiko Groß: For struggling with the same topic, improving the confocal-AFM-setup a lot and finally finding a completely different solution, when I was already on my side-track. Science wins in the end.

Dr. Jer-Shing Huang: Thank you for discovering the gold flake recipe and the great idea to use them for plasmonics. Without these substrates, none of the presented experiments would have worked out. Additionally valuable discussion about waveguides, antennas and sauna have to be mentioned.

Prof. Dr. Paolo Biagioni and Dr. Jord Prangma: We had lot of discussion about physics and beyond. Thank you for many valuable insights.

Dr. Xiafei Wu and Enno Kraus: For cooking a lot of flakes which became larger and larger!

The whole EP 5: For the always friendly atmosphere, lively conversations, lots of cake, great Christmas parties and overall a really good time.

The technical physics department : Namely Prof. Martin Kamp, Monika Emmerling, and Theresa Steinl for maintaining the FIB, trying lithography on gold flakes, evaporating MgF_2 and Au on AFM tips and besides a lot more things, for chatting during lengthy FIB milling procedures.

Prof. Dr. Silke Christiansen: For giving me a 'PraeDoc' position in Erlangen and Berlin, despite this work not being finished, yet.

Dr. Katja Höflich: For helpful discussions and a lot of proof-reading.

My parents: For laying the foundation with a lot of energy and patience.

My wife and my daughter: For reminding me what is important in life. For incredible support in long evening hours of annoying thesis writing work. For the most incredible moments in my life.

If someone feels forgotten, I'm sorry. Please tell me and I will incorporate it for sure in the next version.

Financial support by the DFG is gratefully acknowledged (HE5618/1-1).

Finally I'm really happy to live in a world that starts to share its knowledge for free, with many people investing time to build and share the software that allows to create a large part of what you have seen in the last pages:

The logo for LaTeX, featuring the word "LATEX" in a large, black, serif font.

TeX and LaTeX



Blender



Inkscape



GIMP